Synthesis of Polymers and Quantum Dots for Luminescent Solar Concentrators

by

Odin B. Achorn

B.S. Chemistry
University of New Hampshire, 2014

SUBMITTED TO THE DEPARTMENT OF CHEMISTRY
IN PARTIAL FULFILLMENT OF THE REQUIREMENTS FOR THE DEGREE OF

DOCTOR OF PHILOSOPHY IN CHEMISTRY
AT THE
MASSACHUSETTS INSTITUTE OF TECHNOLOGY

September 2020

Signature of Author: .....
Department of Chemistry
August 25, 2020

Certified by: .....
Moungi G. Bawendi
Lester Wolfe Professor of Chemistry
Thesis Supervisor

Accepted by: .....
Adam Willard
Associate Professor
Graduate Officer

This doctoral thesis has been examined by a committee of the

Department of Chemistry as follows:

Professor Troy Van Voorhis .....

Thesis Committee Chair

Haslam and Dewey Professor of Chemistry

Professor Moungi G. Bawendi.....

Thesis Supervisor

Lester Wolfe Professor of Chemistry

Professor Yogesh Surendranath.....

Thesis Committee Member

Paul M. Cook Career Development Associate Professor of Chemistry

Synthesis of Polymers and Quantum Dots for

Luminescent Solar Concentrators

by

Odin B. Achorn

Submitted to the Department of Chemistry
on August 25, 2020, in partial fulfillment of the
requirements for the degree of
Doctor of Philosophy

Abstract

In order to meet the world's increasing energy demands, we must develop innovative ways of harnessing renewable energy. Benefits can be achieved by supplementing direct photovoltaic technologies with building-integrated photovoltaics, which take advantage of existing infrastructure. For example, luminescent solar concentrators (LSCs) are semitransparent devices that harvest sunlight and redirect it toward photovoltaic cells. Because of their semitransparent nature, LSCs can be used as windows, highway noise barriers, and greenhouse walls to convert these passive structures into energy harvesters.

In the first part of this thesis, we describe the design of thin-film quantum dot (QD) LSCs, which can be deposited on existing transparent structures in the built environment. In order to disperse the thick-shelled CdSe/CdS QDs at a high concentration, we designed and synthesized a new polymer bearing carboxylic acids. The resulting film of the polymer/QD composite is highly concentrated and low scattering, and the high quantum yield of the QDs is retained. We also use a Monte Carlo simulation to predict the benefits of creating a two-layer device with both CdSe/CdS QDs and Lumogen F Red 305.

In the second part of this thesis, we introduce our development of new less toxic QDs to replace CdSe/CdS QDs in LSCs. These new QDs are based on InP, and our first task was to extend their absorption band by developing a new synthetic technique to access large sizes. This technique consists of the slow injection of phosphorus precursors into a reaction mixture of indium precursors. By controlling the injection rate, we accessed large sizes and low size dispersity.

In the third part of this thesis, we addressed reabsorption losses in InP QDs as LSC fluorophores. We did this by introducing silver dopants to the InP QDs, which redshift the emission from the absorption. We improved the quantum yield of these silver-doped InP QDs by adjusting the number of silver dopants per QD and by adding thiols as ligands. Finally, we used our Monte Carlo simulation to predict the performance of these QDs relative to CdSe/CdS QDs in LSCs.

Thesis Supervisor: Moungi G. Bawendi
Title: Lester Wolfe Professor of Chemistry

Acknowledgments

I would first like to thank the people who had a direct influence on the work presented in this thesis. Among these first acknowledgments, the first of the first is my advisor, Moungi Bawendi. I am grateful to have had the opportunity to work in his lab and to have had the intellectual freedom that he allows. I would also like to thank some fellow graduate students in the Bawendi Lab who acted as mentors. Daniel Franke helped me through my first experiments when I was a new graduate student. He taught me a lot about III-V quantum dots and how to synthesize them, and his work on the continuous-injection synthesis of indium arsenide quantum dots was the basis for my work on the continuous-injection synthesis of indium phosphide quantum dots. Igor Coropceanu did work on luminescent solar concentrators and helped me design a research project for this application. José Cordero had a big part in designing the polymer that was used for my thin-film luminescent solar concentrators. I would also like to thank Timothy Sinclair, who wrote the Monte Carlo simulation that I used to predict the performance of my luminescent solar concentrators. Jason Yoo, Cole Perkinson, and Francesca Freyria all helped in making measurements on my luminescent solar concentrators.

The second set of acknowledgments goes to my other lab mates for making the lab environment hospitable, my friends and activity partners for making my extracurricular time enjoyable, and my family for always encouraging and supporting me.

Finally, a word of thanks goes to the company that funded my research. This work was supported by Eni S.p.A. through the MIT Energy Initiative.

Table of Contents

Chapter 1: Introduction

1.1 Luminescent Solar Concentrators

Luminescent solar concentrators (LSCs) are semitransparent devices that make use of a large surface area to absorb sunlight. Reemitted light is then directed perpendicularly toward solar cells that line the perimeter of the device.[1] LSCs are composed of fluorophores dispersed in a matrix that acts as a waveguide. The fluorophores are the components that absorb the sunlight. They then emit photons by fluorescence within the waveguide. Based on the differing refractive indices between the waveguide and the exterior and the principle of total internal reflection, many of the emitted photons reflect off the inside surfaces of the waveguide until they come into contact with one of the solar-cell-coupled faces, where they are finally collected by the solar cells to create electricity. Because of their semitransparency, they are candidates for incorporating light-harvesting devices into the built environment, such as in energy-harvesting windows, greenhouse walls, and highway noise barriers.

LSCs typically take the form of rectangular prisms. In this thesis, we will orient our coordinate axes such that the surface of the earth is in an *xy* plane and sunlight travels parallel to the *z*-axis. We will refer to the LSC faces that are perpendicular to the *z*-axis as the *z* faces. The top face of the LSC, upon which sunlight impinges, is the +*z* face, and the face closer to the earth's surface is the –*z* face. Similarly, the faces perpendicular to the *x*-axis are the *x* faces, and the faces perpendicular to the *y*-axis are the *y* faces. In a typical LSC, solar cells are mounted to all four of the *x* and *y* faces. In this thesis, when there is only one solar cell, it is mounted to the +*x* face.

As mentioned in the previous paragraph, sunlight impinges on the +*z* face. Whether a photon is reflected or transmitted through this face is determined probabilistically by the Fresnel

equations. If the photon penetrates into the LSC, it has the possibility of being absorbed by a fluorophore. A new photon may then be reemitted from the fluorophore. If this new photon comes in contact with a *z* face, it will be reflected if the angle of incidence is greater than the critical angle defined by Snell's law, $\theta_c = \sin^{-1}(n_2/n_1)$, where θ_c is the critical angle, n_1 is the refractive index of the LSC matrix, and n_2 is the refractive index of the surrounding medium (which is typically air). Photons with angles of incidence greater than the critical angle will be waveguided by total internal reflection inside the LSC until they come in contact with an *x* or *y* face, where they may outcouple to a solar cell.

The ability of an LSC to concentrate light is characterized by its gain. The geometric gain is the ratio between the area of the +*z* face and the total area of the four *x* and *y* faces. The optical efficiency is the ratio between the number of photons that exit through the *x* and *y* faces and the number of photons that are incident on the +*z* face. The flux gain is the product of the geometric gain and the optical efficiency. For an LSC with a flux gain greater than 1, photons are more highly concentrated per unit area at the *x* and *y* faces than at the +*z* face. Thus, the solar cells collect more photons than if they were to be illuminated directly by the light source. In order to make this possible, the geometric gain must also be greater than 1, so in an LSC, the *z* faces are of the greatest area. This maximizes the surface area over which the LSC can absorb sunlight.

There are several important loss mechanisms that limit the efficiency of an LSC. These mechanisms are depicted in Figure 1, which is a cross section of an LSC with the page being an *xz* plane. The first event in the function of an LSC is photon absorption, so the first potential loss mechanism is transmission of a photon through the entire device without being absorbed. This may be due to a low extinction coefficient or a low concentration of the absorber. The second functional event is the emission of a photon, so the second loss mechanism is the failure of a

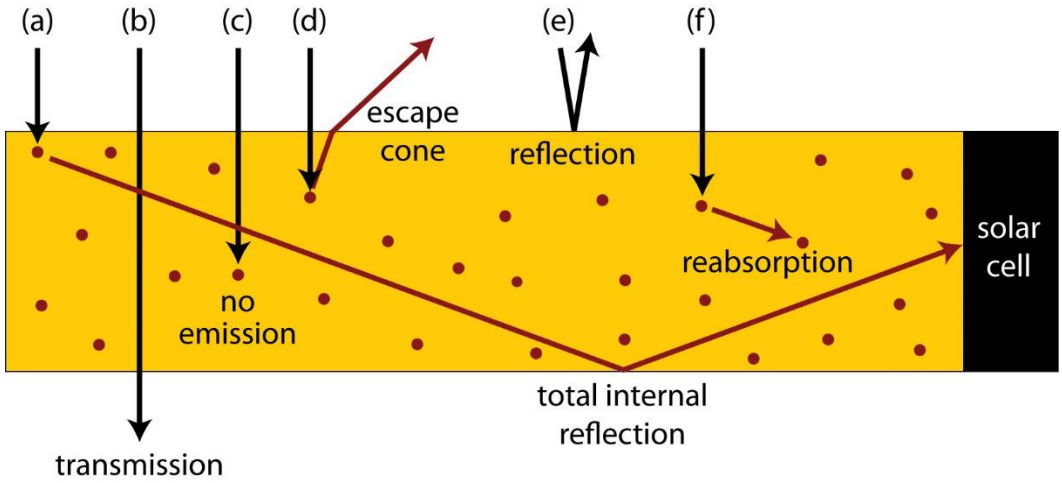

Figure 1. Capture and loss mechanisms in an LSC. (a) Light that is absorbed by a fluorophore, re-emitted in the waveguide, trapped by total internal reflection, and outcoupled to a solar cell is captured as usable energy. (b) Transmission of incident light prevents it from being harvested by the LSC. (c) Sub-unity quantum yield leads to loss by failure of the fluorophores to re-emit absorbed light. (d) Escape cone losses occur when emitted light transmits outside of the LSC as determined by the Fresnel equations. (e) Reflection of incident light off the top of the device prevents it from being harvested by the LSC. (f) Reabsorption of light emitted within the device leads to another possible incidence of mechanism (c) or (d).

fluorophore to emit a photon because of a sub-unity quantum yield (QY). The third functional event is total internal reflection, so the third loss mechanism is the transmission of an emitted photon outside of the waveguide through a range of angles called the escape cone that is determined by the refractive index of the waveguide. A second loss mechanism that depends on the refractive index of the waveguide is reflection of sunlight off of the top face of the LSC rather than absorption inside the LSC. A final mechanism that can affect the efficiency of an LSC is reabsorption of an emitted photon by another fluorophore. This only leads to a loss when it is followed by one of the other loss mechanisms mentioned above. In this project, we were mainly concerned with fluorophore improvements, so we mainly addressed QY, absorption, and reabsorption. In addition, we chose materials based on minimizing toxicity.

Various luminophores have been used for LSCs, including organic dyes and quantum dots. The archetypal dye for LSCs is Lumogen F Red 305. The success of this dye is due mostly to its high quantum yield (over 90%) and broad absorption spectrum. With an absorption maximum at 577 nm, the absorption spectrum spans most of the visible spectrum. There are dyes whose absorption spectra extend into the infrared part of the electromagnetic spectrum, enabling them to absorb more of the solar spectrum than Lumogen F Red 305 can, but they also have low QYs. Thus, any increase in the number of photons absorbed is more than compensated for by a decrease in the fraction of photons that are reemitted. Lumogen F Red 305 strikes a good balance between the number of photons that can be absorbed and reemitted. However, a major disadvantage is the low Stokes shift and the large overlap between the absorption and emission spectra. One way that dye systems for LSCs can be improved is by employing multiple dyes that interact by energy transfer.[2–10] In such a system, one dye that absorbs short wavelengths of light is in high concentration and is the primary absorber of solar light. This dye then transfers its energy to a second dye that exists in a smaller concentration. The second dye is the primary emitter of light, and it emits light at a longer wavelength than what can be absorbed by the primary absorber. This solves the reabsorption problem, but in general, less light can be harvested because the absorption band of the absorber must be blueshifted from the emitter.

Quantum dots (QDs) have the potential to combine all the beneficial aspects of an ideal LSC luminophore.[11–19] Firstly, CdSe/CdS QDs have been demonstrated to achieve near-unity quantum yields. Secondly, various strategies have been implemented to reduce the overlap between the absorption and emission spectra. One strategy is the growth of large shells that constitute the majority of the volume (and thus the majority of the absorptive ability) of the QDs. Absorption occurs mainly in the wide bandgap shell, while emission occurs mainly from the

narrower bandgap core at a much longer wavelength that cannot be reabsorbed by the shell. Thirdly, because of their band structure, they have broad absorption spectra. The bands consist of a continuum of electronic states, so QDs can absorb light of any energy greater than the bandgap.

1.2 Quantum Dots

This thesis focuses mainly on QDs as the fluorophores for LSCs. QDs are semiconductor nanocrystals. As semiconductors, their optical properties are determined by their bandgap. As nanocrystals, their bandgap is influenced by their size and quantum confinement. A bulk semiconductor has electronic states with energy levels that depend on the composition of the semiconductor. Because of the large number of atoms in the bulk system (which can be approximated as infinite), these states form continuous bands. The highest occupied band is called the valence band (VB), and it is filled with electrons. The lowest unoccupied band is called the conduction band (CB), and while it contains electronic states, it is empty of electrons. In between the VB and the CB is the bandgap, which has neither electrons nor empty electronic states. For progressively smaller samples of semiconductors, the number of atoms decreases, and the density of electronic states in the bands also decreases. At the nanometer scale, there are so few atoms in the semiconductor that the band edge states become discrete. This gives rise to the characteristic absorption spectra of QDs, which demonstrate discrete electronic transitions.

The nanometer scale of QDs also gives rise to effects from confinement. In a semiconductor, an excitation leads to a quasiparticle called an exciton, which consists of an excited electron and hole that are bound by an attractive Coulomb force. This sets up a hydrogenic system. The equilibrium distance between the excited electron and hole is called the Bohr exciton radius, and it is typically on the order of ones or tens of nanometers. For a nanoscale semiconductor such

as a QD, the radius of the QD limits the radius of the exciton. The exciton acts like a particle in a box, and so the radius of the QD determines the energy of the exciton. This leads to another characteristic of QDs, which is that the energy (and wavelength) of the light they absorb and emit is dependent on their size.

QDs are synthesized and processed as colloids, typically in organic solvents. Because of this, they are designed with organic ligands. These ligands consist of a binding group (such as a carboxylic acid, phosphonic acid, phosphine, phosphine oxide, amine, or thiol) that binds to the surface atoms of the inorganic core and a tail group (such as an alkyl chain) than allows for dispersibility in organic media.

A second function of the ligands is to passivate defects on the surface of the inorganic core. Often, these defects come in the form of dangling bonds, which result from the incomplete coordination sphere of the surface atoms.[20,21] These undercoordinated surface atoms introduce new electronic states that are different from those formed by the fully coordinated atoms in the interior of the crystal. When these surface states exist within the bandgap, an excited charge carrier can be trapped and localized. Because of being localized, the charge carrier becomes less likely to recombine radiatively with its counterpart and more likely to relax nonradiatively. By passivating these surface defects, or trap states, ligands increase the QY of the QDs.

Normally, ligands are only partially effective at passivating dangling bonds. One reason for this is that there is often a steric barrier to complete passivation. In general, surface passivation can be improved by overcoating the inorganic core with an epitaxial shell of another semiconductor.[22] By epitaxial growth, the second semiconductor passivates the dangling bonds without having a steric barrier. However, it is important that the two semiconductors adopt the same crystal structure and that they have similar lattice parameters. If there are differences in the

crystal structure or lattice parameter, those differences may lead to stacking faults that introduce defects and trap states similarly to dangling bonds.

For core/shell QDs with an ideal epitaxial shell, the surface of the core is completely passivated in much the same manner as the interior atoms. The surface of the core is no longer the surface of the QD because it is surrounded by a shell. Now, the surface atoms of the core experience an environment that is very similar to what is experienced by the atoms at the interior of the core. In a core/shell QD, there are normally still defects such as dangling bonds on the surface of the shell. However, the effect of these defects on the charge carriers can be minimized by ensuring that the carriers are separated spatially from the surface. This is done by confining the carriers to the core by making it energetically unfavorable for them to delocalize in the shell. In other words, the shell material is chosen such that its VB maximum is lower than that of the core and its CB minimum is higher than that of the core. This is called type-I band alignment, and the resulting structure is a type-I core/shell QD. Under these conditions, there are energetic barriers for the excited electron to delocalize into the shell CB and for the excited hole to localize into the shell VB. Thus, the carriers are confined to the core[23,24] and are unlikely to be trapped by defects on the surface of the shell. This leads to optical properties that are similar to that of the core, except for generally higher QYs due to the passivation of dangling bonds.

A second type of core/shell QDs are called type-II. In type II core/shell QDs, the CB maximum and VB minimum of the shell are both either higher or lower than those of the core.[25,26] This sets up a system in which one charge carrier is localized to the core while the other is localized to the shell. This can also lead to an improvement in the QY with respect to the core because one of the carriers is isolated from the surface, but there is still the other carrier that is localized in the shell and has the potential to be trapped by defects on the surface of the shell. A unique feature of

type-II core/shell QDs is broad emission profiles due to the different environments experienced by the electron and the hole.

Lastly, there are also quasi-type-II core/shell QDs. For quasi-type-II shells, the offset between either the VBs or the CBs of the two semiconductors is negligible, while the offset between the other bands is similar to that of a type-I system. In this configuration, one charge carrier is confined to the core while the other is delocalized over the core and the shell. Because one charge carrier can delocalize into the shell, it has the possibility of interacting with surface defects. Thus, quasi-type-II QDs normally have either a large shell or a second type-I shell to minimize the interaction of the charge carrier with the surface.[27–30]

Given that the optical properties of QDs depend on their size, optical homogeneity of a sample is dependent on homogeneity of the size of the QDs in the sample. Thus, a main concern of synthetic research is to design syntheses that lead to low size dispersity. These efforts are dependent on an understanding of the nucleation and growth mechanisms. The mechanism of QD growth has traditionally been understood to follow the LaMer mechanism of colloid growth that was described in 1952. In this model, there are several important species, including precursors, monomers, nuclei, and QDs. Precursors are the stable molecular reactants that are used to design the synthesis. Monomers are generally ill-defined species that form in the reaction mixture by preliminary reactions between precursors. Nuclei are small crystalline species that result from the coalescence of monomers. QDs are crystalline particles that have reached a large enough size to be stable.

In the LaMer model, precursors first convert into monomers. There is a rapid increase in the concentration of monomers, which eventually surpasses the solubility limit. At this point, there is a rapid nucleation that consumes monomers and produces nuclei. The nucleation event eases the

supersaturation of monomers such that the nucleation event ends quickly. However, there is still an appreciable concentration of monomers in the reaction mixture. These remaining monomers add to the existing nuclei in a size-focusing manner.

To take advantage of this mechanism, the so-called "hot-injection" synthesis was developed, specifically for cadmium selenide. In this method, a fatty cadmium salt (the cadmium precursor) is heated in a high-boiling organic solvent. A solution of trioctylphosphine selenide (TOPSe, the selenium precursor) is rapidly injected into the reaction mixture. Because of the rapid injection, the monomers increase in concentration rapidly as the precursors react with each other. As the concentration of monomers crosses the solubility limit, a nucleation event occurs, and the monomers form CdSe nuclei. Once the supersaturation of monomers is relaxed, nucleation stops. The reaction mixture is kept at the high reaction temperature for several more minutes. This allows the remaining monomers to diffuse through the solution and react quickly once in contact with one of the existing nuclei. This diffusion-limited reaction allows the nuclei to grow in a size-focusing manner.

1.3 Doped Quantum Dots

For intrinsic QDs, the important properties are influenced by the band edge. However, greater variability of properties can be achieved by introducing electronic dopants that involve states in addition to those at the band edge. There are two main types of QD dopants based on the nature of their electronic transitions. In one type, the dopant acts as a donor or acceptor and introduces a single new electronic state inside the bandgap of the host semiconductor. After excitation of the host, one of the charge carriers becomes trapped at the localized dopant state. Emission occurs as an electronic transition between one of the band edges and this dopant state.[31,32]

Because the dopant state is within the bandgap, this transition is of a lower energy than a band edge to band edge transition. Thus, the emission occurs at a longer wavelength than the absorption and at a longer wavelength than the emission of the corresponding undoped QD. Because one of the charge carriers exists in a quantum confined band of the host QD, the emission energy is dependent on the size of the QD. The fact that the other charge carrier is localized leads to several effects on the emission properties. One is that the photoluminescence lifetime is longer because of reduced overlap of the electron and hole wave functions.[33] Another effect is that the photoluminescence band is broad because the electron and hole, occupying different environments, are effected by phonons differently.

In the other type of doped QD, the dopant is a transition metal that has a d-d transition within the bandgap of the host semiconductor. In this design, absorption still occurs across the host's band. Then, both of the carriers relax to the dopant, where emission occurs by a d-d transition. This is most often achieved by doping with Mn^{2+}.[34–42] Because neither charge carrier exists in a quantum confined band, the emission energy is not effected by the size of the QD or the bandgap of the semiconductor, as long as the d-d transition lies inside the bandgap.

Synthetically, doped QDs can be achieved by direct incorporation in the synthesis or by post-synthetic cation exchange. In a typical direct synthesis, precursors for the host semiconductor's cation and the dopant cation are both mixed in a high-boiling solvent at high temperature, and the host semiconductor's anion precursor is rapidly injected into the mixture. A disadvantage of this method is that the existence of the dopant cation in the reaction mixture can have negative effects on the reaction and the resulting morphology of the QDs. On the other hand, in a typical cation-exchange reaction, the host QD is first synthesized by a typical method. Then, the dopant cation precursor is introduced into a hot solution of the QDs. The dopant cations can

then diffuse into the QD and replace some of the native cations. One of the advantages of this technique is that there is often no negative impact on the morphology of the QDs. Another advantage is that it allows for direct comparisons between the undoped and doped QDs because a sample of the undoped QDs can be removed from the reaction as a control before the cation exchange.

1.4 Overview

In Chapter 2, we describe the fabrication of thin-film luminescent solar concentrators, which are composed of fluorophores embedded in a matrix and deposited as a film on a waveguide. As fluorophores, we use cadmium selenide/cadmium sulfide (CdSe/CdS) QDs with thick shells that separate the absorption and emission spatially and energetically in order to reduce reabsorption. The use of these giant QDs necessitated the synthesis of a new polymer that allows for a high concentration of QDs and that has minimal impact on the QY. We also describe a Monte Carlo simulation that we used to predict the efficiency of these LSCs and to design more efficient LSCs. In Chapter 3, we describe the synthesis of large indium phosphide QDs that may be used as the basis for less toxic and more efficient LSC fluorophores than CdSe/CdS. In Chapter 4, we describe the synthesis of new silver-doped indium phosphide QDs, in which a midgap state from silver introduces a redshifted emission band that reduces reabsorption. We also describe the application of this doping strategy to the large InP QDs from Chapter 3 in order to work toward low reabsorbing LSC fluorophores that can also absorb more sunlight.

Chapter 2: Thin-Film Luminescent Solar Concentrator

2.1 Introduction

We consider two ways to construct a luminescent solar concentrator (LSC). One way is to embed the luminophores directly into the waveguide. This is called a bulk LSC. The other method is to deposit a luminescent film on top of a transparent waveguide. For reasons of cost and practicality, this film is normally much thinner than the waveguide. In such a case, the device is called a thin-film luminescent solar concentrator. Thin-film LSCs are desirable because they ease the fabrication process, enabling an LSC to be deposited onto any transparent waveguide, including glass windows.

The thin-film LSC design is commonly employed for devices that use organic dyes as the luminophores. This is because many organic dyes have good solubility in organic polymers. For example, the dye Lumogen F Red 305 is commonly dispersed in poly(methyl methacrylate), which is used to cast a thin film onto a waveguide.[43,44]

Thin-film LSCs are less commonly employed for QDs because it is difficult to disperse them well at high concentrations in organic polymers. Previous research in our group has developed CdSe/CdS core/shell QDs with thick shells that reduce reabsorption.[12] Because these QDs are so large, it is especially difficult to disperse them in polymers. In our group's previous work, the CdSe/CdS QDs were incorporated into bulk LSCs by dissolving them in a mixture of lauryl methacrylate, ethylene glycol dimethacrylate, and a photoinitiator, and then initiating a polymerization with UV light.[12] This technique worked for bulk LSCs because the QDs could be kept at a relatively low concentration at which they would remain dispersed in poly(lauryl methacrylate). However, this technique does not work well for thin-film LSCs because poly(lauryl

methacrylate) does not keep the QDs dispersed at high concentrations. At high QD concentrations, the QDs tend to aggregate with themselves, leading to scattering centers that decrease the efficiency of the LSC. If the QDs are kept at a low enough concentration to avoid aggregation, then this limits the amount of light that they can absorb. Thus, one of our goals was to develop a polymer that can interact strongly enough with the thick-shelled QDs in order for us to fabricate highly concentrated, low scattering thin-film LSCs.

In the literature, there are several methods to try to increase the concentration of QDs in polymer matrices. One is the growth of a silica shell followed by dispersion in a polymer that interacts well with the silica shell.[45] Another method is the functionalization of the surface of the QDs with polymerizable groups, and then incorporating them into the polymer during the polymerization step.[46] Both of these methods require post-synthetic modification of the QDs, which is accompanied by a decrease in quantum yield. A third method is to choose a nonpolar polymer that will interact well with the nonpolar ligands of the QDs.[47]

We introduce a new method that is less perturbative of the QDs and is thus accompanied by no loss in QY. Rather than modifying the surface of the QDs to be compatible with a polymer, we developed a new polymer that is compatible with the QDs. Specifically, this polymer has side chains terminated by carboxylic acids that can bond with the surface of the QDs. Because this polymer mimics the native fatty acid ligands of the QDs, it has no effect on the QY of the QDs.

2.2 Description and Synthesis of CdSe/CdS QDs

We chose to use cadmium selenide QDs with thick cadmium sulfide shells of about 14 monolayers, as used in previous research from our group.[12] Because the CdS shell constitutes the bulk of the volume fraction of the QD, the strongest absorption occurs in the shell. Because of the bandgap of CdS, this absorption occurs at wavelengths of 500 nm and shorter (Figure 2). After absorption, the excited charge carriers quickly relax to the core. Then, emission comes from the core at a wavelength of around 640-655 nm (Figure 2). The emitted light is at a longer wavelength than the light that is absorbed in the shell because the CdSe core has a narrower bandgap. This is causes a separation between the absorption and emission spectra, which is a beneficial property for an LSC fluorophore because it reduces the chance that an emitted photon will be reabsorbed.

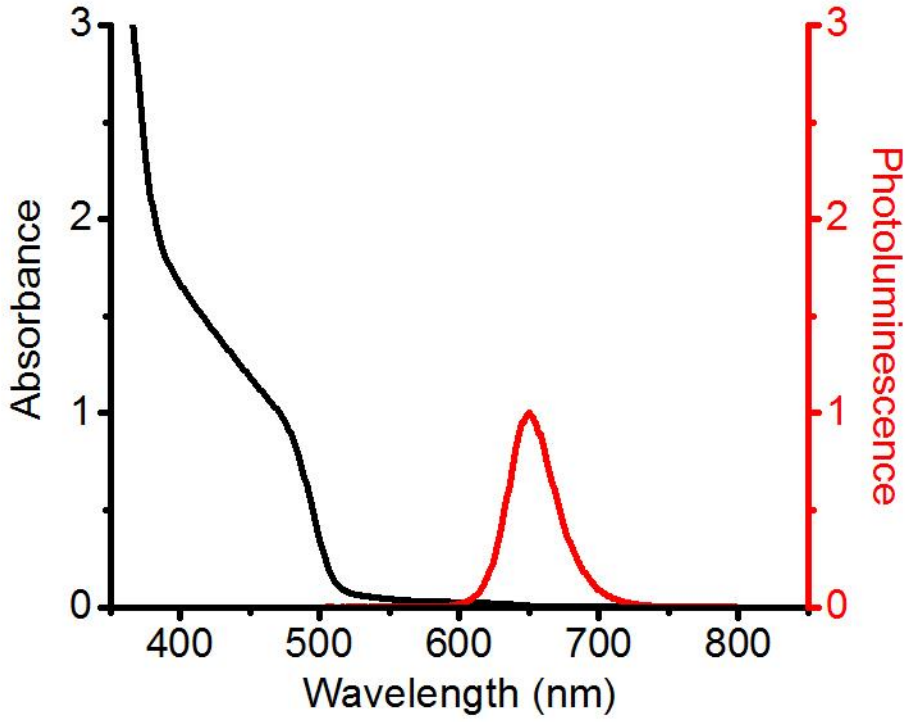

Figure 2. Absorption (black) and photoluminescence (red) spectra of thick-shelled CdSe/CdS QDs. The emission comes from the core at around 650 nm. Due to the large volume fraction of the shell, most of the absorption occurs in the shell at wavelengths shorter than 500 nm. Comparatively little absorption occurs in the core at wavelengths longer than 500 nm, making it unlikely for an emitted photon to be reabsorbed by another QD.

The emitted photons are of energy that is too low to be reabsorbed by the shell of another QD. The emitted photons may be reabsorbed by the core of another QD, but because the core constitutes a small volume fraction of the QD, this is a relatively unlikely event.

We made our QDs by a modification of the previously reported synthesis from our research group.[12] The synthesis consists of two steps. The first is the synthesis of the CdSe cores by the hot injection of trioctylphosphine selenide into a solution of cadmium octadecylphosphonate. In the second step, the purified cores are introduced into a separate reaction flask containing ODE, oleic acid, and oleylamine. Cadmium oleate and octanethiol are injected into the hot reaction mixture by a syringe pump. The basics of this reaction are understood,[30] but there are still some unknown factors that affect the reproducibility. Some of our work to rectify the low reproducibility are described below.

Many of our syntheses yielded an increase in the QY of the QDs to near 100% in the first half of the reaction. However, increasing the shell thickness even further often led to a drastic decrease in the QY. This decrease in QY was accompanied by lower dispersibility of the QDs in organic solvents. Thus, we hypothesized that these two effects were both caused by a decrease in the ligand coverage of the QDs. In these syntheses, oleic acid and oleylamine were both added at the beginning of the reaction. At high temperatures, these two chemicals undergo a condensation reaction to form an amide and water. The occurrence of this side reaction was supported by the observation of bumping of the reaction mixture, presumably as the water boiled. In order to prevent the loss of ligands and the resulting decrease in QY, we added additional oleic acid to the reaction mixture at regular intervals. The resulting quantum dots had quantum yields between 80% and 100%.

2.3 Polymer Design

Next, we designed a new polymer that we would use to disperse the thick-shelled CdSe/CdS QDs in a concentrated thin film. The first step in making our polymer was to design the pendant groups and the backbone. As pendant groups, we chose to use long-chain fatty acids to mimic the native ligands of the as-synthesized QDs. For the backbone, we chose polynorbornene because of its stiffness. This counteracts the effect of the long chains, which tends to decrease the stiffness of a polymer. Thus, for a monomer, we synthesized a long-chain fatty acid terminated by a norbornene group. We then polymerized this monomer using Grubbs's catalyst to synthesize the polymer poly(9-norbornylnonanoic acid) (Figure 3). We chose a molecular weight of about 250,000 g/mol to maintain a good stiffness.

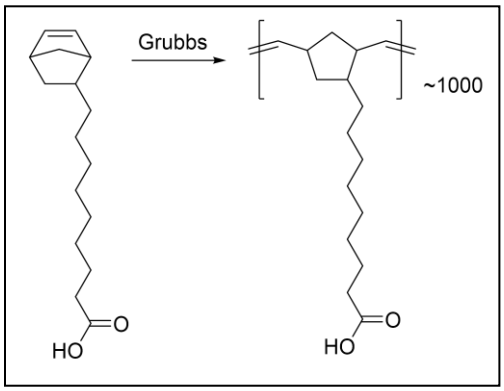

Figure 3. Polymer synthetic scheme and structure. The polymerizable group is a norbornene, which can be polymerized by Grubbs's catalyst into a polynorbornene with good stiffness. The pendant groups are terminated by carboxylic acids to bind to the surface of the QDs to keep them well dispersed. The long alkyl chains are to penetrate into the native ligand shell of the QDs.

Due to the large number of carboxylic acid groups, the polymers bind strongly to the ruthenium ions from the polymerization catalyst, making it difficult to purify the polymer. The ruthenium has an absorption band with a tail that extends into the emission wavelengths of the CdSe/CdS QDs. At the high path lengths relevant to LSCs, the optical density of this tail becomes significant and will prevent a significant portion of photons from reaching the solar cell. Thus, it

was important to remove all of the residual ruthenium from the sample. We did this by a purification step in which we added solid-supported chelators (silica microparticles functionalized with thiol groups) to a solution of the polymer. After binding the ruthenium, the chelators were filtered out of the solution.

Another property of the matrix material that we considered is its refractive index. In the optimal case, the refractive index of the film matches that of the waveguide. If the film had a greater refractive index, it would cause a portion of the emitted photons to remain in the absorptive film by total internal reflection rather than outcoupling into the transparent waveguide. On the other hand, if the film had a lower refractive index, then the escape cone would widen as determined by this lower refractive index. Fortunately, most hydrocarbon polymers have refractive indices between 1.45 and 1.50. Thus, we determined that it was not worth our effort to perform any refractive index optimization.

2.4 Formation of the Composite Film

After synthesizing the polymer, it was necessary to form the composite between the polymer and the QDs. This was done by mixing a solution of the polymer with a solution of the QDs, both in tetrahydrofuran (THF) (Figure 4.a). Attempts to dropcast films directly from this solution were unsuccessful due the rapid evaporation of THF, causing bubbles to form in the film. Thus, after mixing the THF solutions of polymer and QDs, the THF was removed by evaporation and the dry composite was then dissolved in 1,4-dioxane. While the as-synthesized QDs are not soluble in 1,4-dioxane, the polymer/QD composite is. The composite in 1,4-dioxane was then syringe filtered to remove any aggregates. The composite was then dropcast onto an acrylic waveguide, which was placed in a closed chamber to allow for the slow evaporation of solvent.

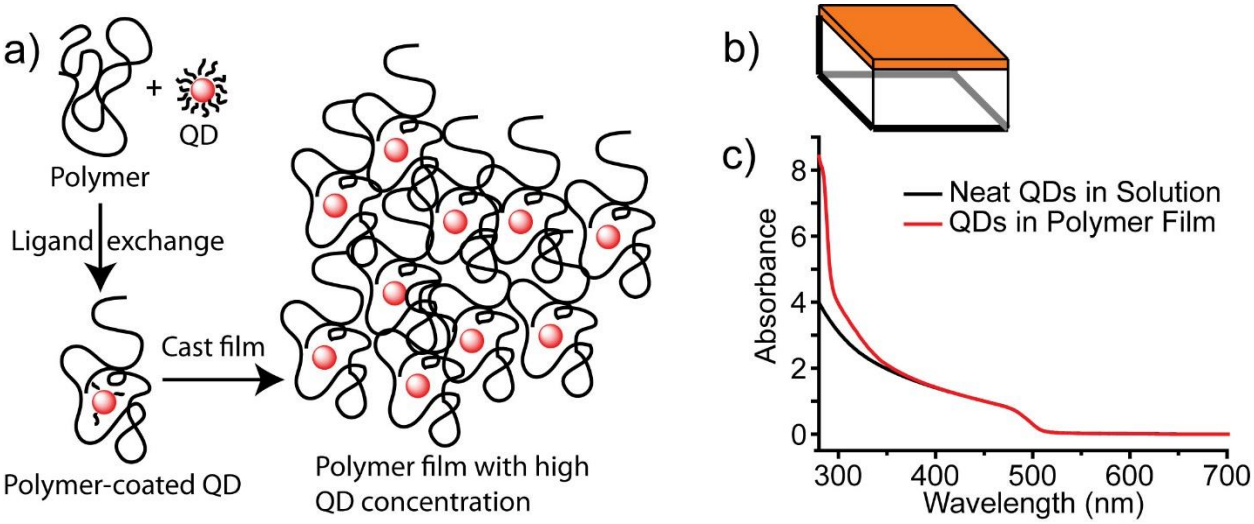

Figure 4. (a) Representation of the process of coating QDs with the polymeric ligand and casting the composite material into a film. (b) Diagram of an LSC consisting of a thin QD-impregnated polymer film on a transparent waveguide. (c) Absorption spectrum of the neat QDs in solution (black) and in a polymer film (red). The extra absorption at wavelengths shorter than 350 nm comes from the polymer. There are no spectroscopic signs of scattering in the film.

The final product was a small-scale thin-film LSC consisting of a thin film of the composite on top of the acrylic waveguide (Figure 4Figure 2.b). The QDs remained well dispersed in the polymer, and the film was low-scattering, as evidenced by the correspondence between the absorption spectra of the QDs in a solution of hexanes and in the dry polymer film (Figure 4.c).

We took transmission electron micrographs of the as-synthesized oleate-capped QDs and of the QD-polymer composite. While the relatively short oleate ligands allow for the QDs to pack closely, the bulky polymer causes the QDs to remain spread out (Figure 5). This is a nanoscopic confirmation of the ability of the polymer to keep the QDs from aggregating. It can also be seen as indirect evidence for the strong interaction between the polymer and the QDs.

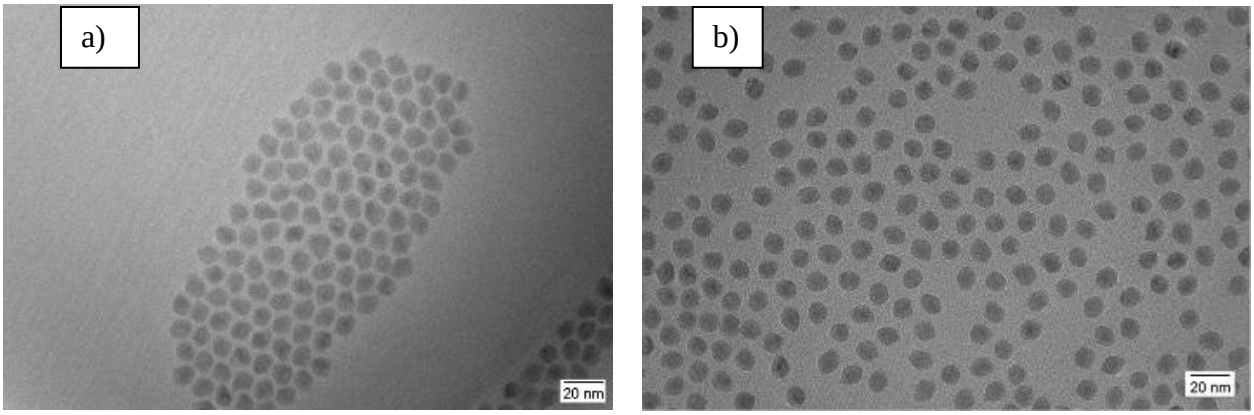

Figure 5. Transmission electron micrographs of (a) neat QDs with oleate ligands and (b) QDs associated with the polymeric ligand. Oleate is small enough to allow the QDs to pack closely. The wide spacing of QDs in (b) is indirect evidence that the polymer associates strongly enough with the QDs to keep them from aggregating.

As a second test of the interaction between the QDs and polymer, we performed qualitative size exclusion chromatography. The as-synthesized oleate-capped CdSe/CdS QDs ran through the column in a narrow band, whereas the polymer ran in a much broader band. With no chemical interaction between the two materials, we would expect the composite to run through the column as the two separate materials. The polymer would run in its wide band, and the QDs would separate out and run in their narrow band. Instead, what we observed was that the QDs and polymer ran together in the same wide band. We collected the red filtrate to dropcast it, and we found that the drop dried into a transparent composite of polymer and QD.

We also tried using several other polymers to disperse the QDs, including poly(acrylic acid) and poly(ethyl 9-norbornylnonanoate). We chose poly(acrylic acid) as a control that bears carboxylic acid groups but without long alkyl chains. Similarly, we chose poly(ethyl 9-norbornylnonanoate) as a control that bears long alkyl chains but no carboxylic acid. Both of these polymers failed at dispersing the QDs in a nonscattering film, so we conclude that the long alkyl chain and the carboxylic acid are both important components. The carboxylic acid binds to the QD

to create a strong chemical interaction. The long alkyl chain helps the carboxylic acid reach through the existing ligand shell in order to access the surface of the QDs.

2.5 Small-Scale Device Efficiency

We made a small (23×23×6 mm) model device to demonstrate the ability of our polymer to disperse CdSe/CdS QDs to make a concentrated thin film with high absorptivity, high QY, and high optical efficiency. For this device, we define the 23×23 mm faces as the *z* faces and the 23×6 mm faces as the *x* and *y* faces. A film of the polymer/QD composite was deposited on the +*z* face (Figure 6.b,c). We measured the optical efficiency using an integrating sphere. We first measured the percentage of incident photons that are reemitted through all six faces of the device [total external quantum efficiency (EQE), Figure 6.a]. We then blocked the *x* and *y* faces with black tape to measure the percentage of photons that are reemitted through the *z* faces. By subtraction, we determined the percentage of absorbed photons that are emitted through the *x* and *y* faces

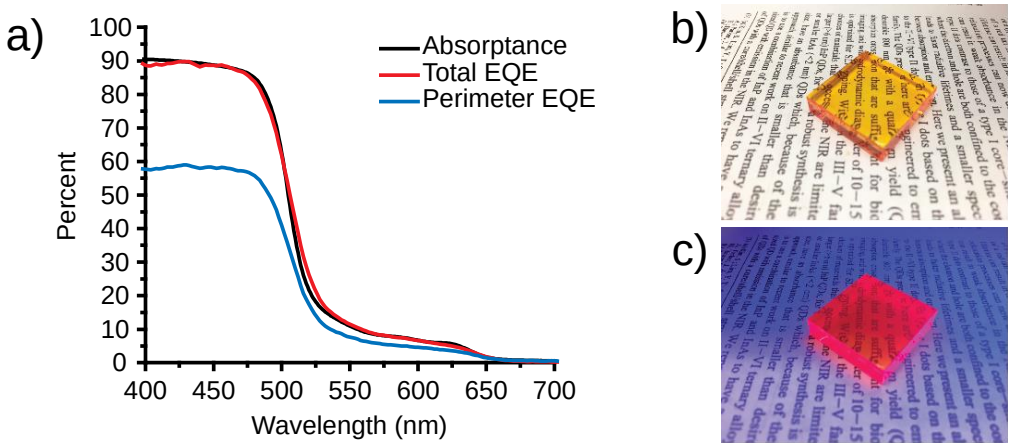

Figure 6. (a) Absorptance and external quantum efficiency of a small-scale LSC. The total EQE from all six faces (red) matches the absorptance (black), indicating near-unity quantum yield of the QDs in the film. The EQE in terms of perimeter-only emission (blue) is about 67% of the total EQE due to reabsorption and escape cone losses. The right side of the figure depicts photographs of the LSC under (b) room and (c) ultraviolet illumination. More concentrated red light can be seen emitted from the perimeter faces compared to the top face.

(Perimeter EQE). The total EQE matches the absorptance of the film, indicating a near-unity QY. The perimeter EQE is 67% of the total EQE due to reabsorption and escape cone losses.

We also characterized the performance of a small-scale model device under a solar simulator with solar cells coupled to the *x* and *y* faces (Figure 7). In this case, the QDs used in the device had a QY of only 80% as opposed to 100%. We measured the current, voltage, and power produced by the four parallel-wired solar cells surrounding the LSC when it was illuminated by a solar simulator (Table 1). We also measured the current, voltage, and power produced by one of the solar cells under direct illumination from the solar simulator.

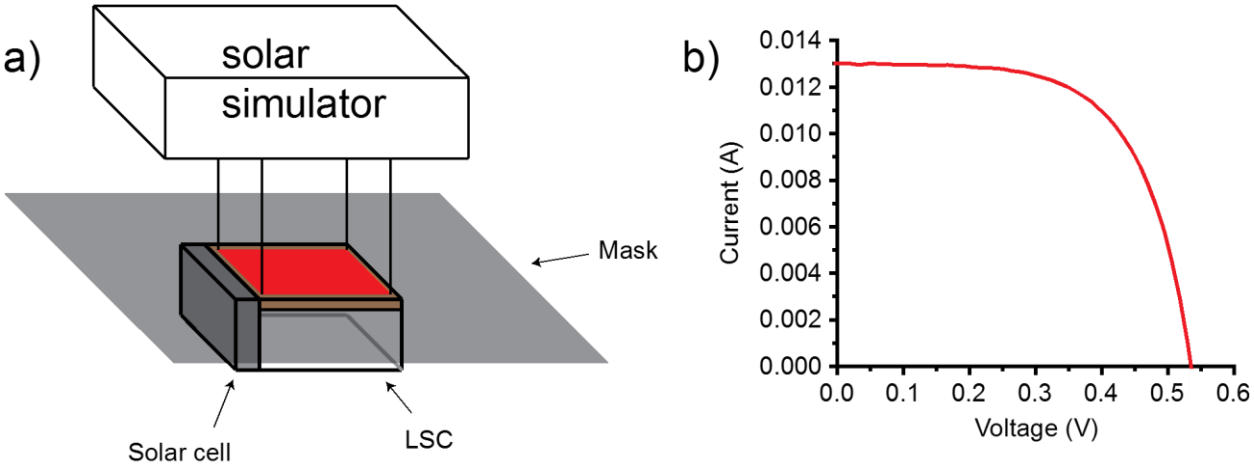

Figure 7. (a) Setup for measuring the power output of solar cells mounted to the perimeter of a small-scale LSC illuminated by a solar simulator. The figure depicts only one solar cell for clarity, but in the actual experiment, all four *x* and *y* faces were coupled to solar cells that were wired together in parallel. A mask is used to limit the area of illumination. (b) Current-voltage curve of the four parallel-wired solar cell in the experiment depicted in (a).

Table 1. Measured Current, Voltage, and Power of Solar Cells and Luminescent Solar Concentrators

Current produced by 1 solar cell under solar simulator	0.04118 A
Voltage produced by 1 solar cell under solar simulator	0.6569 V
Power produced by 1 solar cell under solar simulator	18.20 mW
Current produced by 4 solar cells coupled to LSC under solar simulator	0.01299 A
Voltage produced by 4 solar cells coupled to LSC under solar simulator	0.5354 V
Power produced by 4 solar cells coupled to LSC under solar simulator	4.379 mW

In a separate experiment, using a monochromator, we measured the responsivity of the solar cell as a function of the wavelength of the incident light. We used this, along with the current produced by the LSC-coupled solar cells, to determine the power of light and the number of photons per second that were incident on the LSC-coupled solar cells (Table 2).

Table 2. Measured Responsivity of the Solar Cell and Estimated Amount of Light Incident on the LSC-Coupled Solar Cells

Responsivity of the solar cell at 640 nm	0.484 A/W
Power of 640 nm light incident on the 4 solar cells	26.85 mW
Number of 640 nm photons incident on the 4 solar cells	$8.833\ 10^{16}$ photons/s

Next, we used the AM1.5 solar spectrum and the absorptance spectrum of the LSC to estimate the power and photon density that were incident on the LSC and that were absorbed by the LSC (Table 3). To be rigorous, we would have used the power spectrum of the solar simulator rather than the AM1.5 solar spectrum. The solar simulator spectrum was difficult to obtain, so we used the AM1.5 solar spectrum as an approximation.

Table 3. Power and Photon Density Incident on and Absorbed by the LSC

Power density incident on LSC	100.0 mW/cm^2
Power density absorbed by LSC	20.42 mW/cm^2
Density of photons incident on LSC	$4.303\ 10^{17}$ photons/s/cm^2
Density of photons absorbed by LSC	$4.565\ 10^{16}$ photons/s/cm^2

Lastly, we note the geometric dimensions of the LSC and the solar cells (Table 4).

Table 4. Geometric Dimensions of the LSC and Solar Cells

Area of LSC	5.29 cm^2
Illuminated area of LSC	4.00 cm^2
Perimeter area of LSC	5.52 cm^2
Area of solar cell	1.20 cm^2
Area of 4 solar cells	4.80 cm^2

We used these data to first present an estimation of the EQE. Figure 6 presents the EQE for each wavelength of excitation light, but we now estimate the EQE integrated across the entire

solar spectrum, weighted by the number of photons of each wavelength. We find a value of 5.13%. We also estimate the internal quantum efficiency (IQE) of the LSC, which is defined as the ratio between the number of photons that are incident on the LSC-coupled solar cells and the number of photons that are absorbed by the LSC. We find a value of 48.37%, which becomes 55.63% after correcting for the fact that the combined active area of the solar cells is only 4.80 cm^2, compared to the area of the *x* and *y* faces of the LSC, which is 5.52 cm^2. Still, this 55.63% is lower than the 67% calculated by the integrating sphere. This is accounted for by the fact that the QY of the QDs in this device was only 80%, whereas the QY of the QDs in the integrating sphere experiment was 100%.

We can also assign efficiencies based on the power output. One figure of merit is the ratio of the power conversion efficiency of the LSC (1.09%) to the power conversion efficiency of the solar cells (15.16%). In other words, it is the power produced by the LSC divided by the power that would be produced by a solar cell of the same area as the LSC. In our case, the figure is 7.218%. However, the purpose of an LSC is not to replace a solar cell with a new device of the same surface area. Instead, the purpose is to effectively increase the absorbing area of a solar cell of a constant size. Thus, a better figure of merit for our purposes is the power produced by the solar cells surrounding the LSC divided by the power that would be produced by these solar cells if they were instead directly illuminated by the sun. This figure is 6.015%. While this indicates that the use of the LSC actually decreases the power output of the solar cells compared to their direct illumination, we must also remember that this is a small-scale device in which the total surface area of the solar cells is greater than that of the LSC. In other words, the geometric gain is less than 1. This measurement of the efficiency will scale with the area of the +*z* face. However, it does not scale linearly because of effects of reabsorption. The farther the point of excitation is

away from the edge of the device and the solar cell, the longer the path length of the emitted photons through the absorptive waveguide. This increases the probability of the photon being reabsorbed and lost. Thus, we set out to understand exactly how the efficiency scales with the size of the LSC.

2.6 Predictions of LSC Efficiency

Our experiments to determine how the efficiency scales with the size of the LSC are based on a model device that is 300×23×6 mm. The *y* and *z* dimensions are the same as the small-scale device of the previous section, but the *x* dimension is roughly 13 times as big. In these experiments, a solar cell is mounted to the +*x* face. Before presenting the experimental results, we will present our predictions of the performance. These include analytical solutions that assume fluorophores with no reabsorption and Monte Carlo simulations that take reabsorption into account.

2.6.1 Analytical Solutions

We begin our discussion of our predictions of LSC efficiency by presenting analytical solutions for the efficiency of an ideal non-reabsorbing LSC as a function of the position of illumination. For these predictions, we choose to define the efficiency in terms of the number of photons that are collected by the solar cell relative to the number of photons that are incident on the LSC. These solutions consider the geometry of the device, the refractive index, and the Fresnel equations. Reabsorption of photons by the fluorophores adds complexity because of the increased number of events to consider. Thus, we assume no reabsorption for these solutions.

For these solutions, we imagined an LSC that is 300×23×6 mm with a 0.1 mm fluorophore film. We assumed an isotropically emitting fluorophore with 100% QY and no overlap between

its absorption and emission spectra in order to avoid complications related to multiple reabsorption events. In addition, the fluorophore absorbs 100% of the photons with which it comes in contact. We orient the axes such that the fluorophore film is in an *xy* plane of constant *z*. The solar cell is in a *yz* plane of constant *x*. Based on these coordinates and the orientation of the LSC, we call the 23×6 mm faces the *x* faces, the 300×6 mm faces the *y* faces, and the 300×23 mm faces the *z* faces. Thus, the solar cell is mounted to the +*x* face. In our analyses, we generate a photon at the origin of our coordinate system, a distance *d* along the *x*-axis away from the solar cell. We allow for this photon to be emitted in any direction with azimuthal angle θ and polar angle φ such that the possible rays fill a uniform distribution in a sphere. For an isotropic emitter at the origin of a polar coordinate system, the probability density function of a photon being emitted with angles φ and θ is $(\sin\varphi)/(4\pi)$. The fraction of absorbed photons that is reemitted to the solar cell is found by integrating this function over the range of angles φ and θ for which the photon will be totally internally reflected and outcoupled at the +*x* face. For an LSC of refractive index 1.49 surrounded by air, $(\pi/2)-\sin^{-1}(1/1.49) < \varphi < (\pi/2)-\sin^{-1}(1/1.49)$. The restriction on θ is more complicated because the angle at which a photon contacts an *x* or *y* face depends on θ and φ. They are shown as the integration limits in Equation 1. The integral in Equation 1 works out to 0.129, which is the fraction of photons absorbed by the LSC that are then incident on the solar cell (Figure 8.a).

$$\int_{\frac{\pi}{2}-\sin^{-1}\frac{1}{1.49}}^{\frac{\pi}{2}+\sin^{-1}\frac{1}{1.49}} \int_{-\cos^{-1}\frac{\cos\left(\sin^{-1}\frac{1}{1.49}\right)}{\sin\varphi}}^{\cos^{-1}\frac{\cos\left(\sin^{-1}\frac{1}{1.49}\right)}{\sin\varphi}} \frac{1}{4\pi}\sin\varphi \, d\theta \, d\varphi = 0.129 \qquad \text{Equation 1}$$

We also derived a solution for a case in which the solar cell is index matched to the +*x* face. This solution requires several more integrals because we no longer consider total internal reflection at the +*x* face. This adds some directional dependence and some distance dependence to

the allowed angles. The six required integrals are shown in Equations 2-7, and the graph is shown in Figure 8.b.

$$\int_{\sin^{-1}\frac{1}{1.49}}^{\frac{\pi}{2}-\sin^{-1}\frac{1}{1.49}} \int_{0}^{\frac{\pi}{2}} \frac{2}{\pi} \sin\varphi \, \mathrm{d}\theta \, \mathrm{d}\varphi = 0.07019 \qquad \text{Equation 2}$$

$$\int_{\frac{\pi}{2}-\sin^{-1}\frac{1}{1.49}}^{\frac{\pi}{2}} \int_{\cos^{-1}\frac{\cos\left(\sin^{-1}\frac{1}{1.49}\right)}{\sin\varphi}}^{\sin^{-1}\frac{\cos\left(\sin^{-1}\frac{1}{1.49}\right)}{\sin\varphi}} \frac{2}{\pi} \sin\varphi \, \mathrm{d}\theta \, \mathrm{d}\varphi = 0.1538 \qquad \text{Equation 3}$$

$$\int_{\frac{\pi}{2}-\sin^{-1}\frac{1}{1.49}}^{\frac{\pi}{2}} \int_{0}^{\sin^{-1}\frac{\cos\left(\sin^{-1}\frac{1}{1.49}\right)}{\sin\varphi}} \frac{2}{\pi} \sin\varphi \, \mathrm{d}\theta \, \mathrm{d}\varphi = 0.412471 \qquad \text{Equation 4}$$

$$\int_{\tan^{-1}\frac{d}{6.1}}^{\sin^{-1}\frac{1}{1.49}} \int_{0}^{\cos^{-1}\frac{d}{6.1\tan\varphi}} \frac{2}{\pi} \sin\varphi \, \mathrm{d}\theta \, \mathrm{d}\varphi = \frac{2}{\pi} \int_{\tan^{-1}\frac{d}{6.1}}^{\sin^{-1}\frac{1}{1.49}} \sin\varphi \left[\cos^{-1}\frac{d}{6.1\tan\varphi}\right] \mathrm{d}\varphi \qquad \text{Equation 5}$$

$$\int_{\frac{\pi}{2}-\sin^{-1}\frac{1}{1.49}}^{\sin^{-1}\frac{\cos\left(\sin^{-1}\frac{1}{1.49}\right)}{\sin\left(\tan^{-1}\frac{11.5}{d}\right)}} \int_{0}^{\sin^{-1}\frac{\cos\left(\sin^{-1}\frac{1}{1.49}\right)}{\sin\varphi}} \frac{2}{\pi} \sin\varphi \, \mathrm{d}\theta \, \mathrm{d}\varphi \qquad \text{Equation 6}$$

$$= \frac{2}{\pi} \int_{\frac{\pi}{2}-\sin^{-1}\frac{1}{1.49}}^{\sin^{-1}\frac{\cos\left(\sin^{-1}\frac{1}{1.49}\right)}{\sin\left(\tan^{-1}\frac{11.5}{d}\right)}} \sin\varphi \sin^{-1}\frac{\cos\left(\sin^{-1}\frac{1}{1.49}\right)}{\sin\varphi} d\varphi$$

$$\int_{\sin^{-1}\frac{\cos\left(\sin^{-1}\frac{1}{1.49}\right)}{\sin\left(\tan^{-1}\frac{11.5}{d}\right)}}^{\frac{\pi}{2}} \int_{0}^{\tan^{-1}\frac{11.5}{d}} \frac{2}{\pi} \sin\varphi \, \mathrm{d}\theta \, \mathrm{d}\varphi = \frac{2}{\pi} \tan^{-1}\frac{11.5}{d} \left(\cos\left(\sin^{-1}\frac{\cos\left(\sin^{-1}\frac{1}{1.49}\right)}{\sin\left(\tan^{-1}\frac{11.5}{d}\right)}\right)\right) \qquad \text{Equation 7}$$

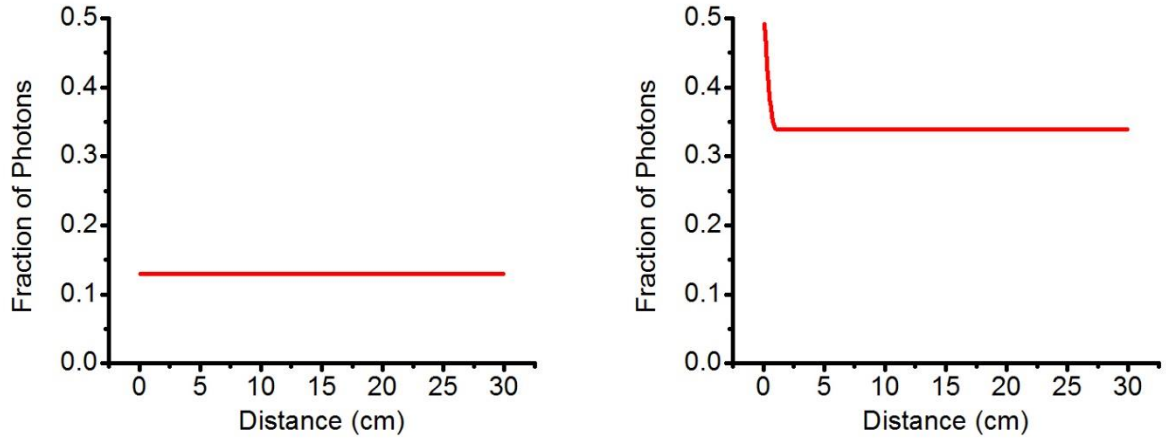

Figure 8. Calculated efficiency of a non-reabsorbing large-scale LSC that has (a) no refractive index matching to the surroundings and (b) one solar cell index-matched to an *x*-face. Efficiency is defined as the fraction of photons incident on a given position of the LSC that are collected by the solar cell mounted to the LSC at distance $x = 0$.

2.6.2 Monte Carlo Simulation

In order to predict the performance of real LSCs with overlapping absorption and emission spectra, we implemented Monte Carlo simulations in MATLAB by coding a ray-tracing model. Instead of calculating solutions analytically, this simulation tracks the unique trajectory of each individual photon. The trajectory is updated at each absorption, emission, transmission, and reflection event by choosing a discrete value from an appropriate probability distribution. Every important property of the LSC can be manipulated in this simulation, including size, refractive index of the LSC and surroundings, absorption spectrum, fluorescence spectrum, and QY.

In these simulations, we treat each photon's trajectory stochastically, drawing penetration depths and reflection vs. transmission decisions from the physically appropriate distributions. We derive the penetration depth distributions from transmission spectra of each bare layer, and reflection probabilities from the measured indices of refraction of each layer. After averaging the results of hundreds of thousands of photon trajectories, the Monte Carlo simulations converge to

the actual device performance. For devices using the nearly ideal QD fluorophores with extremely low reabsorption, we find escape cone losses to be the predominant loss mechanism for the wavelengths of light that are absorbed by the QDs. Additionally, by increasing the size of the simulated LSC for a device architecture for which simulations of smaller devices matched the measured efficiency, we are able to predict the performance of our materials in a real-world application.

The MATLAB code for this simulation can be found in the Appendix. After specifying the dimensions of the device and the thickness, index of refraction, transmission spectrum, emission spectrum, and QY of each layer, individual photon trajectories were determined by the following routine:

1. Initiate the photon's wavelength, position, and direction.
2. Draw a penetration depth in the current layer.
3. Trace the trajectory of the photon to the nearest external or internal interface.
    a. If the balance of the penetration depth is lower than the distance to this surface, truncate the trajectory at the end of the penetration depth and skip to step 7.
    b. Otherwise, subtract the distance traveled to the collision point from the balance of the penetration depth and set the photon's location to the collision point.
4. Draw a reflection vs. transmission decision and adjust the photon's direction and polarization appropriately.
    a. If the photon is now outside and moving away from the device, this photon's lifecycle is over. Record its final resting place and its wavelength and exit.
    b. Otherwise, return to step 3.
5. Draw a re-emission decision using the appropriate QY.

a. If the photon is not re-emitted, this photon's lifecycle is over. Record its final resting place and its wavelength and exit.

b. Otherwise, determine the photon's new wavelength and direction and return to step 3.

To make sure that the simulation was treating the geometry and Fresnel equations correctly, we first input non-overlapping transmission and emission spectra into the code. This way, the code was simulating the same conditions as the analytical solutions. The simulation matched the calculations well (Figure 9), confirming that the simulation works properly, at least for a non-reabsorbing case.

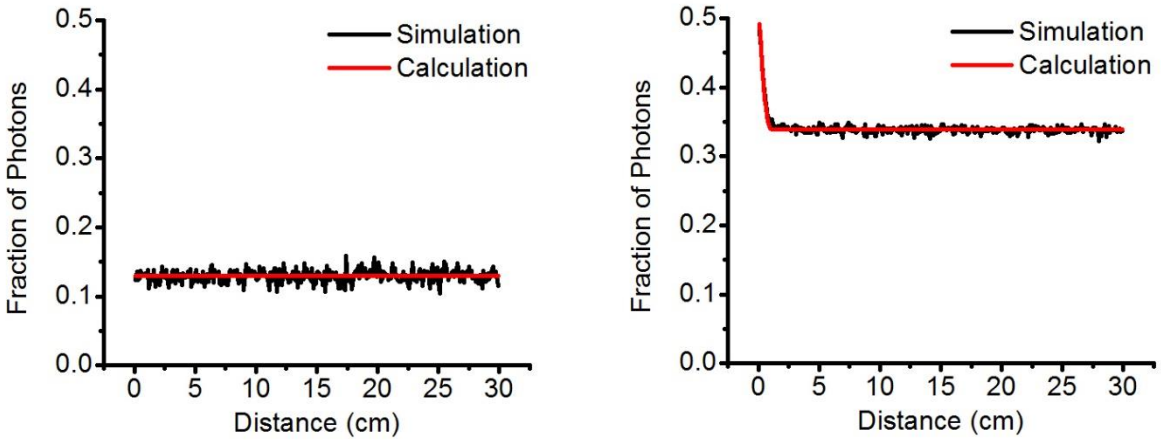

Figure 9. Simulated efficiency (black) compared to calculated efficiency (red) of a non-reabsorbing large-scale LSC that has (a) no refractive index matching to the surroundings and (b) one solar cell index-matched to an *x*-face. Efficiency is defined as the fraction of photons incident on a given position of the LSC that are collected by the solar cell mounted to the LSC at distance $x = 0$.

2.7 Large-Scale Device Efficiency

We also tested the performance of a 300×23×6 mm LSC experimentally. First, we fabricated such a device by dropcasting a film of the polymer/QD composite onto a 300×23×6 mm acrylic slab. When designing the large-scale device, it was important to balance two competing

effects of the optical density of the film. The first effect is the amount of sunlight that the LSC can absorb, and the second effect is the amount of emitted light that will be reabsorbed. Films with high optical density absorb a lot of sunlight, which has the effect of increasing the power output of the device. However, they also experience more reabsorption, which has the effect of decreasing the power output of the device. On the other hand, a film with lower optical density will experience less reabsorption, but will also absorb less sunlight to begin with. In order to find the correct optical density to balance these two effects, we fabricated a thin-film LSC by depositing the film in three separate layers, increasing the optical density with each layer.

In order to measure the efficiency of this device, we lay the LSC down on a black surface and mounted a solar cell to one of the *x* faces. We positioned a 405 nm laser above and pointing down at the LSC (Figure 10.a). This laser was mounted on a stage that can be translated in the *x* direction. With the laser on, illuminating a small area at a certain distance from the solar cell, we measured the current output by the solar cell. We moved the point of illumination by 0.5 cm increments along the length of the LSC, measuring the current output at each step and comparing to the current output of the solar cell illuminated directly by the laser. We found that the first layer had a relatively constant response in producing current in the solar cell as a function of the illumination distance of the laser (Figure 10.c). Because of the low optical density, the reabsorption losses were minimal. The addition of a second layer increased the current at short distances because of increased absorption, but there was no improvement at long distances because the increased absorption was balanced out by increased reabsorption losses at long path lengths. The addition of a third layer led to a decrease in current at all distances because the percentage of absorbed photons was already approaching 100% at the excitation wavelength. This means that there was very little

difference in the number of photons absorbed between the second and third layers. However, the absorptance at the emission wavelengths increased, leading to increased reabsorption losses.

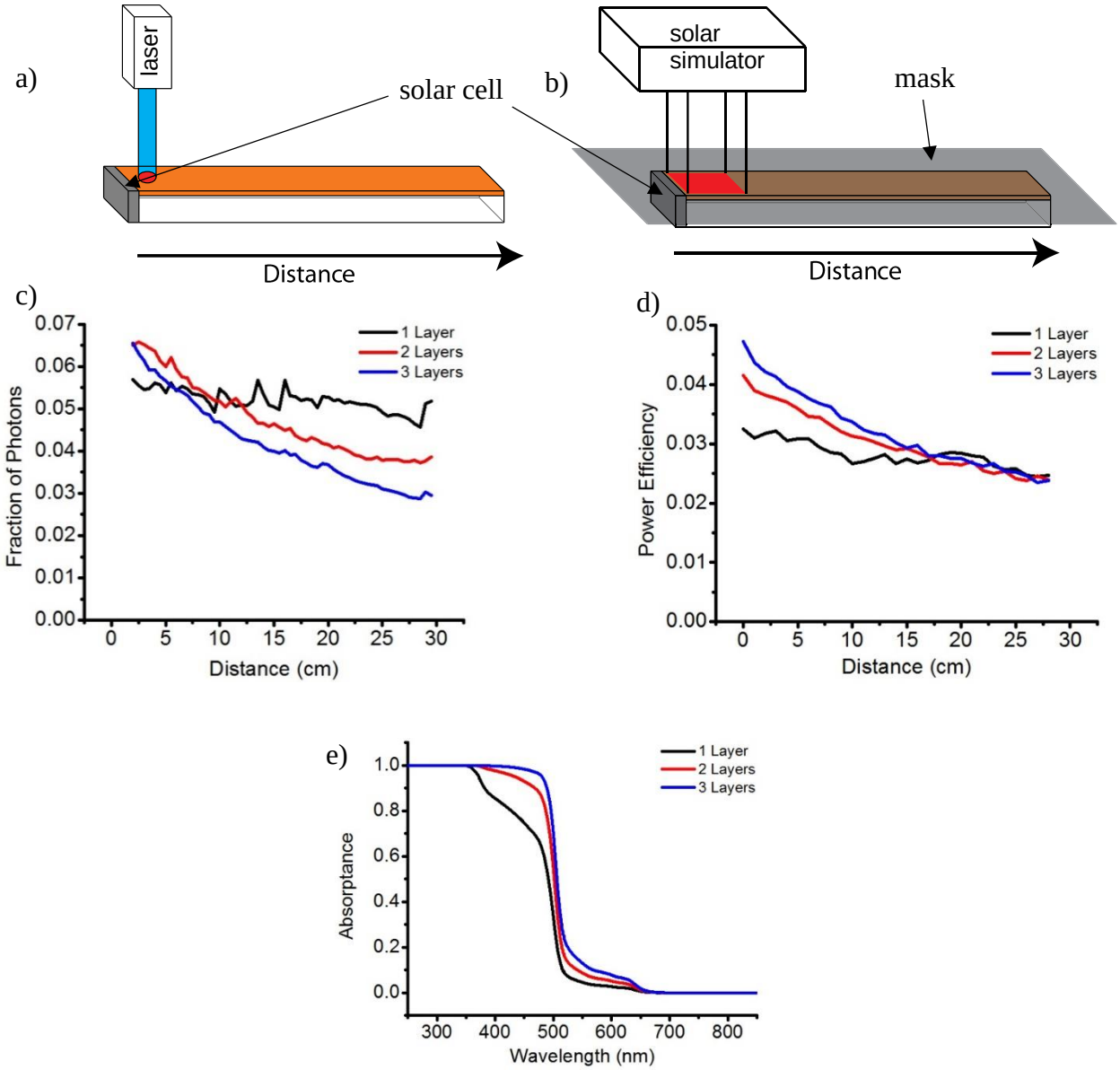

Figure 10. Diagrams of the experimental setup for measuring the efficiency of a large-scale LSC as a function of illumination distance under illumination by (a) a laser and (b) a solar simulator. Illumination from the solar simulator was limited to a 2×2 cm area by a mask (c) Fraction of photons collected by the solar cell relative to the number of photons incident on the LSC from the laser, as a function of illumination position. (d) Amount of power produced by the LSC-coupled solar cell relative to the power it would produce when illuminated directly by the solar simulator (power efficiency). We added three layers of the polymer/QD composite to the LSC and measured the photon and power efficiency after each layer. After successive layers, increases in efficiency are due to increased absorptance and decreases in efficiency are due to increased reabsorption (e) Absorptance spectra of the LSC with 1, 2, and 3 layers of the polymer/QD composite film.

We ran a Monte Carlo simulation using the transmission and emission spectra of the QD film and found a near-perfect correspondence with the experimental result (Figure 11). This gives us confidence simultaneously that the simulation treats reabsorption correctly and that the physical LSC is performing at its theoretical maximum.

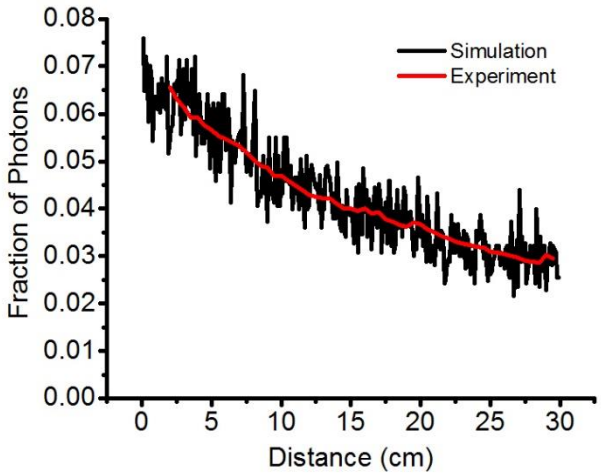

Figure 11. Fraction of photons collected by the +*x*-mounted solar cell relative to the number of photons incident on the LSC from the laser, as a function of illumination position. The results of the Monte Carlo simulation (black) match those of the experiment on the real device (red), giving us confidence that the simulation works properly and the real device is operating at its maximum.

We also illuminated the LSC by a solar simulator (Figure 10.b). We used a mask to control the area of illumination at 2×2 cm, and we moved this area of illumination down the length of the LSC in 1 cm increments. We measured the power output of the LSC-coupled solar cell under these conditions and compared it to the power that would be produced by the solar cell if illuminated directly by the solar simulator. We call this value the power efficiency. Again, the first layer showed a relatively constant response across the entire length (Figure 10.d). The second layer showed increased power at short distances compared to the first layer. The third layer also showed increased power compared to the second layer. This contrasts with the trend for monochromatic 405 nm excitation, in which the third layer performs worse than the second layer. This is because, while the percentage of absorbed photons at 405 nm does not change much between the second and third layer, the percentage of absorbed photons at wavelengths longer than 405 nm increases

from the second to the third layer. With the broadband excitation of the solar simulator, this leads to an overall increase in the number of photons absorbed. However, the third layer appears to be approaching the limit of efficiency because there is not much of an increase between the second and third layer. Also, at long distances, the efficiency of the third layer is the same as that of the first and second layer. With greater optical density, the efficiency at these long distances will likely drop due to increased reabsorption.

Knowing how the device performs (specifically the current produced) under illumination of a constant area at different positions, we can now estimate how the device will perform when its entire area is illuminated. When the entire area is illuminated, each unique 2×2 cm section will still contribute the same number of photons to the solar cell as when that section is illuminated individually. Thus each section is still responsible for the same amount of current. To estimate the current produced by the solar cell when the entire device is illuminated, we simply have to add up the currents produced by the solar cell when each unique 2×2 cm section is illuminated individually. Then, by fitting the solar cell's power output as a function of current, we can estimate the power that will be produced by the solar cell when the entire device is illuminated. For 1 layer, 2 layers, and 3 layers, the total current is 0.02496 A, 0.02791 A, and 0.2789 A, respectively, and the estimated power output is 10.67 mW, 12.06 mW, and 12.05 mW. Compared to the 18.20 mW that would be produced by the solar cell if illuminated directly by the solar simulator, the power efficiencies are 58.60%, 66.28%, and 66.23%, respectively. Thus, the LSC-coupled solar cell still does not perform as well as the solar cell on its own. We could continue trying larger LSCs with greater geometric gains to see if we could eventually reach a power efficiency over 100%, but instead, we decided to make improvements to the active layer.

2.8 Two-layer Device

While measuring the performance of the CdSe/CdS LSC under illumination from a solar simulator, we noted that its biggest limitation is in the amount of light that it can absorb. Most of the absorption of light occurs in the CdS shell, which has a bandgap that corresponds to roughly 500 nm. Thus, this device cannot make much use of any solar light at wavelengths longer than 500 nm. In contrast, the organic dye Lumogen F Red 305 has an absorption spectrum that reaches out past 600 nm. Because of its broadband absorption and high QY, and despite the large overlap between its absorption and emission spectra, this dye performs better in a 300x23x6 mm LSC under a solar simulator than CdSe/CdS QDs do (Figure 12a). However, under monochromatic excitation, the QDs outperform the dye because of their lower reabsorption (Figure 12.b) This means that the QDs perform better per absorbed photon, but the dye performs better for a given incident solar flux. Thus, we imagined a multilayer LSC that makes use of the advantages of both of these fluorophores. This LSC consists of the poly(methyl methacrylate) waveguide, a film of Lumogen-impregnated PMMA, and a top layer of CdSe/CdS QDs dispersed in our new polymer

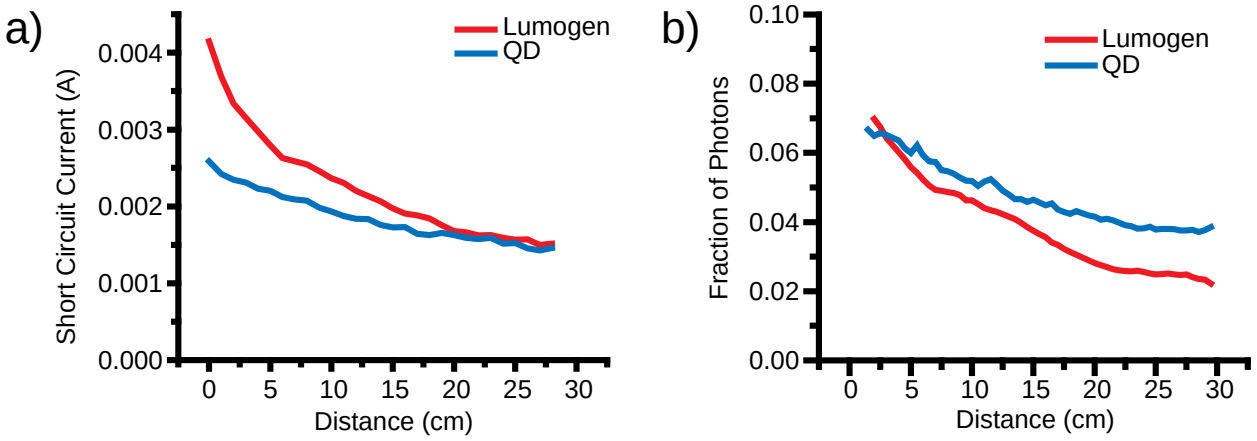

Figure 12. (a) The short circuit current produced by an *x*-coupled solar cell as a function of solar simulator illumination distance and (b) the fraction of photons collected by an *x*-mounted solar cell as a function of laser illumination distance for Lumogen F Red 305 (red) and CdSe/CdS QD (blue) LSCs. The Lumogen LSC performs better under the solar simulator because it can absorb more light. The QD LSC performs better under laser illumination because of the lower reabsorption.

(Figure 13.b). With this structure, photons would impinge first upon the QD layer. This maximizes the number of photons absorbed by the QDs and the number of photons emitted by the QDs. Of the two fluorophores, the QDs have the redder emission spectrum. This means that these photons are less likely to be reabsorbed by either fluorophore. Thus, in this construction, we minimize the chance of reabsorbing a photon. The other advantage of this construction is that the photons that are not absorbed by the QDs then encounter the dye layer. Here is a second chance for absorption, particularly in the 500-600 nm range where the QDs do not absorb strongly but the dye does (Figure 13a).

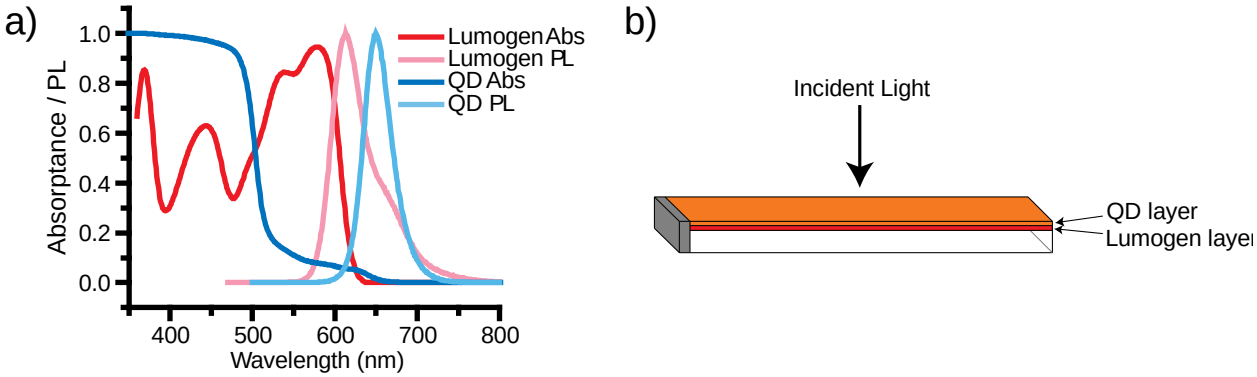

Figure 13. (a) Absorptance (dark colors) and photoluminescence (light colors) of Lumogen F Red 305 (red) and CdSe/CdS QDs (blue). The absorptance of Lumogen F Red 305 and CdSe/CdS QDs cover different parts of the electromagnetic spectrum, meaning that they can act complementarily to absorb a large fraction of the solar spectrum. In addition, each fluorophore's PL has a small overlap with the other fluorophore's absorptance. (b) Diagram of the two-layer device with a QD top layer and a Lumogen F Red 305 second layer. Light will be absorbed first by the QD layer to maximize the number of emitted photons in its longer-wavelength emission band compared to that of Lumogen F Red 305. Incident light between 500-600 nm that is not absorbed by the QDs will have a second chance to be absorbed by the Lumogen F Red 305.

We ran a Monte Carlo simulation for the performance of this two-layer LSC. We compared the efficiency at different distances for CdSe/CdS, Lumogen F Red 305, and two-layer LSCs (Figure 14). In the simulation, we excited each LSC with 405 nm light (where the QDs absorb strongly but the Lumogen does not) and with 578 nm light (where the Lumogen absorb strongly but the QDs do not). As anticipated, the QDs outperform Lumogen under 405 nm

excitation and Lumogen outperforms the QDs at 578 nm excitation due to absorbance. The two layer device performs slightly worse than the QDs under 405 nm excitation and slightly worse than Lumogen under 578 nm excitation because of the increased reabsorption from having two fluorophore layers. However, the two-layer device performs drastically better than the QDs under 578 nm excitation and drastically better than Lumogen under 405 nm excitation. On average over all wavelengths, the simulation predicts that the two-layer device will outperform a single-layer device of either fluorophore.

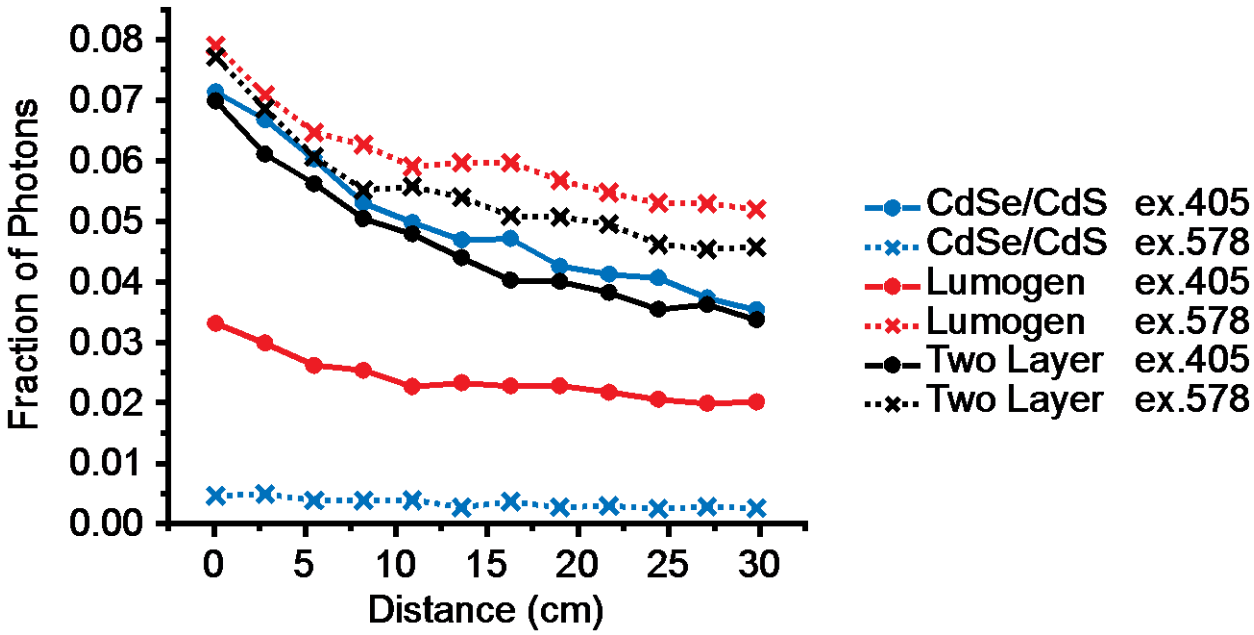

Figure 14. Results of Monte Carlo simulations of the efficiency of single-layer QD (blue), single-layer Lumogen (red), and two-layer (black) LSCs under 405 nm excitation (solid lines with circle point markers) and 578 nm excitation (dashed lines with x point markers). Under 405 nm excitation, the two-layer device does not perform as well as the QD-only device, and under 578 nm excitation, the two-layer device does not perform as well as the Lumogen-only device. However, the average performance under these two excitation wavelengths is better for the two-layer device than either single-layer device, predicting that the two-layer device will perform better under broadband excitation from the sun.

2.9 Conclusions

We invented a new polymer that interacts strongly with CdSe/CdS QDs as if it were a ligand. This is advantageous for thin-film LSCs because it allows for a high loading of the QDs in the thin film, creating a highly absorptive film that can absorb a large amount of sunlight. In addition, the polymer mimics the native ligands of the QDs, allowing for complete retention of their QY to maximize the number of absorbed photons that are then reemitted in the waveguide toward a solar cell. We developed a Monte Carlo simulation and found that our experimental results of LSC efficiency match the simulation well. We also compared the efficiencies of CdSe/CdS LSCs to Lumogen F Red 305 LSCs. Finding that they each have their own strengths, we designed a two-layer device using both fluorophores and used the Monte Carlo simulation to predict that the two-layer device will outperform a single-layer device of either fluorophore.

2.10 Experimental

2.10.1 CdSe/CdS Quantum Dot Synthesis

Quantum dots were synthesized by a modification of a previously-published method.

1. Oleic acid (3 mL), 1-octadecene (ODE, 3 mL), and 100 nmol of CdSe core QDs (with a maximum of the first excitonic feature in the absorbance spectrum at 591 nm) dissolved in hexane were added to a 100 mL 4-neck round-bottom flask. Oleylamine (3 mL) was added, and the solution was degassed at room temperature for 45 minutes and at 110 °C for 15 minutes.
2. The solution was then stirred under nitrogen and the temperature was raised to 310 °C.

3. At 200 °C, a solution of cadmium oleate (8 mL of a 0.2 M solution of cadmium oleate in ODE) dissolved in ODE (12 mL) and a separate solution of octanethiol (360 μL) dissolved in ODE (24 mL) were injected into the reaction flask at a rate of 2.5 mL/hr.
4. Portions of oleic acid (1 mL) were injected into the reaction mixture after reaction times of 1, 2, 3, 4, and 6 hours. Portions of oleylamine (1 mL) were injected into the reaction mixture after reaction times of 5 and 7 hours.
5. After 8 hours of reaction time, the reaction mixture was cooled to room temperature and the final product was isolated by precipitation with acetone.

2.10.2 Monomer Synthesis

The monomer was synthesized by a modification of the previously-reported Diels-Alder reaction between dicyclopentadiene and ethyl 10-undecenoate.[48]

1. Dicyclopentadiene (100.00g 0.756mol) and ethyl undecylenoate (220mL, 0.911mol) were added to a 450mL pressure vessel.
2. The temperature was raised to 170˚C and the sample was left to react for 20 hours under constant stirring.
3. The crude product mixture was placed in a refrigerator to induce the precipitation of a byproduct, which was then removed by filtration.
4. Under vacuum, the most volatile fractions with vapor temperature under 100 ˚C were distilled.
5. The residue was cooled to induce more precipitation which was removed by filtration.
6. A second distillation was performed to collect the product with vapor temperature of 120-130 ˚C.

7. The mixture was cooled again to precipitate and filter out solid impurities.
8. To a 1 M KOH (56 g) solution in methanol (1000 mL), the product from step 7 (65 mL) was added dropwise and the resulting solution was left stirring at room temperature for 4 hours.
9. Unreacted materials were then extracted away with hexanes (500mL, 3X) and discarded.
10. The methanol phase was acidified to pH 3 using concentrated HCl and the product was extracted into hexanes (1000mL, 3X).
11. The hexanes layer was dried over magnesium sulfate, filtered, and evaporated in vacuo to yield a white solid.

2.10.3 Polymer Synthesis

Grubbs third generation catalyst (2 mg) was dissolved in THF (2 mL) in a vial with a stir bar. The monomer (0.566 g) was dissolved in THF (2 mL) and injected into the stirring solution of Grubbs catalyst. After 30 minutes, the reaction was quenched with a few drops of ethyl vinyl ether. More THF (4 mL) was added, along with Quadrasil MP metal scavenger (2 g). The mixture was stirred for 4 hours to complex the Grubbs catalyst to the metal scavenger. The metal scavenger was then removed by filtration through a syringe filter. The polymer was isolated by precipitation with hexanes and dried under vacuum.

2.10.4 Composite Preparation

The QD/polymer composite was prepared by mixing equal volumes of a 2.5 mg/mL solution of QDs in tetrahydrofuran and a 75 mg/mL solution of the polymer in tetrahydrofuran.

The final composite solution was prepared by removing tetrahydrofuran and dissolving in one-quarter the amount of 1,4-dioxane, followed by filtration through a syringe filter.

2.10.5 Device Fabrication

Poly(methyl methacrylate) substrates were prepared by cutting to the desired dimensions with a CO_2 laser cutter, followed by annealing at 80 °C overnight and cooling to room temperature at 10 °C/hour. The substrate was placed in a homemade box. The solution of composite in dioxane was dropcast over the entire area of the device. In order to cover a 30x2.3 cm substrate, 8 mL of the composite solution in dioxane was dropcast. The box was sealed to slow the evaporation rate of dioxane to allow for the formation of uniform films.

Chapter 3: Large Indium Phosphide Quantum Dots

Portions of this chapter were adapted with permission from Achorn, O. B.; Franke, D.; Bawendi, M. G. Seedless Continuous Injection Synthesis of Indium Phosphide Quantum Dots as a Route to Large Size and Low Size Dispersity. *Chem. Mater.* **2020**, *32*, 6532–6539.

3.1 Introduction

Quantum dots (QDs) are useful fluorophores in applications that require broadband light absorption, such as LSCs. QDs are also useful for applications that require narrowband luminescence, such as LEDs and displays. Cadmium selenide (CdSe) QDs, while exhibiting broad spectral tunability and narrow ensemble emission linewidths, are problematic for commercial applications because of their potential toxicity. Indium phosphide (InP) QDs are less toxic alternatives, but they generally suffer from less facile access to red wavelengths and narrow ensemble emission spectra. These two effects are not intrinsic to InP QDs. In fact, InP has a narrower bulk bandgap than CdSe does and the single-nanocrystal emission linewidth of InP QDs is similar to that of CdSe QDs.[49] Thus, the shorter wavelengths of InP absorption spectra are due to the difficulties in synthesizing large InP QDs, and the broader linewidths of InP QD ensemble emission spectra are due to the difficulties in synthesizing ensembles with low size dispersity.

There is still an incomplete understanding of the nucleation and growth mechanisms of InP QDs, and this limits the possibilities for the rational design of better synthetic methods that lead to larger sizes and lower size dispersities. Syntheses for III-V semiconductor QDs, including those for InP QDs, have usually been modeled after the syntheses for II-VI semiconductor QDs, which were designed based on the mechanism of colloid growth proposed by LaMer.[50] In the LaMer

model, a rapid increase in the concentration of monomers is followed by a discrete nucleation event, which is then followed by size-focusing growth of the nuclei from the remaining monomers.[51] The most popular synthetic methods that are used to take advantage of the LaMer model can be broadly grouped into hot-injection syntheses, in which one precursor is rapidly injected into a high-temperature solution of the other precursor,[52] and heat-up syntheses, in which both precursors are mixed at low temperature and then heated up to the reaction temperature.[53] In both cases, all of the precursors experience nucleation conditions at the same time, allowing all of the nuclei to form simultaneously and separately from the size-focusing growth stage. While II-VI QD growth aligns qualitatively with the LaMer model, evidence suggests that InP QD growth does not follow the same process.

The mechanism of InP QD growth has been found to differ from that of II-VI QDs due in part to the greater reactivity of the anion precursor.[54] The high anion precursor reactivity leads to the rapid depletion of precursors, which prevents the size-focusing growth of the nuclei from monomers later in the reaction.[50,51,55] This, in turn, restricts the formation of large and monodisperse InP QDs. Previous attempts at increasing the size and decreasing the size dispersity of InP QDs include the use of less reactive phosphorus precursors with the aim of reserving some precursors to form monomers for further growth after the nucleation event is complete. However, this has led to minimal success due to the persistent difficulty of separating nucleation and growth in time.[56–58,59,60] More successful strategies include secondary injections and continuous injections of precursors, in which additional precursors are added to the reaction mixture after nanocrystal "seeds" are produced by an initial rapid hot-injection or heat-up approach.[61,62–66] These methods were designed to control the supply of monomers externally. For example, a syringe-pump-mediated seeded continuous injection synthesis of III-V QDs was used by Franke et al.,

specifically for indium arsenide (InAs) QDs.[62] This study demonstrates how a continuous external supply of precursors can be used to compensate for their high reactivity and effectively extend the growth of III-V QDs while keeping their size dispersity low.

Another possible reason for the deviation of InP QD growth from the LaMer model is the existence of kinetically persistent intermediates that build up during the reaction.[67–70] The group of Cossairt has isolated 1.3 nm InP nanoclusters, implicated them as kinetically persistent intermediates in InP QD growth, and used them as precursors for the hot-injection synthesis of InP QDs.[67–69] Additionally, the group of Jensen has identified small clusters with masses of about 10 kDa that persist throughout the course of InP QD growth.[70] In order to achieve larger and more monodisperse InP QDs, new synthetic methods must take into account the existence of these kinetically persistent intermediates.

Another strategy in the improvement of InP QD syntheses is the incorporation of zinc ions. Incorporation of zinc in InP QD syntheses appears to lead to QDs with narrower absorption and PL spectra, shorter wavelengths for the absorption and PL features, and higher QY. There is disagreement in the community about the mechanism of these effects. One common explanation is that zinc is incorporated into the interior of the crystal, forming an In(Zn)P alloy. A second common explanation is that the zinc binds to the surface of the QDs, acting as a ligand and passivating dangling bonds.[71] This explanation is attractive based on arguments of sterics and coordination spheres. Indium, as a +3 ion, requires three carboxylate ligands for charge balance. However, three ligands is a high steric demand for atoms on the surface of a QD. Thus, it can be energetically favorable for indium to be undercoordinated at the surface. This leaves dangling bonds at the surface that act as electron traps. Zinc, on the other hand, is a +2 ion, so there is less of a steric barrier to its full passivation. Zinc carboxylates may displace undercoordinated surface

indium atoms and remove the associated electron traps. The third explanation for the role of zinc in the improvement of InP QDs is that it may play a role in the reaction kinetics.[72] The existence of a second metal (Zn in addition to In) in the reaction mixture adds a competing pathway for the conversion of the phosphorus precursor. It may be that the first step in the reaction is the formation of a Zn-P complex, which has a lower reactivity than the phosphorus precursor.

In this work, we developed several new continuous injection strategies for the synthesis of InP QDs that allow us to access continuous growth to achieve large sizes of InP QDs. This is a necessary step in developing InP QDs for use as broadband absorbing fluorophores in LSCs. An added benefit is that our synthetic techniques produce InP QDs with narrow size distributions, and hence narrow photoluminescence (PL) spectra, which makes them attractive for narrow-band light emission applications such as displays and LEDs. We started with seeded continuous injection methods based on the InAs work of Franke. After we started working on these methods, seeded continuous injection (and similar) syntheses of InP QDs were published by Ramasamy et al.[63,64], Won et al.[66], and Xu et al.[65] We then switched focus to develop a seedless continuous injection method.

3.2 Seeded Continuous Injection

3.2.1 Constant-Rate Seeded Continuous Injection

In order to extend InP QD growth beyond what is possible from a traditional hot-injection synthesis, we designed a new synthesis in which additional precursors are added to the reaction mixture after seeds are created by a hot injection. In our first synthesis, we started with enough indium for the hot injection and continuous injection in the reaction flask. For the nucleation step, 17% of the total amount of phosphorus was used in a hot injection. Then, the remaining 83% of

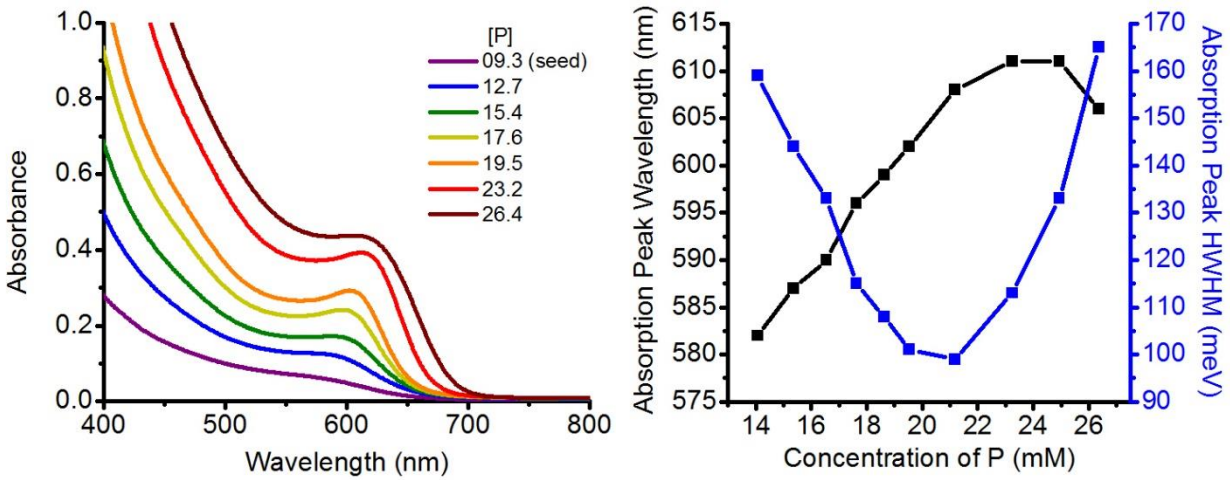

Figure 15. (a) Absorption spectra of aliquots taken during the constant-rate seeded continuous injection synthesis of InP QDs. (b) The absorption peak wavelength (black) and HWHM (blue) of the aliquots as a function of the concentration phosphorus in the reaction mixture. This graph indicates that there is an initial period of growth and size focusing, followed by size stagnation and defocusing. We hypothesize that the size defocuses because the injection rate is too high.

the phosphorus precursor was supplied dropwise by a syringe pump. After the hot injection, the absorption spectrum of the seeds was broad with only a shoulder instead of a distinct peak for the first excitonic transition, indicating a broad size distribution (Figure 15). During the continuous injection, we took aliquots from the reaction mixture at 10-minute intervals. The absorption spectrum of the first aliquot was very similar to that of the seed except that the absorbance was greater. By the second aliquot, the absorption shoulder had become more prominent, and by the third aliquot, a local maximum had emerged for the first excitonic absorption feature. For the rest of the growth, we used this absorption feature (its wavelength and width) to characterize the growth progress. The absorption peak wavelength increased for most of the reaction, indicating QD growth. Meanwhile, the absorption peak half width at half maximum (HWHM) decreased for the first 120 min, indicating a narrowing size distribution. In the later stages of the reaction, the peak wavelength plateaued and the HWHM increased, indicating that the QDs stopped growing and the size distribution became broader.

3.2.2 Variable-Rate Seeded Continuous Injection

We hypothesized that the broadening in late stages of the continuous injection was due to the high injection rate. Thus, in our next synthesis we modulated the injection rate to prevent the broadening. Given that the previous experiment worked well at early times, we used the same rate for the initial stage of the continuous injection. Again, we monitored the absorption peak wavelength and HWHM. The absorption peak continued to redshift until 0.2 mmol of phosphorus had been added, and the HWHM continued to decrease until 0.16 mmol of phosphorus had been added, after which point it started to increase (Figure 16). Thus, after 0.22 mmol of phosphorus had been added, we slowed the injection rate from 1 mL/h to 0.3 mL/h. After slowing the injection rate, the peak wavelength began to redshift again, indicating that the average size of the QDs began increasing again. In addition, the HWHM narrowed slightly before broadening again. After slowing the injection rate from 0.3 mL/h to 0.2 mL/h, the HWHM narrowed slightly again before increasing drastically. These results demonstrate that control of the injection rate can be used to keep the QDs in a growth and size focusing regime. We hypothesize that injection rates that are

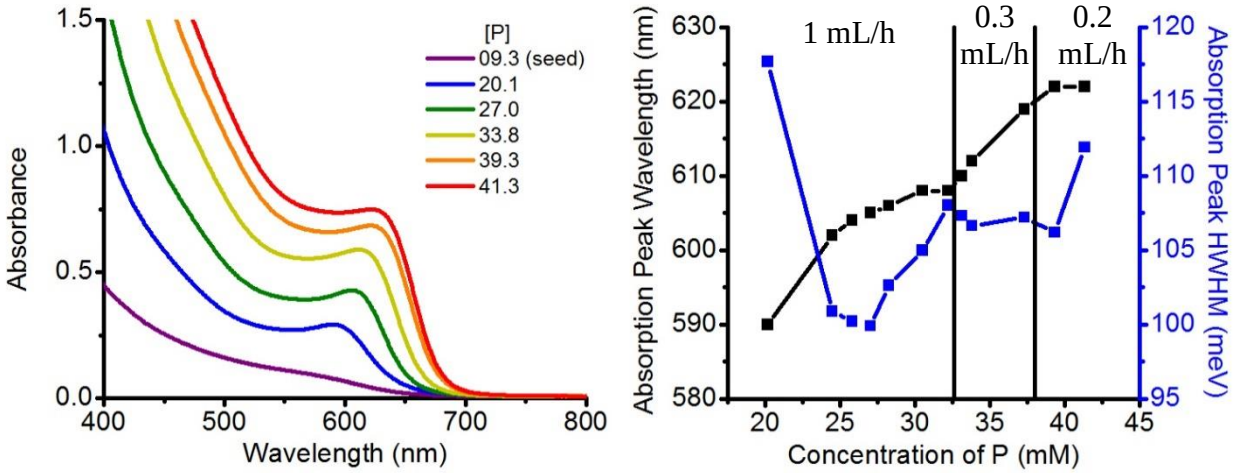

Figure 16. (a) Absorption spectra of aliquots taken during the variable-rate seeded continuous injection synthesis of InP QDs. (b) The absorption peak wavelength (black) and HWHM (blue) of the aliquots as a function of the concentration phosphorus in the reaction mixture. This graph indicates that slower injection rates aid in QD growth and size focusing.

too fast lead to excessive nucleation of new QDs. This would prevent the existing QDs from growing, and it would cause the size distribution to broaden. By slowing the injection rate, we can shift the balance away from nucleation and toward growth and size focusing of the existing QDs. Better results could likely be achieved by slowing the injection rate preemptively before the size distribution started to broaden. Before working on this, though, we wanted to improve the initial size distribution of the seeds.

3.2.3 Stoichiometric Seeded Continuous Injection

In the previous two reactions, the seeds had broad absorption spectra with no distinct local maxima. This indicates that the seeds started out with high size dispersity which had to be overcome during the continuous injection step. We wanted to instead start with seeds of low dispersity to see if continuous injection could lead to even narrower size dispersity. We hypothesized that high size dispersity of the seeds was caused by the high concentration of indium in the hot-injection step. Thus, we modified our synthesis to produce high-quality seeds by including a more traditional hot injection with a nearly stoichiometric P:In ratio.

In our new method, we adjusted the P:In atomic ratio of the hot-injection step to be nearly stoichiometric at 1:1.2. As expected, these reaction conditions led to seeds with narrow absorption spectra (Figure 17). During the continuous injection step, TMS_3P and indium oleate were both loaded into two separate syringes and injected into the reaction mixture, again at a 1:1.2 ratio. This led to steady redshifting and narrowing of the absorption spectra.

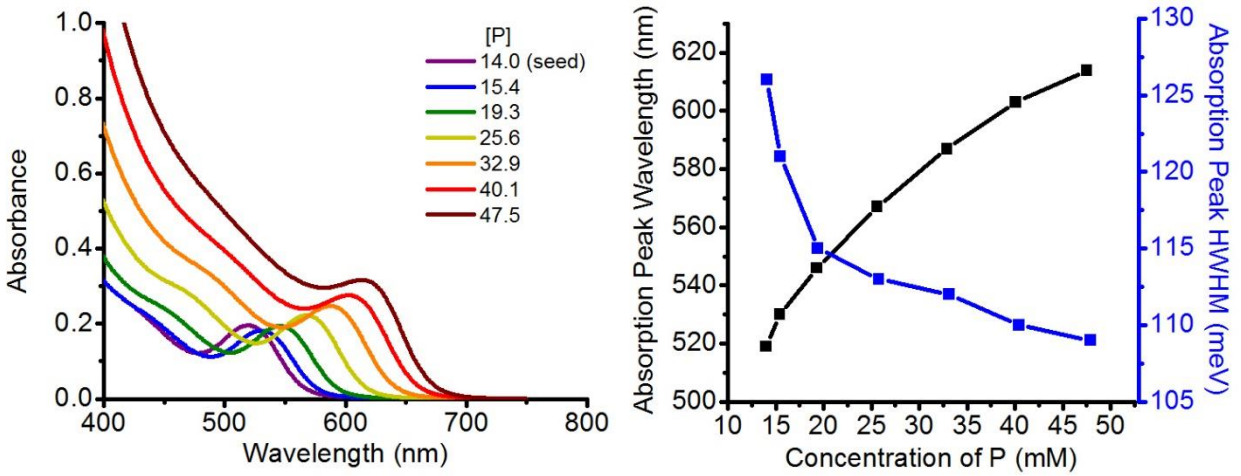

Figure 17. (a) Absorption spectra of aliquots taken during the stoichiometric seeded continuous injection synthesis of InP QDs. (b) The absorption peak wavelength (black) and HWHM (blue) of the aliquots as a function of the concentration phosphorus in the reaction mixture. Despite the narrower size distribution of the seeds, the final HWHM is not narrower than in the indium-rich reactions.

Even though, compared to the indium-rich reaction, the stoichiometric reaction had more monodisperse seeds, a more steadily increasing absorption peak wavelength, and a more steadily decreasing HWHM, the maximum absorption peak wavelength was not longer and the minimum HWHM was not narrower than in the indium-rich reaction. While there is still room for optimization of both of these synthetic methods, our results suggest that control of the injection rate is more important than the quality of the seeds in order to synthesize large InP QDs with low size dispersity.

3.2.4 Quantum Dot Concentration

The absorption spectra of successive aliquots in the indium-rich reactions increase in absorbance more drastically than successive aliquots in the stoichiometric reaction. This suggests that the concentration of QDs increases throughout the course of the continuous injection, at least for the indium-rich reaction. We estimated the concentration of QDs in the reaction mixture for an indium-rich reaction and a stoichiometric reaction by first measuring the absorbance at 350 nm

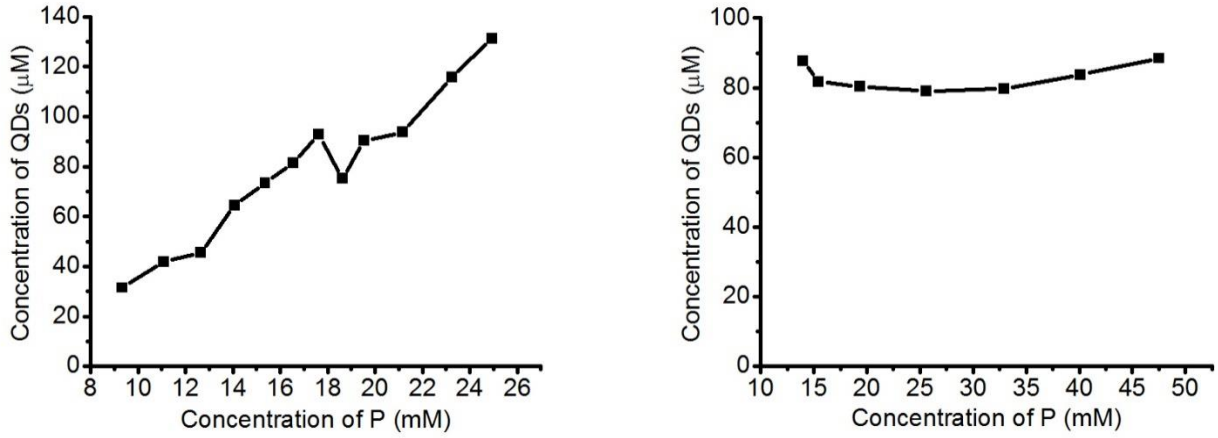

Figure 18. Concentration of QDs as a function of the concentration of phosphorus in the reaction mixture for (a) indium-rich reaction and (b) stoichiometric reaction. The relatively constant concentration of QDs in the stoichiometric reaction indicates that the continuously injected precursors add to the existing QDs from the hot injection. The increasing concentration of QDs in the indium-rich reaction indicates that nucleation of new QDs accompanies the growth of existing QDs during the whole reaction. Combined with Figure 15 and Figure 16, this indicates that separation of the nucleation and growth events is not necessary in order to achieve a narrowing size distribution.

and the wavelength of the absorption peak of each aliquot. The absorbance at 350 nm was used to calculate the concentration of InP units in the mixture, and the wavelength of the absorption peak was used the calculate the number of InP units per QD. The concentration of QDs was then estimated by dividing the concentration of InP units by the number of InP units per QD. Indeed, as shown in Figure 18 a and b, the concentration of QDs increases for the indium-rich reaction but stays relatively constant for the stoichiometric reaction. This highlights a major mechanistic difference between the two cases. The stoichiometric reaction appears to follow the LaMer-type mechanism that it was designed for. Specifically, nucleation is confined to the brief hot injection step at the beginning of the synthesis, and growth occurs during the rest of the synthesis during the continuous injection step. During the growth stage, the precursors from the continuous injection add to the existing QDs. On the other hand, in the indium-rich reaction, nucleation and growth happen simultaneously and continuously over the course of the entire synthesis. Given a traditional understanding of QD nucleation and growth, this should lead to a continuously broadening size

distribution because QDs nucleated at different times would have different amounts of time to grow. Surprisingly, as shown in Figure 15.b and Figure 16.b, there are still periods of size focusing during these continuous-nucleation reactions. Moreover, it is possible that, by optimizing the continuous injection rate, size-focusing could accompany growth throughout the entire reaction. Before investigating this further, we made two more observations. Firstly, the fact that nucleation occurs throughout the reaction implies that nucleation can be initiated by the continuous injection and that an initial hot injection is not necessary for nucleation. Secondly, given that the concentration of QD seeds from the hot-injection step is such a small fraction of the final QD concentration, we hypothesize that these seeds have little impact on the overall course of the reaction and the final properties of the ensemble. Thus, we continued our investigation into this matter by designing and studying a seedless continuous injection synthesis.

3.3 Seedless Continuous Injection

The traditional belief is that a hot-injection or a heat-up step is required in the synthesis of monodisperse QDs. However, the minimal effect of the seeds on the final product in the indium-rich seeded continuous injection reaction suggest that this may not be the case. Thus, we designed a new method for the synthesis of InP QDs based on a continuous injection of precursors into a reaction flask but without the existence of seeds from an initial hot-injection or heat-up step. In this novel seedless continuous injection synthesis of InP QDs, a slow injection of the phosphorus precursor in a single continuous injection step induces QD nucleation, growth, and size focusing. We controlled the injection rate in order to control the concentration of kinetically persistent intermediates to prevent unwanted nucleation events. This allowed us to extend growth to achieve

large InP QDs with absorption spectra as far red as 630 nm and to extend size focusing to achieve a PL spectrum as narrow as 53 nm.

3.3.1 Constant-Rate Seedless Continuous Injection

In our first synthesis, we performed the continuous injection at a constant rate. Specifically, we began with 3 mL of a degassed 27 mM solution of indium oleate in 1-octadecene (ODE) at 300 °C, into which an 85 mM solution of tris(trimethylsilyl)phosphine [$(TMS)_3P$] in ODE was injected by a syringe pump at 0.2 mL/h. Enough of the TMS_3P solution was prepared so that when all of it was injected, the ratio of indium to phosphorus in the reaction flask would be 1.2:1. This ensures an excess of ligands to stabilize the QDs. In order to monitor the growth process, we sampled equivolume aliquots from the reaction mixture at regular intervals, diluted them by a constant factor in hexanes, and recorded their absorption spectra. We relate our observations to the total concentration of phosphorus in the solution, which was determined by the amount of $(TMS)_3P$ that had been injected and the volume of the reaction solution.

A local maximum corresponding to the first excitonic transition (hereafter referred to as the absorption peak) appeared in the absorption spectrum by the time phosphorus reached 5.3 mM (0.21 equiv of P with respect to In), as shown in Figure 19.a. The existence of this absorption feature indicates that QDs had nucleated, and the definition of the peak indicates that, despite the lack of a rapid hot injection, the QDs had a relatively low size dispersity. By the time phosphorus reached 7.7 mM (0.32 equiv), the absorption peak had redshifted. This is the expected result of a continuous injection process, in which continuously supplied precursors promote the growth of existing QDs in the solution.[62,64] During the stage of the reaction when phosphorus was at a concentration between 7.7 mM (0.32 equiv) and 12.1 mM (0.53 equiv), the wavelength of the

absorption peak changed minimally, indicating that the growth of the existing QDs had slowed significantly. This slowing growth rate may be the result of the lower surface energy of larger QDs, the oxidation of the surface of the QDs by carboxylates or water in the reaction mixture, or changes in surface bonding.[73–76]

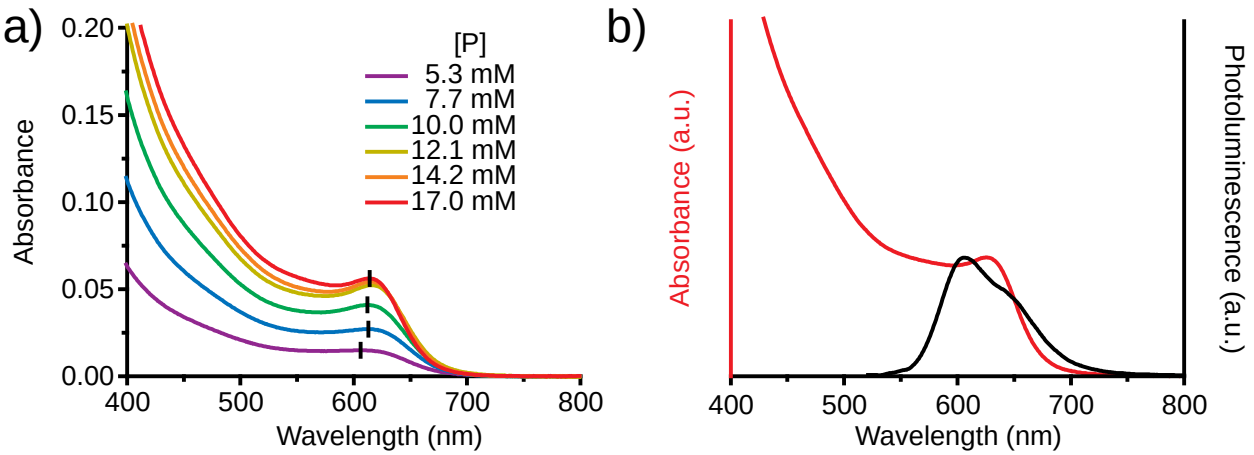

Figure 19. (a) Absorption spectra of aliquots taken throughout the constant-rate seedless continuous injection reaction. The legend indicates the concentration of phosphorus in the reaction mixture when each aliquot was taken. The absorption peaks are marked with black tick marks. The trends in absorbance and peak wavelength suggest that the QDs increase in concentration throughout most of the reaction and increase in size only at the beginning. (b) Absorption and PL spectra of InP/ZnSe core/shell QDs after growing a ZnSe shell on the final product of the reaction in (a). The PL peak at shorter wavelength than the absorption peak indicates the presence of a secondary population of smaller QDs.

The concentration of QDs in the reaction mixture was calculated by measuring the absorbance of the aliquots at 350 nm to determine the concentration of InP units and by measuring the wavelength of the absorption peak to determine the size of the QDs. First, the concentration of InP units (c_{InP}, in M) in the reaction mixture was determined by using the Beer-Lambert law with the absorbance of the diluted aliquots at 350 nm (A_{350}), the size-independent molar extinction coefficient of InP units ($\varepsilon_{350} = 3700\ \mathrm{M^{-1}cm^{-1}}$),[77] the path length of the cuvette ($\ell = 1.00$ cm), and the dilution factor of the aliquot ($D = 61$).

$$c_{\mathrm{InP}} = \frac{A_{350}}{\varepsilon_{350}\ell} \cdot D$$

Next, the diameter (d, in nm) of the QDs was determined by using the wavelength (λ, in nm) of the absorption peak and the following fit to the data in reference 77:

$$d = 0.02124\lambda - 9.251$$

The number of InP units per QD (N_{InP}) was determined by assuming spherical QDs and using the diameter (d, in nm) of the QDs and the bulk lattice parameter ($a = 0.58687$ nm) of zincblende InP.[78] The volume of a sphere is $V_{\mathrm{sphere}} = \frac{4\pi}{3}\left(\frac{d}{2}\right)^3$, the volume of a unit cell is $V_{\mathrm{unit\,cell}} = a^3$, and there are 4 InP units per unit cell, so we used the following equation:

$$N_{\mathrm{InP}} = \frac{2\pi}{3}\left(\frac{d}{a}\right)^3$$

Finally, the concentration of QDs (c_{QD}, in M) in the reaction mixture was calculated by dividing the concentration of InP units (c_{InP} in M) by the number of InP units per QD (N_{InP}).

$$c_{\mathrm{QD}} = \frac{c_{\mathrm{InP}}}{N_{\mathrm{InP}}}$$

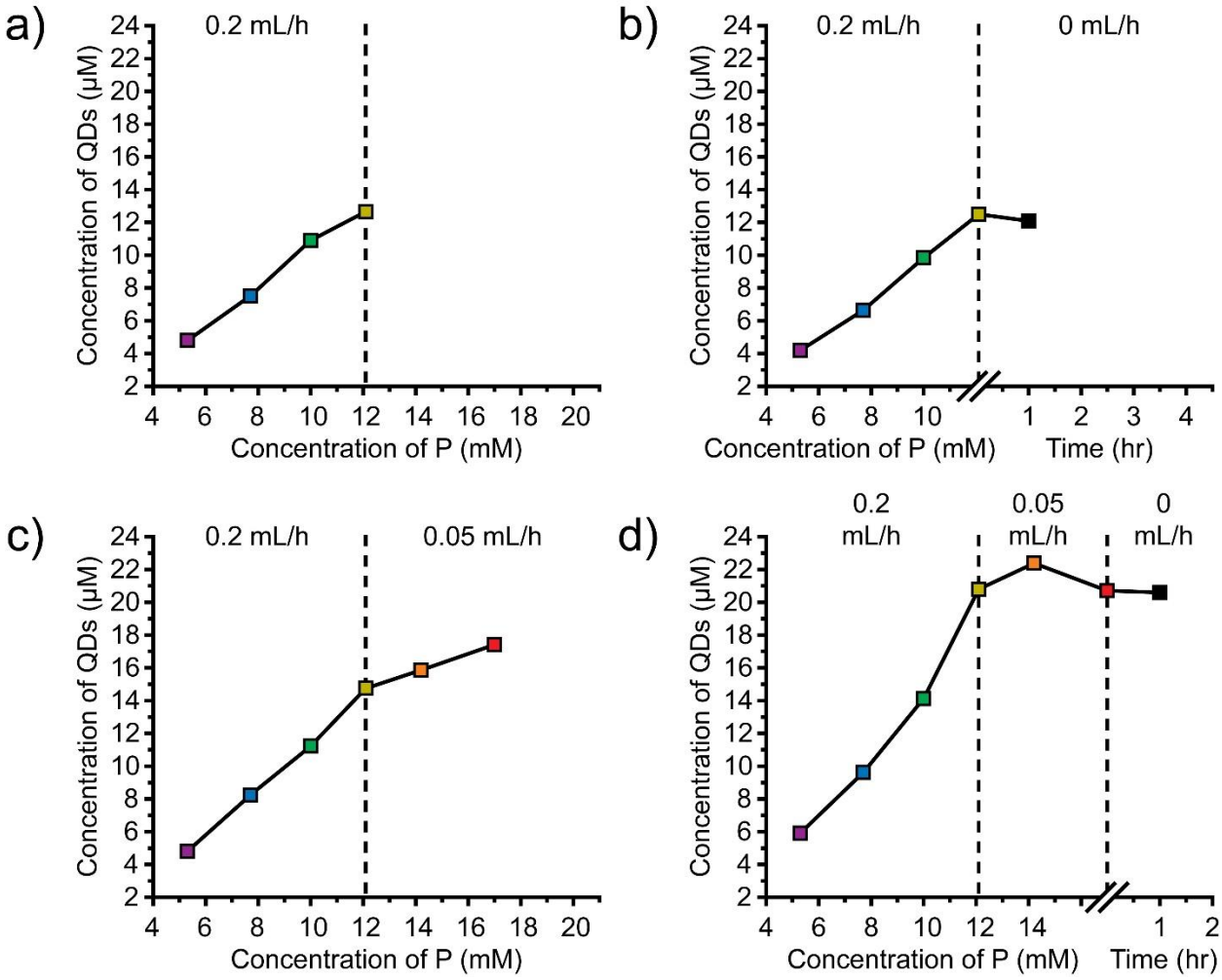

Figure 20. The concentration of QDs in the reaction mixture as the reaction progressed for (a) constant-rate injection, (b) interrupted injection with subsequent annealing, (c) variable-rate injection, and (d) variable-rate injection with subsequent annealing. Reaction progress is defined in terms of the concentration of phosphorus in the reaction mixture. For (b) and (d), a break in the *x*-axis indicates when the injection was stopped and the anneal step began. To the right of the break, reaction progress is defined in terms of time. For (c) and (d), dotted vertical lines at 12.1 mM indicate when the injection rate was changed from 0.2 mL/h to 0.05 mL/h. For (a), the concentration of QDs was not calculated after the secondary nucleation event because the existence of two populations of QDs of different sizes made such a calculation impossible. These graphs show that, in each reaction, the concentration of QDs increased during the 0.2 mL/h injection stage. During annealing steps with no precursor injection (b and d), no new QDs nucleated, so the concentration stayed relatively constant. For variable-rate injection reactions (c and d), after the injection rate was slowed down to 0.05 mL/h, the concentration of QDs either stayed relatively constant or increased at a slower rate.

We determined that the concentration of QDs increased approximately linearly throughout the reaction until phosphorus reached a concentration of 12.1 mM (see Figure 20.a). This suggests

that in the absence of a hot injection, QDs nucleate continuously during the continuous injection instead of all at once at the beginning of the reaction. Meanwhile, the half width at half maximum (HWHM) of the absorption peak continued to decrease (Figure 21.a). Because these QDs are within a size regime in which the bandgap energy depends linearly on size,[77] the narrowing HWHM is indicative of a narrowing size distribution. This narrowing size distribution, which

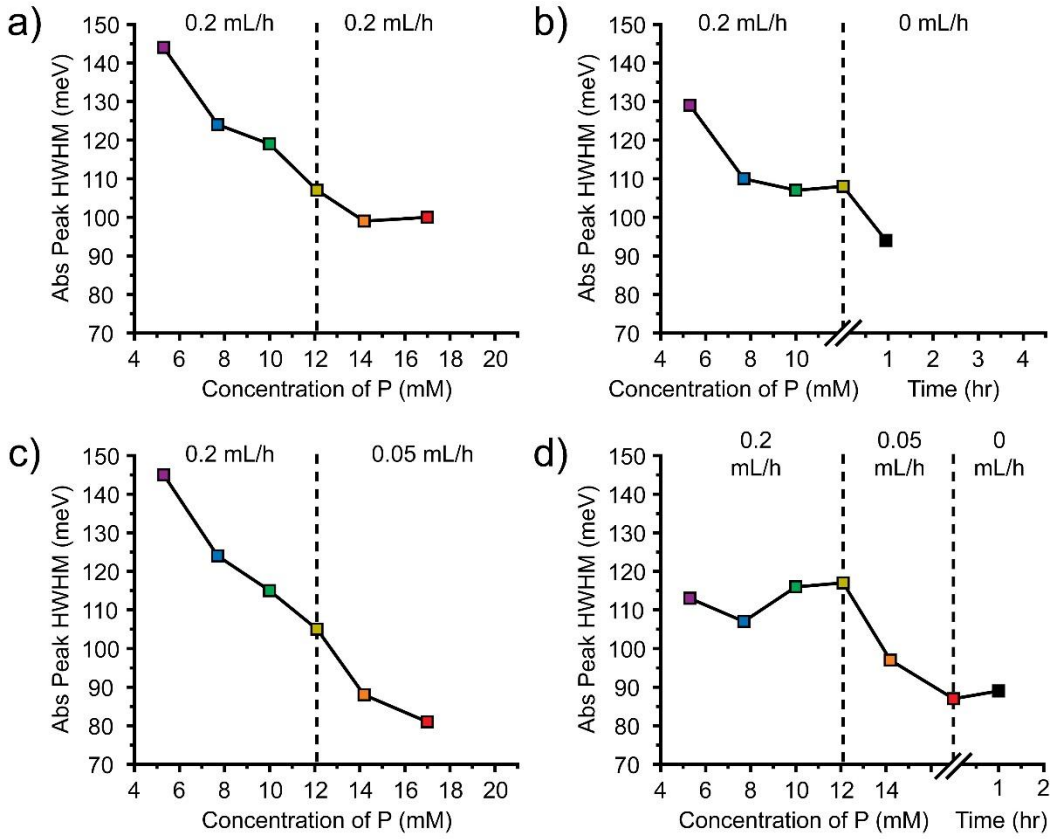

Figure 21. The evolution of the absorption peak half width at half maximum (HWHM) as the reaction progressed for (a) constant-rate injection, (b) interrupted injection with subsequent annealing, (c) variable-rate injection, and (d) variable-rate injection with subsequent annealing. Reaction progress is defined in terms of the concentration of phosphorus in the reaction mixture. For (b) and (d), a break in the *x*-axis indicates when the injection was stopped. To the right of the break, reaction progress is defined in terms of time. For (c) and (d), dotted vertical lines at 12.1 mM indicate when the injection rate was changed from 0.2 mL/h to 0.05 mL/h. There is some batch-to-batch variation in the HWHM data, but the general trends are what is important, and they are reproducible. The HWHM generally decreases for all reactions, with the especially important trend that the HWHM decreases more significantly after the injection is stopped or slowed compared to when it is held constant beyond a phosphorus concentration of 12.1 mM. This suggests that the slower injection rates allow for more size focusing as the concentration of intermediates decreases.

occurs despite the continuous nucleation of new QDs, can be explained based on the slowing growth rate of the QDs as they grow larger, which allows the newly nucleated smaller QDs to catch up in size.[79] Continuous nucleation has also been observed in hot-injection syntheses, and it has been found to not have a negative impact on the breadth of the absorption features.[80,81]

The final absorption spectrum in Figure 19.a has a relatively narrow HWHM (100 meV), but a better representation of the size distribution comes from the FWHM of the PL spectrum. The InP core-only QDs that were produced by this reaction were not emissive, so we grew a thin zinc selenide (ZnSe) shell on them in order to characterize the width of their PL spectra. Shell growth revealed a PL FWHM (80 nm, 257 meV) that is much greater than what would be expected from the HWHM (31 nm, 94 meV) of the absorption peak of the core/shell QDs (Figure 19.b). In addition, the PL maximum is at a shorter wavelength than the absorption maximum, and there is a shoulder on its long-wavelength side. These observations indicate that there were two distinct populations of QDs in the sample. Of these two populations, the larger QDs were likely in a higher concentration, so they dominate the absorption spectrum. On the other hand, the smaller QDs were likely brighter than the larger ones, so they dominate the PL spectrum.

We confirmed the presence of two separate populations by synthesizing a new sample and separating it by a size-selective precipitation. We then compared the absorption and PL spectra of the full batch to those of the precipitate and supernatant after the size-selective precipitation (Figure 22). The absorption spectrum of the precipitate looks very similar to that of the full batch, suggesting that these QDs make up the majority of the sample. On the other hand, the absorption spectrum of the supernatant is broader and at shorter wavelengths. The population of QDs in the supernatant contributes to the difference in VPR (but not much to a difference in HWHM) between the spectra of the full batch and the precipitate. Similarly, the PL spectrum of the supernatant is

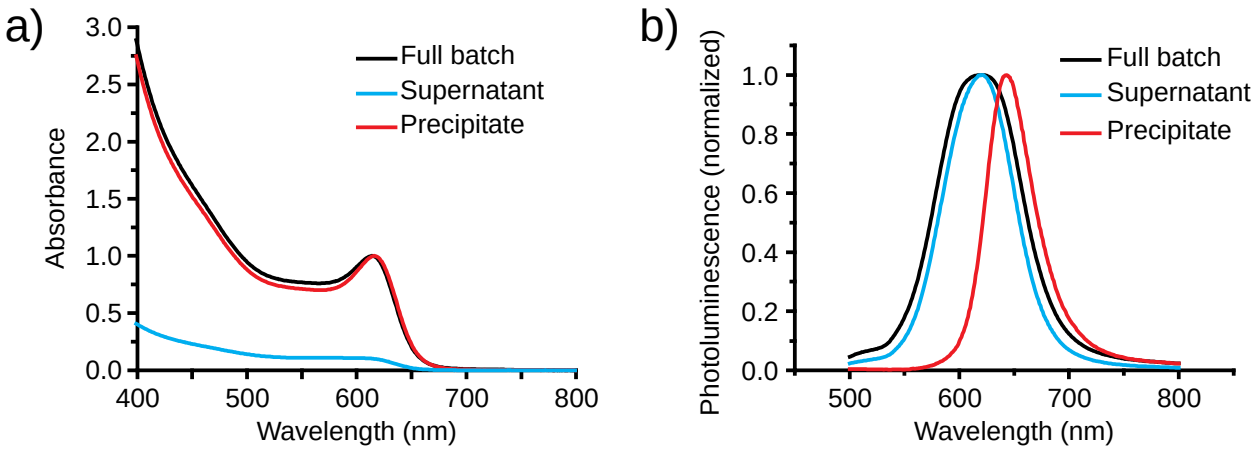

Figure 22. (a) Absorption spectra of the full batch and of the supernatant and precipitate after the size-selective precipitation of In(Zn)P/ZnSe QDs prepared by seedless continuous injection and subsequent shell growth. The absorption peaks for the full batch and the precipitate are normalized to an absorbance of 1. The absorbance of the supernatant is scaled to match the difference between the absorbance of the full batch and the precipitate. (b) Normalized photoluminescence spectra of the full batch and of the supernatant and precipitate after size-selective precipitation. These spectra indicate that the full batch is composed of a majority population of large QDs of low size dispersity and a minority population of small QDs of high size dispersity.

also broader and at shorter wavelength than that of the precipitate, indicating that the supernatant is composed of smaller QDs with a broader distribution of QD sizes. The similarity between the spectra of the supernatant and the full batch suggests that the QDs in the supernatant are brighter than the QDs in the precipitate and more responsible for the breadth of the spectrum of the full batch. The long wavelength (643 nm) and narrow FWHM (51 nm) of the precipitate's spectrum indicate that the precipitate is composed of large QDs of low size dispersity. By removing the population of smaller and more polydisperse QDs from the full batch, only the population of large, monodisperse QDs is left with its narrow optical spectra. This suggests that our seedless continuous injection synthesis can produce InP QD ensembles with narrow optical features if the formation of the population of smaller QDs can be prevented.

In order to prevent the formation of the population of smaller QDs, we first needed to determine when it formed by monitoring the valley/peak ratio (VPR) of the absorption spectra, for which the valley is the local minimum at shorter wavelengths than the peak.[65] In this case, we take

an increase in the VPR to indicate an increase in the concentration of small QDs, which absorb light at the wavelengths of the valley (but not the peak) of the main population of large QDs. For the absorption spectra of the InP QDs during the constant-rate injection growth, reproduced in Figure 23.a.i, the VPR (Figure 23.a.ii) decreased until the phosphorus concentration reached 12.1 mM (0.53 equiv), after which the VPR increased. We hypothesize that this is the point at which the secondary population of smaller QDs formed. Moreover, we hypothesize that this secondary population formed because of an increasing concentration of reaction intermediates, which may be the magic-sized clusters described by others[67–70] or any other persistent InP-containing species that are smaller than QDs. If the nucleation rate is dependent on the concentration of these intermediates, then a critical concentration of intermediates would induce this secondary nucleation.

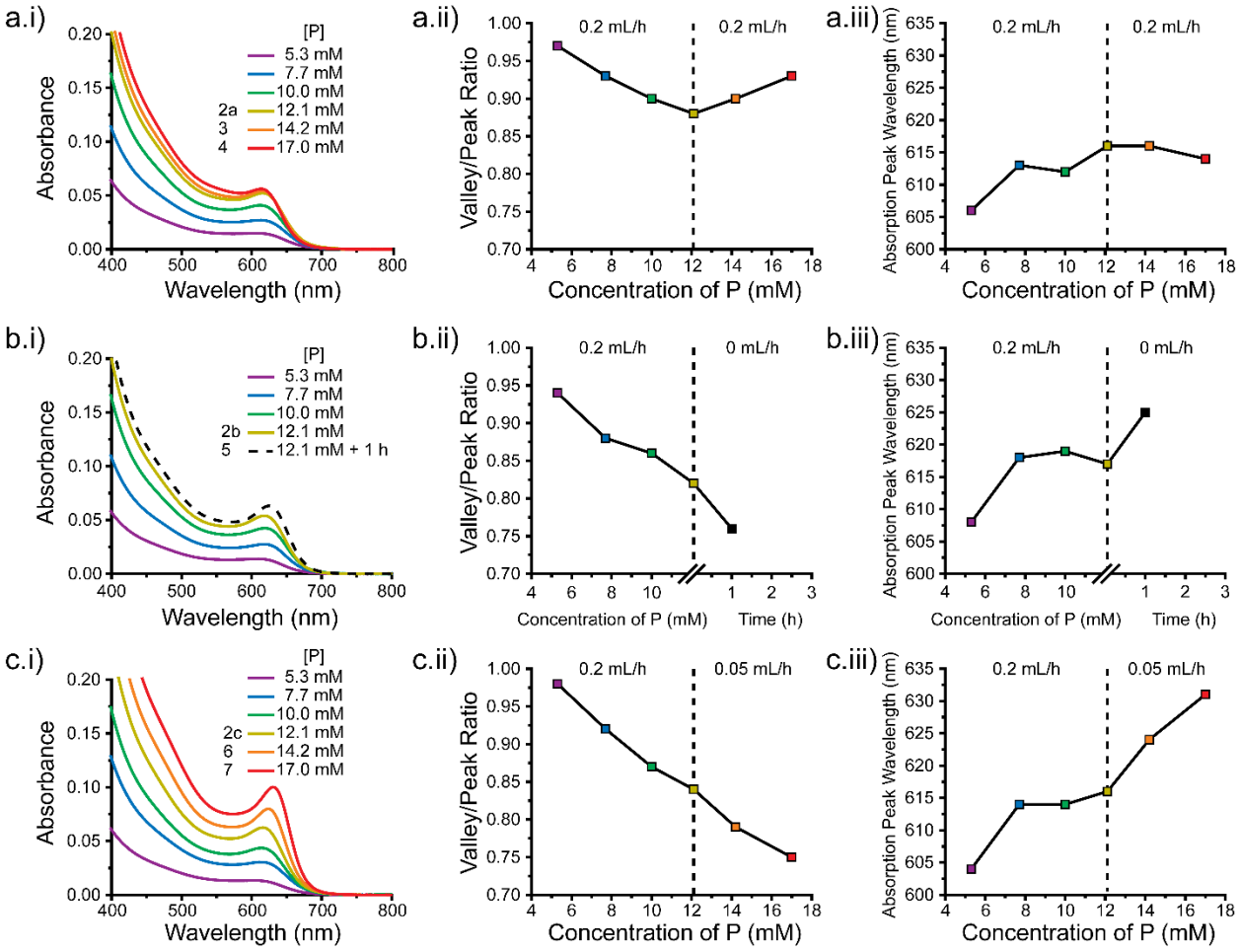

Figure 23. Absorption spectra of aliquots taken throughout InP QD growth under conditions of (a.i) constant-rate, (b.i) interrupted, and (c.i) variable-rate seedless continuous injection. In the legends, the numbers on the right indicate concentrations of phosphorus, and the numbers on the left correspond to the numbered flasks in Figure 24. For each series (a-c), (i) is the full absorption spectra, (ii) is the VPR at different phosphorus concentrations, and (iii) is the absorption peak wavelength at different phosphorus concentrations. The colored points in (ii) and (iii) correspond to the colored traces in (i). For (a.ii) and (a.iii), the injection rate is the same on both sides of the vertical dotted line. For (b.ii) and (b.iii), the vertical dotted line indicates when the injection was interrupted. To the right of the vertical line, the *x*-axis measures time instead of phosphorus concentration. For (c.ii) and (c.iii), the vertical dotted line indicates when the injection rate was changed from 0.2 mL/h to 0.05 mL/h. These graphs show that during a constant-rate injection, a secondary population of smaller QDs eventually grows at the expense of the continuous growth of the main population. Interrupting or slowing the injection at the right time prevents the formation of the secondary population and allows for the continuous size focusing and growth of the existing QDs.

Here, we make a distinction between continuous nucleation and secondary nucleation based on relative rates. At the beginning of a seedless continuous injection reaction, when only a small amount of the precursor solution has been injected, the concentration of intermediates is low. Thus, the rate of nucleation is slow compared to the rate of growth of existing QDs, so the QDs grow to large sizes instead of accumulating in a high concentration at small sizes. Because of the size-dependent growth rate (with small QDs growing faster than large QDs), the QDs focus at the large sizes. When nucleation continues at this relatively slow rate throughout the injection, we refer to it as "continuous nucleation." As the injection progresses, the concentration of intermediates increases, and the rate of nucleation also increases. When the rate of nucleation is fast compared to the rate of growth of existing QDs, then a high concentration of QDs accumulates at small sizes on a shorter timescale than growth to large sizes. Because there is already a population of larger QDs in the reaction mixture, this leads to a bimodal size distribution. We refer to the rapid formation of this secondary population as a "secondary nucleation."

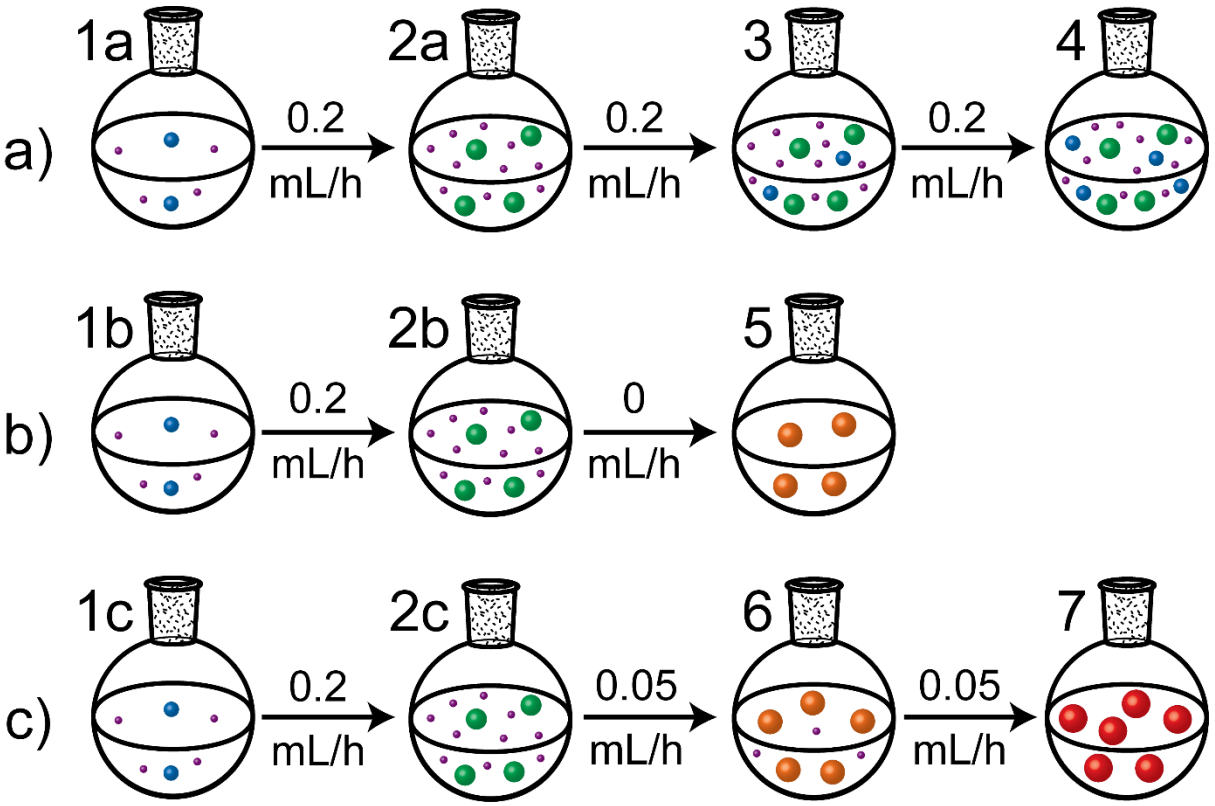

Figure 24. Model of the evolution of the size, size dispersity, and concentration of InP QDs under the conditions of (a) constant-rate, (b) interrupted, and (c) variable-rate seedless continuous injection. The injection rate of the $(TMS)_3P$ solution is indicated for each step. The size of the QDs is represented by the size of the spheres as well as the color in the order blue < green < orange < red. The purple spheres represent intermediates, which are smaller than QDs. The numbers next to the flasks correspond to the numbers of the aliquots indicated in the absorption spectra of Figure 23. Flasks 1 and 2 both experience the same synthetic conditions and exhibit similar results in (a), (b), and (c). In this model, secondary nucleation is caused by a high concentration of intermediates. Interrupting or slowing the injection allows for the intermediates to decrease in concentration as they promote the growth of existing QDs instead of contributing to a secondary nucleation.

We combined our conclusions from Figure 23.a into a model of QD growth. This model is depicted in Figure 24.a, in which intermediates are represented by small purple spheres, and QDs are represented by colored spheres that increase in size in the order blue < green < orange < red. In the early stages of a reaction, intermediates form and contribute to the nucleation and growth of QDs. This is represented between flasks 1a and 2a in Figure 24.a, and it is supported by the redshift of the absorption peak in the first two aliquots of Figure 23.a.i and Figure 23.a.iii. Additionally, the concentration of QDs increases by continuous nucleation (Figure 20.a), but because of the

slowing growth rate of large QDs, the size distribution narrows (indicated by the decrease in VPR shown in Figure 23.a.ii and the decrease in the HWHM shown in Figure 21.a). In later stages of the reaction, the QDs become so large and their growth rate becomes so slow that the absorption peak wavelength remains relatively constant, as seen in the last five aliquots of Figure 23.a.iii. Intermediates are still forming due to the continuous injection of precursors, but because the large QDs consume them at a slower rate, they eventually increase to a critical concentration at which a secondary nucleation leads to a new population of small QDs. This is depicted in flask 3. From Figure 23.a.ii, this threshold concentration of intermediates is reached when the VPR begins to increase after the phosphorus concentration reaches 12.1 mM (0.53 equiv). We hypothesize that, after this point in the reaction, the concentration of intermediates remains high, so QDs continue to nucleate and accumulate at small sizes before they can all catch up to the size of the primary population of more mature QDs (flask 4). There may be conditions that allow them to catch up, but we decided instead to simply prevent the secondary nucleation in the first place, as described in the next section.

3.3.2 Interrupted Seedless Continuous Injection

In our model, there is a relatively large concentration of intermediates in the reaction mixture by the time the phosphorus concentration reaches 12.1 mM (0.53 equiv). If the injection of additional precursors is interrupted at this point, then this should prevent additional intermediates from forming and reaching the critical concentration that gives rise to a secondary population of smaller QDs. Instead, we expect the existing intermediates to decrease in concentration as they promote the growth of existing QDs. This extension of our model is depicted in Figure 24.b between flasks 2b and 5. To test this experimentally, we repeated the synthesis, but

we interrupted the injection when phosphorus reached 12.1 mM (0.53 equiv) and annealed the reaction mixture at the reaction temperature for 1 hour. During the 0.2 mL/h injection stage, the VPR (Figure 23.b.ii) and absorption peak wavelength (Figure 23.b.iii) data show minor variation compared to the data in Figure 23.a, but more importantly, the general trends were reproduced. However, in sharp contrast to the results of Figure 23.a.ii, Figure 23.b.ii shows that the annealing step caused the VPR to continue to decrease, which is consistent with a lack of secondary nucleation. Additionally, the concentration of QDs stayed relatively constant during the annealing step (Figure 20.b), indicating that continuous nucleation had also stopped. As shown in Figure 23.b.i and Figure 23.b.iii, the absorption peak wavelength, which had plateaued before the interruption due to the slowing growth rate of the large QDs, began to redshift again, which is consistent with QD growth. Thus, we conclude that the interruption of the injection prevented further nucleation because the concentration of intermediates remained low. The remaining intermediates in the solution, which were no longer being consumed by nucleation, instead contributed to the growth and size focusing of the existing QDs.

3.3.3 Variable-Rate Seedless Continuous Injection

As shown in the previous section, interrupting the injection of $(TMS)_3P$ and annealing the reaction mixture when phosphorus reached 12.1 mM (0.53 equiv) led to the continued growth of the QDs without a secondary nucleation. However, the extent of continued growth was limited by the concentration of intermediates in the mixture at the time that the injection was interrupted. In order to synthesize even larger QDs, more precursors must be continuously supplied to the reaction mixture, but this must be done at a rate such that intermediate formation is slower than QD growth. This would allow the intermediates to remain in continuous supply to promote the growth of the

QDs, but at a sufficiently low concentration to prevent secondary populations from forming. This extension of our model is depicted in Figure 24.c. To test this, we performed a variable-rate seedless continuous injection. As with the previous two reactions, during the 0.2 mL/h injection stage, the concentration of QDs continuously increased (Figure 20.c), the VPR continuously decreased (Figure 23.c.ii), and the QDs grew in size until reaching a plateau (Figure 23.c.iii). When phosphorus reached 12.1 mM (0.53 equiv), the injection rate was slowed down instead of being held constant or being interrupted altogether. We found that 0.05 mL/h was a sufficiently slow rate to prevent the nucleation of a secondary population, as revealed by the continuously decreasing VPR of the final two aliquots (Figure 23.c.ii). In addition, during the 0.05 mL/h injection stage, the concentration of QDs increased at a slower rate (Figure 20.c), and the peak wavelength increased (Figure 23.c.iii). These results indicate that the slower injection rate leads to a lower concentration of intermediates, which suppresses nucleation. Because fewer intermediates are being consumed by nucleation, they instead contribute to the growth and size focusing of the existing QDs. The final aliquot has an absorption peak at 631 nm and a HWHM of 81 meV. The VPR is 0.75, which is similar to what has previously been achieved at a similar wavelength using a seeded continuous injection.[65] We have not optimized the rate or duration of each injection step, but nevertheless, our results show that a seedless continuous injection can be just as effective as a seeded continuous injection in synthesizing large InP QDs with low size dispersity.

In the model depicted in Figure 24.c, there are no intermediates left in the reaction mixture at the end of the 0.05 mL/h injection step. To provide additional evidence for the complete consumption of intermediates during this step, we repeated the variable-rate injection reaction but added an annealing step of 1 hour after the 0.05 mL/h injection step was complete. We also note that this reaction was performed at 250 °C instead of 300 °C, but the reaction progressed similarly

to the previous variable-rate injection reaction. Specifically, the VPR mostly decreased throughout the reaction (Figure 25.b), and the absorption peak wavelength plateaued before increasing again once the injection rate was slowed down (Figure 25.c). In contrast to the annealing step of the interrupted injection reaction (Figure 23.b), the annealing step in this reaction led to almost no change in the absorption spectra (the red trace and dotted black trace in Figure 25.a), which implies that there were no more intermediates in the reaction mixture to promote QD growth. This implies that the slower injection rate (0.05 mL/h as opposed to 0.2 mL/h) prevented the intermediates from increasing in concentration as they slowly promoted the growth of the existing QDs. This is represented in Figure 25.d, in which flasks 7 and 8 have only large QDs with no intermediates.

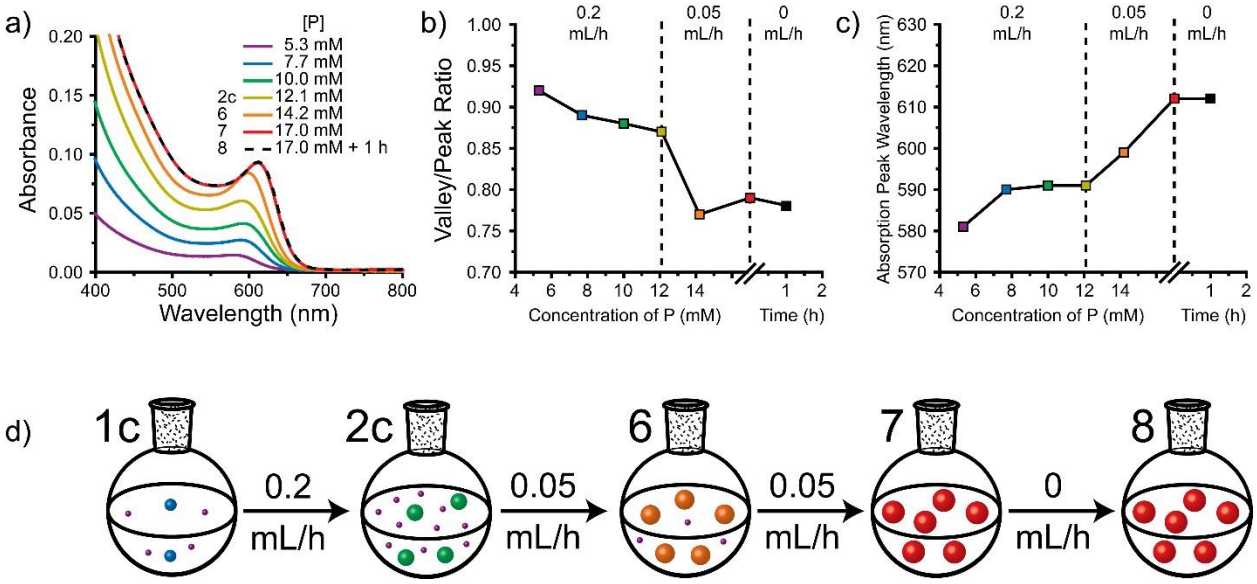

Figure 25. (a) Absorption spectra of aliquots taken throughout InP QD growth under conditions of variable-rate seedless continuous injection at 250 °C. (b) The VPR at different stages of reaction progress. (c) The absorption peak wavelength at different stages of reaction progress. For (b) and (c), the first vertical dotted line indicates when the injection rate was changed from 0.2 mL/h to 0.05 mL/h. The second vertical dotted line indicates when the injection step finished and the annealing step began. To the left of this line, the *x*-axis measures phosphorus concentration, and to the right of this line, the *x*-axis measures time. The minimal effect of the annealing step suggests that the 0.05 mL/h injection step allowed the intermediates to decrease in concentration. Powder X-ray diffraction data, showing a zinc blende crystal structure, and transmission electron microscopy data, showing QDs about 3.7 nm in diameter, for this sample are presented in Figure 26 and Figure 27, respectively. (d) The evolution of the size distribution of QDs during the variable-rate injection reaction at 250 °C. The color scheme is the same as that in Figure 24.

Powder X-ray diffraction reveals that these QDs adopt the zinc blende crystal structure, as shown in Figure 26. The (111), (220), and (311) planes are clearly resolved by XRD. The peak at about 20° is due to amorphous residues.[82] Transmission electron microscopy revealed that the QDs were about 3.7 nm in diameter, consistent with the sizing curve in reference 77 (Figure 27).

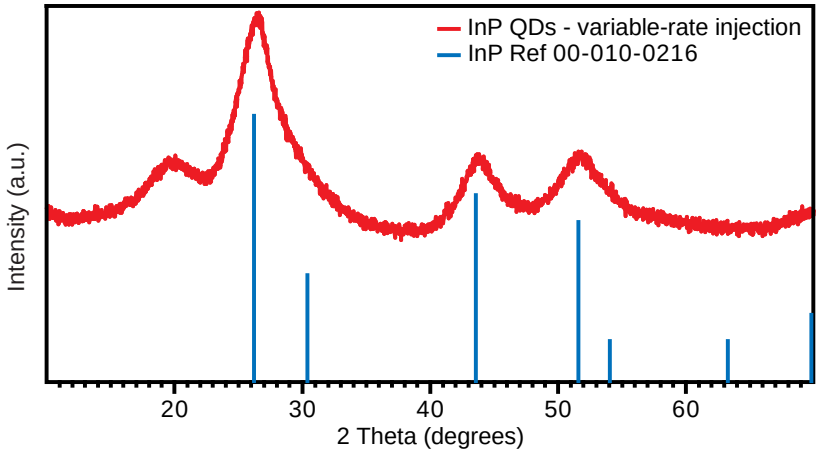

Figure 26. Powder X-ray diffraction pattern of InP QDs synthesized by variable-rate seedless continuous injection with subsequent annealing (red). The peak at about 20° is due to amorphous residues.[82] The reference pattern for bulk zinc blende InP is in blue.

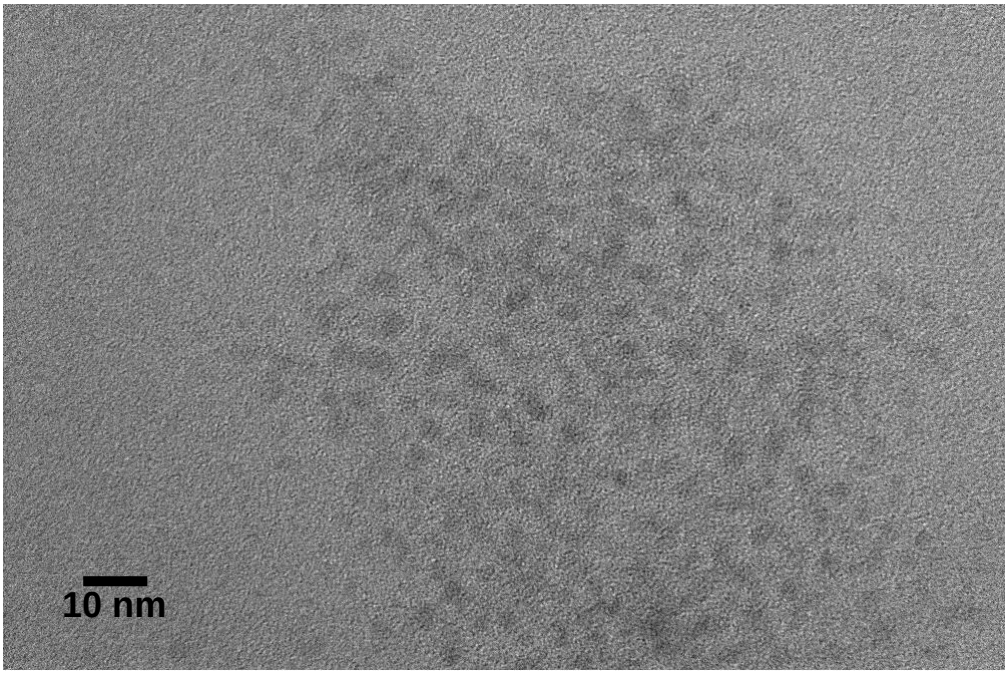

Figure 27. Transmission electron micrograph of InP QDs produced by variable-rate seedless continuous injection with subsequent annealing. The batch in this micrograph has an absorption peak at 612 nm with a HWHM of 87 meV and a VPR of 0.79. The QDs are about 3.7 nm in diameter.

3.3.4 Initial Injection Rate

To determine whether a more rapid increase in the monomer concentration at the beginning of the reaction could improve our results by separating the nucleation event from the growth, we varied the initial injection rate. For the constant-rate injection reaction, the initial injection rate was the same as the injection rate for the rest of the reaction, which was 0.2 mL/h. For the interrupted injection reaction, the initial injection rate was increased to 1 mL/h, and for the variable-rate injection reaction, the initial injection rate was increased to 10 mL/h. In order to prevent broadening from a sustained high injection rate, this initial injection step introduced only 0.05 equivalents of P with respect to In, and the memory of any effect of this injection step was lost by the time of the 5.3 mM (0.21 equiv) aliquot. The characteristic behavior of these reactions occurred after this brief initial injection step. Thus, the rate of the initial injection step had no discernible effect on the rest of the reaction.

3.3.5 Zinc Carboxylates

The addition of zinc carboxylates to hot-injection syntheses of InP QDs can lead to narrower optical spectra and higher QY. We tested the effect of zinc carboxylates on the optical properties of the QDs that are grown by a seedless continuous injection reaction, but we found no significant effect. For the product of the reaction with zinc, the wavelength of the absorption maximum is 618 nm (compared to 633 nm without zinc), the VPR is 0.73 (compared to 0.75), and the HWHM is 77 meV (compared to 81 meV). In addition, the QDs are barely emissive, much like the ones without zinc.

3.3.6 Photoluminescence Properties

In order to characterize the PL wavelength and color purity of the QDs synthesized by our variable-rate seedless continuous injection, we grew a thin ZnSe shell on the QDs of Figure 23.c. The thin ZnSe shell caused only a slight redshift of the absorption peak from 631 to 633 nm, which indicates that the optical properties are representative of the InP core. The resulting PL peak has a maximum at 655 nm with a FWHM of 53 nm or 152 meV (Figure 28). Importantly, these values are similar to the 643 nm peak and 51 nm FWHM that we achieved by using a size-selective precipitation to isolate the population of large QDs in Figure 22. These observations provide evidence that the variable-rate injection method avoids the formation of secondary populations and produces large InP QDs with low size dispersity without the need for a size-selective

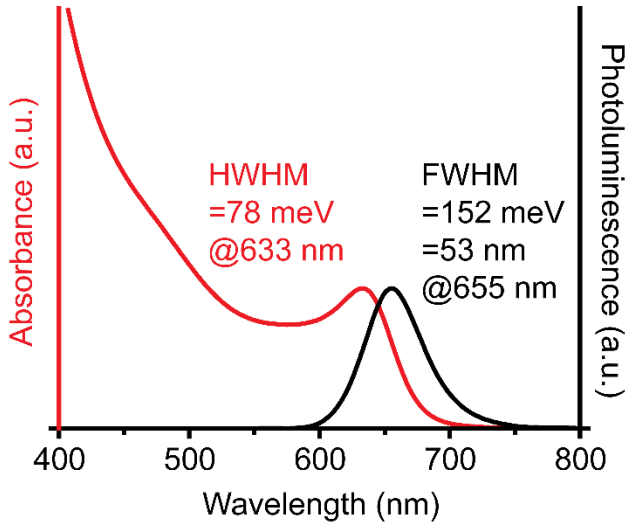

Figure 28. Absorption and PL spectra of InP/ZnSe core/shell QDs labeled with the corresponding peak widths and positions. The long wavelength and narrow FWHM of the PL peak is indicative of large QDs with low size dispersity.
precipitation.

3.3.7 Implications

The results of this work demonstrate that continuous injection can produce large InP QDs of low size dispersity without the need for a separate hot-injection step. This simplifies the synthetic procedure and may avoid the mixing issues associated with large-scale hot injections, making our method attractive for industrial applications.[83] Additionally, the ability of our method to produce InP QDs with narrow PL spectra in the red part of the visible spectrum may make it attractive for further development for applications in solid-state lighting and displays. For example, the PL spectrum of our InP/ZnSe QDs has color coordinates of (0.707, 0.293) on the Commission Internationale de l'Eclairage 1931 color space (Figure 29).[84] This is very close to the color coordinates of the Rec. 2020 standard for the red primary color in displays, which are (0.708, 0.292), corresponding to a monochromatic source at 630 nm. Applying recent surface etching and shell growth methods[66] to the InP QDs produced by our method may also make them highly luminescent, increasing their attractiveness for applications.

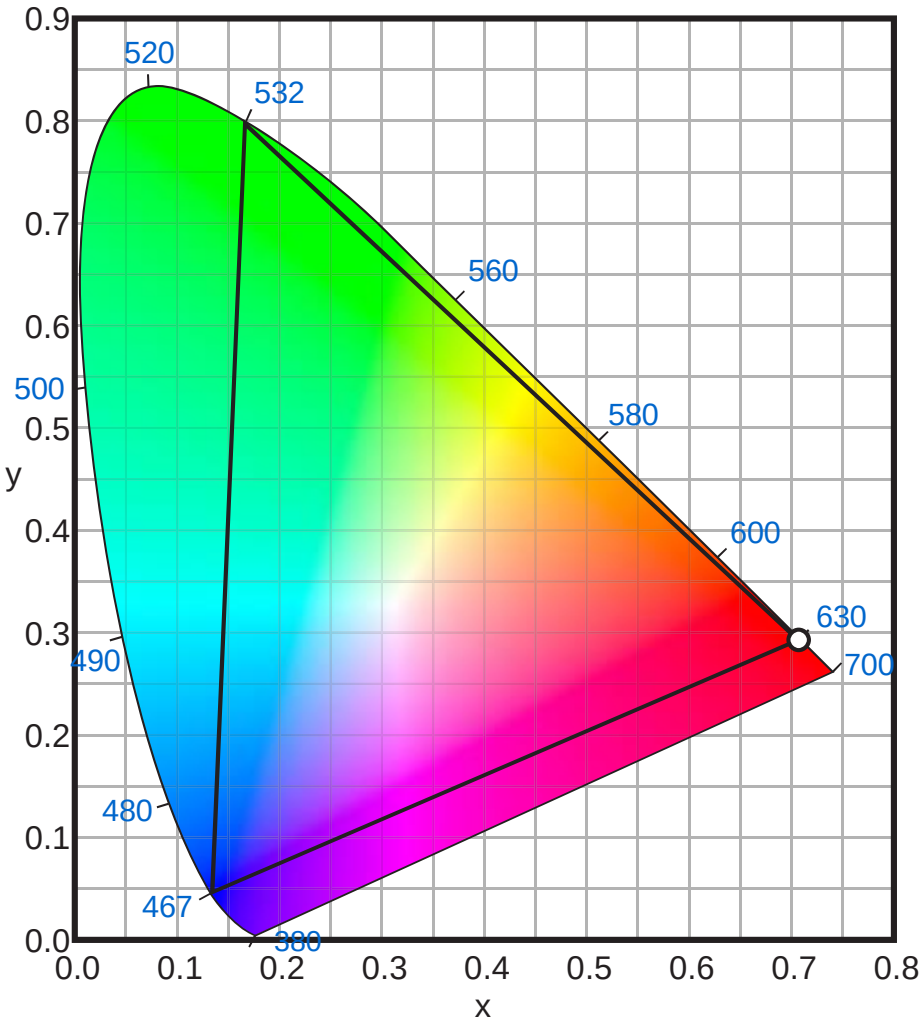

Figure 29. The Commission Internationale de l'Eclairage 1931 chromaticity diagram. The Rec. 2020 color space is enclosed within the black triangle, and the point with coordinates corresponding to the photoluminescence spectrum of our InP/ZnSe QDs in Figure 28 is marked with a white circle. This image was modified from reference 84 under a Creative Commons license.

3.4 Conclusions

We developed several new syntheses for large InP QDs, including an indium-rich seeded continuous injection and a stoichiometric seeded continuous injection. A comparison of the change in concentration of the QDs in these two reactions led us to conclude that the stoichiometric reaction followed a LaMer-type mechanism while the indium-rich reaction followed a continuous nucleation mechanism. We explored the continuous nucleation mechanism further by developing a new seedless continuous injection strategy for the synthesis of InP QDs. The results of our work demonstrate that a rapid nucleation event is not necessary in order to achieve large InP QDs with narrow optical spectra. In fact, a seedless continuous injection leads to the continuous nucleation of InP QDs but also to continuous growth and size focusing. In refining our method, we used previous observations of persistent intermediates to explain the appearance of a secondary population of QDs in the reaction mixture. We then constructed a model of QD growth in which the nucleation rate depends on the concentration of intermediates and the growth rate depends on the size of the QDs. We used this model to design a variable-rate injection method that controls the concentration of intermediates and allows for the continuous growth and size focusing of the QDs without secondary nucleation. The final product consisted of InP QDs with an absorption peak as far red as 631 nm with a narrow HWHM of 81 meV and a VPR of 0.75. The growth of a thin ZnSe shell revealed a PL peak at 655 nm with a FWHM of 53 nm. Our results demonstrate the importance of controlling the injection rate to achieve narrowing optical features throughout the course of the seedless continuous injection synthesis of InP QDs. Further research on the role of the injection rate may lead to greater improvements in size tunability and dispersity.

3.5 Experimental

3.5.1 Preparation of 0.1 M indium oleate

Indium acetate (2 mmol, 0.584 g), oleic acid (6 mmol, 1.9 mL), and ODE (18.1 mL) were loaded into a 25-mL Schlenk flask with a stir bar and rubber septum. The mixture was degassed under vacuum and heated at 100 °C until all of the solid indium acetate had been solubilized. The mixture was cooled to room temperature and stored in a nitrogen-filled glovebox.

3.5.2 Preparation of 0.083 M trioctylphosphine selenide (TOPSe)

To prepare a stock solution of 1 M TOPSe in TOP, selenium powder (5 mmol, 0.395 g) was dissolved in TOP (5 mL) by stirring at room temperature in a nitrogen-filled glovebox. To prepare a 0.083 M solution of TOPSe, 0.2 mL of the 1 M stock solution was diluted in 2.2 mL of ODE.

3.5.3 Synthesis of InP QDs by constant-rate seeded continuous injection

ODE (5.0 mL) and indium myristate (1 mmol, 0.7967 g) were loaded into a 25-mL four-neck round-bottom flask equipped with a stir bar, two rubber septa, a condenser, and a thermocouple. The mixture was degassed for 1 h under vacuum at 110 °C, and then the flask was refilled with an inert atmosphere of nitrogen. The solution was brought to 295 °C, and then a solution of $(TMS)_3P$ (56 μmol, 0.014 g) in trioctylamine (1 mL) was swiftly injected into the reaction mixture. The QDs were left to grow for 20 minutes. Then, solutions of $(TMS)_3P$ (0.38 mmol, 0.096 g) in ODE (4.5 mL) and indium oleate (0.38 mol, 0.36 g) in ODE (2.25 mL) and trioctylamine (2.25 mL) were injected into the reaction mixture by a syringe pump at a rate of 1 mL/h.

3.5.4 Synthesis of InP QDs by variable-rate seeded continuous injection

ODE (5.0 mL) and indium myristate (1 mmol, 0.7967 g) were loaded into a 25-mL four-neck round-bottom flask equipped with a stir bar, two rubber septa, a condenser, and a thermocouple. The mixture was degassed for 1 h under vacuum at 110 °C, and then the flask was refilled with an inert atmosphere of nitrogen. The solution was brought to 295 °C, and then a solution of $(TMS)_3P$ (56 μmol, 0.014 g) in trioctylamine (1 mL) was swiftly injected into the reaction mixture. The QDs were left to grow for 20 minutes. Then, a solution of $(TMS)_3P$ (0.34 mmol, 0.085 g) in ODE (4.0 mL) was injected into the reaction mixture by a syringe pump at a rate of 1 mL/h. After 2.6 mL had been added, the injection rate was changed to 0.3 mL/h. After a total of 3.5 mL had been injected, the injection rate was changed to 0.2 mL/h.

3.5.5 Synthesis of InP QDs by stoichiometric seeded continuous injection

ODE (2.3 mL) and 0.1 M indium oleate in ODE (70 μmol, 0.7 mL) were loaded into a 25-mL four-neck round-bottom flask equipped with a stir bar, two rubber septa, a condenser, and a thermocouple. The mixture was degassed for 1 h under vacuum at 110 °C, and then the flask was refilled with an inert atmosphere of nitrogen. The solution was brought to 300 °C, and then a solution of $(TMS)_3P$ (56 μmol, 0.014 g) in ODE (1 mL) was swiftly injected into the reaction mixture. The QDs were left to grow for 20 minutes. Then, solutions of $(TMS)_3P$ (0.17 mmol, 0.042 g) in ODE (2.0 mL) and 0.1 M indium oleate in ODE (0.20 mmol, 2.0 mL) were injected into the reaction mixture by a syringe pump at a rate of 0.25 mL/h.

3.5.6 Synthesis of InP QDs by constant-rate seedless continuous injection

ODE (2.2 mL), oleic acid (8.0 μmol, 2.5 μL), and 0.1 M indium oleate in ODE (80 μmol, 0.8 mL) were loaded into a 25-mL four-neck round-bottom flask equipped with a stir bar, two rubber septa, a condenser, and a thermocouple. The mixture was degassed for 1 h under vacuum at 110 °C, and then the flask was refilled with an inert atmosphere of nitrogen. The solution was brought to 300 °C, and then a solution of $(TMS)_3P$ (85 μmol, 0.021 g) in ODE (1 mL) was injected into the reaction mixture by a syringe pump at a rate of 0.2 mL/h. A total of 0.75 mL of the $(TMS)_3P$ solution was injected before stopping the injection and cooling down the reaction mixture to room temperature.

3.5.7 Synthesis of In(Zn)P/ZnSe core/shell QDs

Zinc undecylenate (40 μmol, 0.0173 g), ODE (2.2 mL), oleic acid (8.0 μmol, 2.5 μL), and 0.1 M indium oleate in ODE (80 μmol, 0.8 mL) were loaded into a 25-mL four-neck round-bottom flask equipped with a stir bar, two rubber septa, a condenser, and a thermocouple. The mixture was degassed for 1 h under vacuum at 110 °C, and then the flask was refilled with an inert atmosphere of nitrogen. The solution was brought to 300 °C, and then a solution of $(TMS)_3P$ (85 μmol, 0.021 g) in ODE (1 mL) was injected into the reaction mixture by a syringe pump. The injection rate was initially set at 1 mL/h. After 0.05 mL had been injected, the injection rate was changed to 0.2 mL/h. After a total of 0.6 mL had been injected, the injection rate was changed to 0.05 mL/h. After a total of 0.75 mL had been injected, the injection was stopped. Then, a 0.1 M solution of zinc neodecanoate in ODE (100 μmol, 1 mL) and a 0.083 M solution of TOPSe in ODE (83 μmol, 1 mL) were injected at 1 mL/h. When the injection was complete, the mixture was

cooled to room temperature. For size-selective precipitation, ethanol was added to the mixture until it started to become turbid. The mixture was centrifuged at 7000 rpm for 3 minutes.

3.5.8 Synthesis of InP QDs with interrupted injection and subsequent annealing

ODE (2.2 mL), oleic acid (8.0 μmol, 2.5 μL), and 0.1 M indium oleate in ODE (80 μmol, 0.8 mL) were loaded into a 25-mL four-neck round-bottom flask equipped with a stir bar, two rubber septa, a condenser, and a thermocouple. The mixture was degassed for 1 h under vacuum at 110 °C, and then the flask was refilled with an inert atmosphere of nitrogen. The solution was brought to 300 °C, and then a solution of $(TMS)_3P$ (85 μmol, 0.021 g) in ODE (1 mL) was injected into the reaction mixture by a syringe pump. The injection rate was initially set at 1 mL/h. After 0.05 mL had been injected, the injection rate was changed to 0.2 mL/h. After a total of 0.5 mL had been injected, the injection was stopped, and the reaction mixture was annealed at 300 °C for 1 h.

3.5.9 Synthesis of InP QDs by variable-rate seedless continuous injection

ODE (2.2 mL), oleic acid (8.0 μmol, 2.5 μL), and 0.1 M indium oleate in ODE (80 μmol, 0.8 mL) were loaded into a 25-mL four-neck round-bottom flask equipped with a stir bar, two rubber septa, a condenser, and a thermocouple. The mixture was degassed for 1 h under vacuum at 110 °C, and then the flask was refilled with an inert atmosphere of nitrogen. The solution was brought to 300 °C, and then a solution of $(TMS)_3P$ (85 μmol, 0.021 g) in ODE (1 mL) was injected into the reaction mixture by a syringe pump. The injection rate was initially set at 10 mL/h. After 0.05 mL had been injected, the injection rate was changed to 0.2 mL/h. After a total of 0.5 mL had been injected, the injection rate was changed to 0.05 mL/h. After a total of 0.75 mL had been injected, the injection was stopped.

3.5.10 Synthesis of InP/ZnSe core/shell QDs

After the continuous injection synthesis of InP core QDs with a variable-rate injection, the reaction mixture was kept at 300 °C under an inert atmosphere of nitrogen. Next, a 0.1 M solution of zinc neodecanoate in ODE (100 μmol, 1 mL) and a 0.083 M solution of TOPSe in ODE (83 μmol, 1 mL) were injected at 1 mL/h.

3.5.11 Synthesis of InP QDs with variable-rate seedless continuous injection and subsequent annealing

ODE (2.2 mL), oleic acid (8.0 μmol, 2.5 μL), and 0.1 M indium oleate in ODE (80 μmol, 0.8 mL) were loaded into a 25-mL four-neck round-bottom flask equipped with a stir bar, two rubber septa, a condenser, and a thermocouple. The mixture was degassed for 1 h under vacuum at 110 °C, and then the flask was refilled with an inert atmosphere of nitrogen. The solution was brought to 250 °C, and then a solution of $(TMS)_3P$ (85 μmol, 0.021 g) in ODE (1 mL) was injected into the reaction mixture by a syringe pump. The injection rate was initially set at 1 mL/h. After 0.05 mL had been injected, the injection rate was changed to 0.2 mL/h. After a total of 0.5 mL had been injected, the injection rate was changed to 0.05 mL/h. After a total of 0.75 mL had been injected, the injection was stopped, and the reaction mixture was annealed at 250 °C for 1 h. After cooling to room temperature, the reaction mixture was transferred to a nitrogen-filled glovebox. The product was cleaned by three cycles of precipitation with anhydrous ethanol, centrifugation at 3800 rpm for 3 minutes, and redispersion in anhydrous hexanes.

3.5.12 Synthesis of In(Zn)P QDs by variable-rate seedless continuous injection

Zinc undecylenate (38 μmol, 0.0165 g), ODE (2.2 mL), oleic acid (8.0 μmol, 2.5 μL), and 0.1 M indium oleate in ODE (80 μmol, 0.8 mL) were loaded into a 25-mL four-neck round-bottom flask equipped with a stir bar, two rubber septa, a condenser, and a thermocouple. The mixture was degassed for 1 h under vacuum at 110 °C, and then the flask was refilled with an inert atmosphere of nitrogen. The solution was brought to 300 °C, and then a solution of $(TMS)_3P$ (85 μmol, 0.021 g) in ODE (1 mL) was injected into the reaction mixture by a syringe pump. The injection rate was initially set at 1 mL/h. After 0.05 mL had been injected, the injection rate was changed to 0.2 mL/h. After a total of 0.5 mL had been injected, the injection rate was changed to 0.06 mL/h. After a total of 0.74 mL had been injected, the injection was stopped.

Chapter 4: Silver-Doped Indium Phosphide Quantum Dots

4.1 Introduction

Fluorophores for luminescent solar concentrators must have high quantum yield, low reabsorption, and broadband absorption. The thick-shelled cadmium selenide/cadmium sulfide (CdSe/CdS) quantum dots (QDs) in Chapter 2 work well in terms of high quantum yield (QY) and low reabsorption, but they have two main disadvantages. The first of these disadvantages is that they contain cadmium, which is a toxic element that is restricted in commercial products. The second disadvantage is that the amount of light that can be absorbed is limited by the bulk bandgap of the CdS shell, which corresponds in energy to light of ~500 nm. To solve both of these issues, we switched our focus to InP QDs. InP QDs are intrinsically less toxic than CdSe/CdS QDs. In Chapter 3, we described our work to broaden the absorption band of InP QDs by developing a new synthesis to access larger sizes. In the current chapter, we describe our work to increase the QY and decrease the reabsorption of InP QDs.

For thick-shelled QDs, the separation of the absorption and emission spectra comes from the differing bandgaps and the differing volume fractions of the core and shell materials. While emission comes from the core, absorption occurs mostly in the shell because of its larger volume fraction. Because these events occur in different materials with different bandgaps, they occur at different energies. When designing a core/shell QD system for LSCs, the shell most have several properties. First, it must adopt the same crystal structure with a similar lattice parameter as the core. Second, it must have a wider bandgap than the core in order to absorb light that is sufficiently separated from the emission band of the core. Thirdly, in order to outperform CdSe/CdS, the bandgap of the shell must be narrower than that of CdS so that it can absorb more of the solar

spectrum than CdS can. Unfortunately, it is difficult to find the right material to make this kind of shell on InP cores. The most common shell materials for InP QDs are ZnS and ZnSe, but these materials have significant lattice mismatches with InP, making it difficult to grow thick shells while maintaining a high QY. In addition, ZnS and ZnSe have wider bandgaps than CdS does, meaning that they would not be able to harvest as much of the solar spectrum.

Another strategy to separate absorption and emission spectrally is to add a dopant element to a QD core. If the dopant element introduces an electronic state within the host semiconductor's bandgap, a new emissive transition will be possible. Figure 30 demonstrates these processes as they relate to indium phosphide QDs doped with silver, which is what we studied in this project.

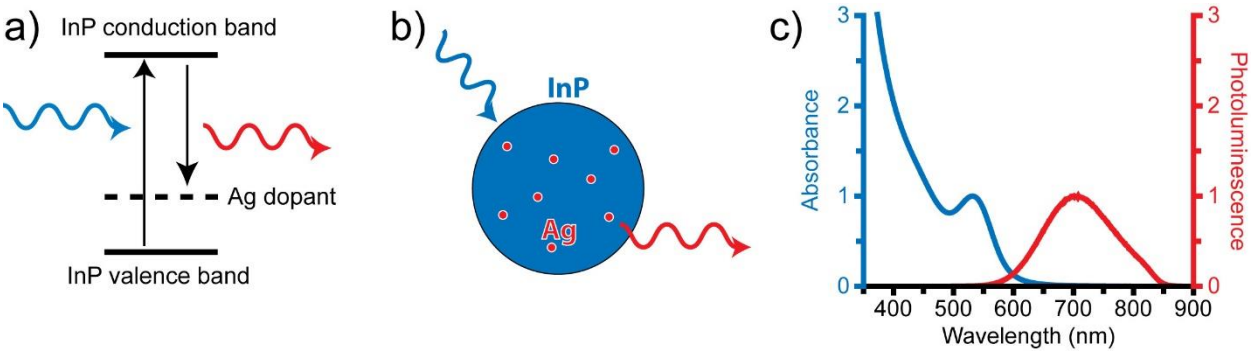

Figure 30. (a) Band diagram demonstrating the energy separation of the absorption and emission events, with the absorption of high-energy light (blue wave) occurring across the InP bandgap (from valence band to conduction band) and emission of low-energy light (red wave) from the InP conduction band to the midgap silver state. (b) Representation of these events occurring in a doped QD. (c) Absorption (blue) and photoluminescence (red) spectra of Ag:InP QDs produced by this work, showing low spectral overlap.

Most previous research on doped InP QDs has been done with copper.[85–87] In the literature, the prevailing explanation of the charge excitation and recombination events involves a localized electronic state on the copper ions whose energy lies within the bandgap of the InP host. Absorption of a photon of appropriate energy promotes an electron from the InP valence band to the InP conduction band, leaving a hole in the valence band. The hole then relaxes to the midgap

copper state, oxidizing the copper ion from Cu^{+} to Cu^{2+}. In the photon emission process, the excited electron relaxes from the InP conduction band to the Cu^{2+}, reducing it back to Cu^{+}.[88]

In CdSe QDs, it has been found that Ag^{+} ions have a similar effect as Cu^{+} ions.[89] This is surprising given the large difference in ionization energy between silver and copper. Recent computational work has shown that in CdSe QDs, copper and silver dopants hybridize with the selenium atoms, and the midgap states are actually antibonding orbitals. For copper, the 3d orbitals lie above the VB that is composed primarily of selenium atoms. After hybridization, the antibonding orbital is predominantly copper in character, and it is pushed deeper into the bandgap than unhybridized copper. For silver, the 4d orbitals lie below the VB maximum. After hybridization of silver with selenium, an antibonding orbital is again pushed into the bandgap, but this time, it is predominantly selenium in character. In either case, a metal-selenium antibonding orbital introduces a midgap state, leading to similar optical properties for copper-doped and silver-doped cadmium selenide QDs.

For the host material, we chose to use indium phosphide QDs because they do not contain any of the toxic elements found in other semiconductors, such as cadmium, lead, and arsenic. In addition, the 1.35 eV bandgap of bulk InP means that it can absorb light up to ~900 nm. This is the bulk bandgap, so quantum-confined QDs will have wider bandgaps, but this gives us a limit to strive toward. In Chapter 3, we described a separate project on increasing the size of InP QDs in order to decrease their bandgap and increase the range of wavelengths that they can absorb. Later in this chapter, we will describe our work on doping large InP QDs, but to start, we worked with more commonly sized InP QDs with bandgaps between 500-600 nm. This already gives them an absorptive advantage over CdSe/CdS QDs, which are limited by the CdS bandgap to absorb light with wavelengths shorter than 500 nm. For the dopant element, we chose silver. Previous research

by other groups has led to copper-doped InP QDs with QYs of 40-60%.[85,87] At the time that we conceived of our project, silver-doped InP QDs were an unpublished material, and we saw them as a potential route to achieving higher QYs. Several papers on silver-doped InP QDs have since been published, but they have been dual-emissive, with emission bands from the InP band edge as well as the silver-related state.[90–92] In this project, we developed silver-doped InP (Ag:InP) QDs with emission almost exclusively from the redshifted silver-related transition in order to maximize the separation between the absorption and emission spectra.

4.2 Silver Doping

We used a cation exchange procedure for the synthesis of Ag:InP QDs. This consisted of a hot-injection synthesis of undoped InP QDs at 300 °C, followed by the addition of a silver precursor to the crude reaction mixture at 210 °C. We used several different silver salts to introduce silver ions into the InP QDs. The first that we tried was silver iodide, but it tended to decompose at high temperature into elemental silver and iodine, leading to a heterogeneous mixture. We then tried silver carboxylates, such as silver acetate and silver oleate. Both silver carboxylates demonstrated an improvement in stability over silver iodide, but they led to a tail in the absorption spectrum at wavelengths longer than the first excitonic transition. This tail may be due to disorder at the surface of the QDs or to the formation of a byproduct. In either case, this absorption tail would lead to reabsorption losses in LSCs. Lastly, we used silver nitrate as the silver precursor, which did not lead to a tail in the absorption spectrum.

Addition of each of the silver precursors to the InP QDs led to the appearance of a similar photoluminescence band that is broader and at longer wavelengths than the band edge emission band of the undoped InP QDs. As described in the next section, the QY of this band could reach

as high as 70%. In addition to introducing a new emission band with a high QY, silver dopants also have the initial effect of increasing the efficiency of the band edge emission at low silver concentrations. This might be due to a similar effect to what is seen when zinc ions are added to an InP QD synthesis. Specifically, it may be that the silver atoms passivate surface electron traps that are caused by undercoordinated surface indium atoms. Because indium requires three ligands for charge balance, there is a steric barrier to full passivation. Silver requires only one negatively charged ligand for charge balance, so there is not a large steric barrier to its complete passivation. If fully coordinated silver atoms replace some of the undercoordinated indium atoms, then this would lead to an increase in QY of the band edge emission. As the concentration of silver increases, the intensity of the band edge emission decreases as the intensity of the dopant-related emission increases. This may be because the increase in concentration of the dopant increases the probability that the hole will be trapped at a dopant before it can recombine radiatively from the VB edge with the electron. Passivation of surface electron traps would also be beneficial for the QY of the dopant-related emission.

4.3 Ligands

While using silver carboxylates as the silver precursor, we noticed that the addition of dodecanethiol (DDT) improved the QY of the QDs (Figure 31.b,c). By the hard-soft acid-base principle, silver is a soft acid, and should bond better with soft thiol ligands than hard carboxylate ligands. Thus, DDT may improve the QY by bonding well with surface-bound silver to passivate their associated trap states (Figure 31a). The addition of DDT also had the effect of diminishing the tail in the absorption spectrum that was induced by the addition of the silver carboxylate. This could indicate that the DDT eased disorder at the surface that was induced by unpassivated silver atoms. Alternatively, it could also mean that the DDT complexed with silver byproducts in the reaction mixture to form a new byproduct that was not absorptive at these wavelengths.

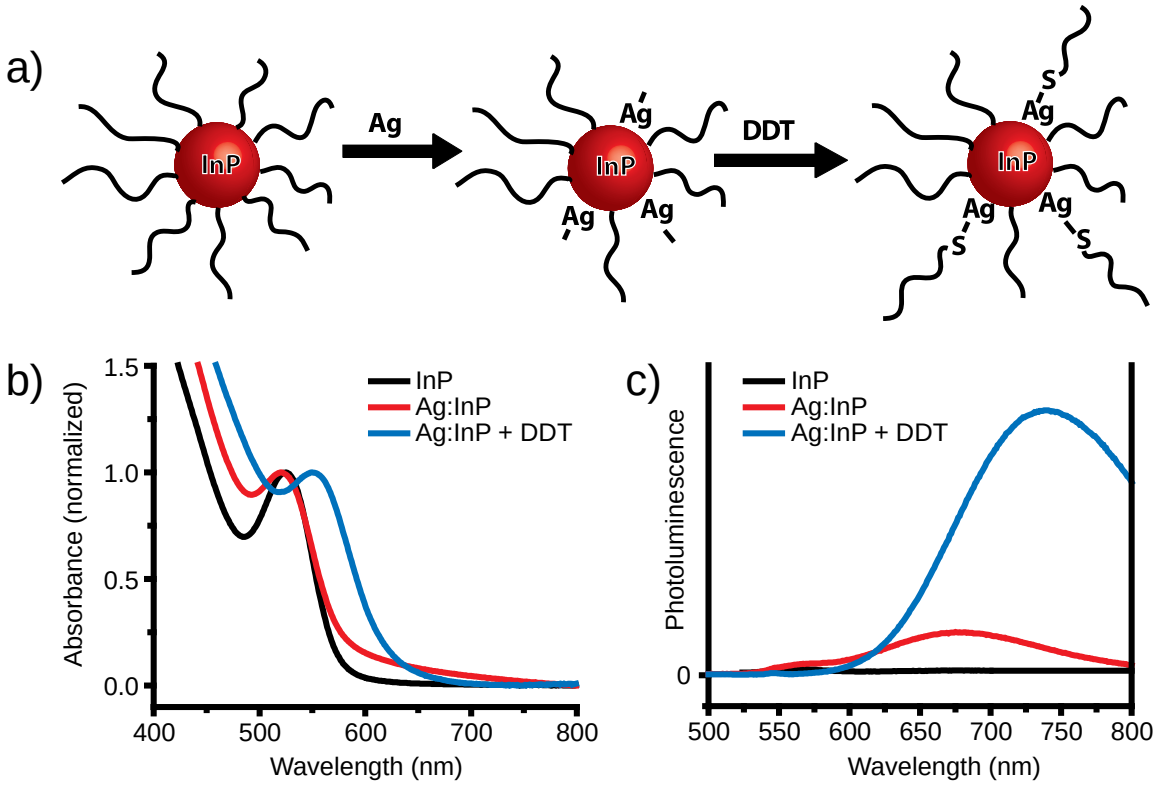

Figure 31. (a) Schematic depiction of the attachment of silver to the surface of InP QDs and passivation with dodecanethiol (DDT). Change in the (b) absorption spectra and (c) photoluminescence intensity after doping InP QDs with silver and passivating them with DDT. Silver introduces a new emission band at lower energy than the band edge. DDT increases the intensity of this emission band.

The same positive effect of dodecanethiol on the QY was observed when using silver nitrate as the silver source. In order to maximize the QY of Ag:InP, we found the optimal concentration of both silver and DDT. To do this, we performed a synthesis in which we first added silver at a 0.09:1 ratio to phosphorus in order to introduce the dopant-related emission. We then started a slow injection of DDT into the reaction mixture. The QY initially decreased before recovering and increasing. When the QY started to level off, we added more silver. The QY appeared to reached a plateau at 70% at a Ag:P ratio of 0.35:1 (Figure 32).

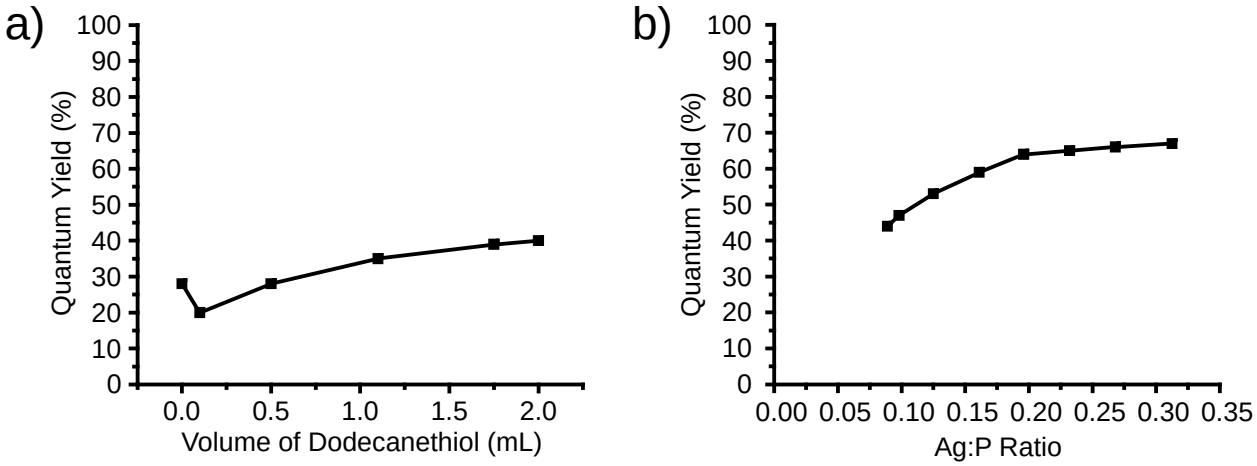

Figure 32. The effect of (a) dodecanethiol and (b) silver content on the quantum yield of silver-doped indium phosphide quantum dots.

4.4 Simulated Performance

We used our Monte Carlo simulation to predict the performance of our Ag:InP QDs and to compare it to the predicted performance of thick-shelled CdSe/CdS QDs. In order to make a meaningful comparison, we had to predict the performance under solar irradiation rather than monochromatic excitation. The only thing that leads to different efficiencies at different excitation wavelengths is the number of photons that can be absorbed. Thus, for each fluorophore, we first ran a simulation to determine the efficiency assuming that 100% of incident photons were absorbed. We then predicted the efficiency at each excitation wavelength by multiplying the maximum efficiency by the absorptance of the fluorophore at that wavelength. We then averaged the efficiency over all wavelengths, weighted by the number of photons in the solar spectrum at each wavelength. As shown in Figure 33, our simulation predicts that the Ag:InP QDs will perform slightly better than the CdSe/CdS QDs. This is despite the fact that our Ag:InP QDs have a QY of only 70% compared to the 80% QY of the CdSe/CdS QDs. The reason why Ag:InP QDs perform

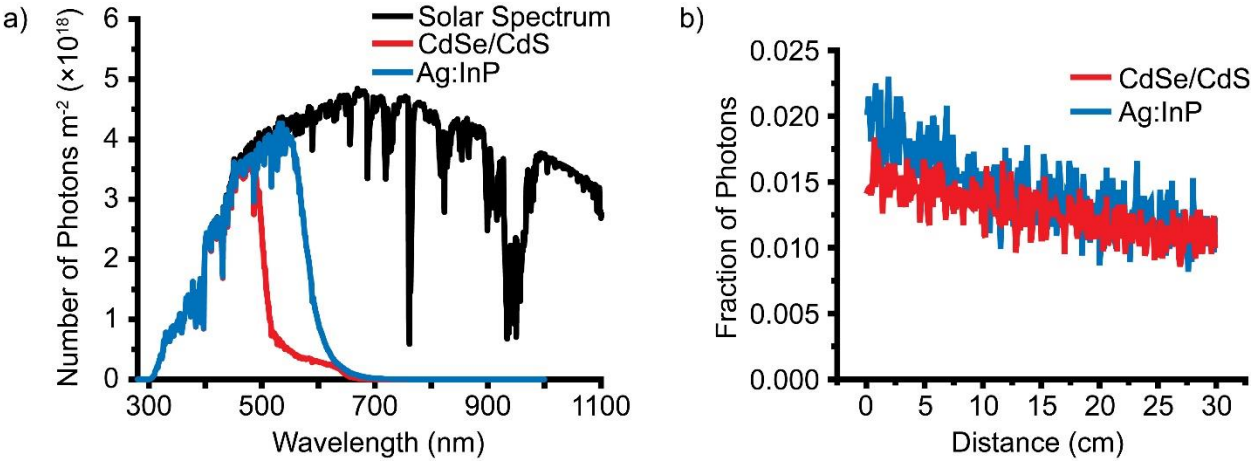

Figure 33. (a) The portion of the solar spectrum (black) that can be absorbed by CdSe/CdS QDs (red) and Ag:InP QDs (blue). (b) Results of Monte Carlo simulations of the efficiency of LSCs with CdSe/CdS (red) and Ag:InP (blue) QD fluorophores. These efficiencies were determined by averaging the efficiency at each excitation wavelength, weighted by the number of photons in the solar spectrum at that wavelength. Even though CdSe/CdS QDs have a higher quantum yield, Ag:InP QDs have a slight advantage in efficiency due to their broader absorption spectrum.

better is that they have a broader absorption spectrum and can absorb more light from the sun. By multiplying the absorptance spectra by the solar spectrum and integrating the results, we determined that our Ag:InP QDs can absorb 1.6 times as many photons from the solar spectrum as CdSe/CdS QDs (Figure 33).

4.5 Large Ag:InP QDs

For thick-shelled CdSe/CdS QDs (described in Chapter 2), the majority of the absorption occurs in the CdS shell, whose bandgap approaches that of bulk CdS. Therefore, there is no option for bandgap tunability to absorb longer wavelengths of light. In contrast, for the Ag:InP system, the absorption occurs in the quantum-confined InP host. Therefore, the breadth of the absorption spectrum of the system can be tuned by changing the size of the InP QDs. Because of the prediction of Figure 33.b that the increased solar absorption of Ag:InP with respect to CdSe/CdS may lead to improved performance, we decided to synthesize larger Ag:InP QDs that can absorb even more light.

In order to collect data on the effect of size on the optical properties of Ag:InP QDs, we designed a seeded continuous injection synthesis in which the seeds are small Ag:InP QDs and the continuous injection solutions contain indium and phosphorus precursors. To avoid potential effects of coordinating solvents on the growth of the nanocrystals, we used a silver precursor that could be dissolved in ODE. Thus, we synthesized silver t-dodecanethiolate. In the synthesis of Ag:InP QDs, InP QD seeds were first synthesized by the normal hot-injection route of injecting TMS_3P into a hot solution of indium oleate. Next, a solution of silver t-dodecanethiolate in ODE was injected into the mixture to dope the InP QDs. As expected, this led to a broad emission band redshifted from the absorption band (Figure 34.b). We then used a syringe pump to slowly inject

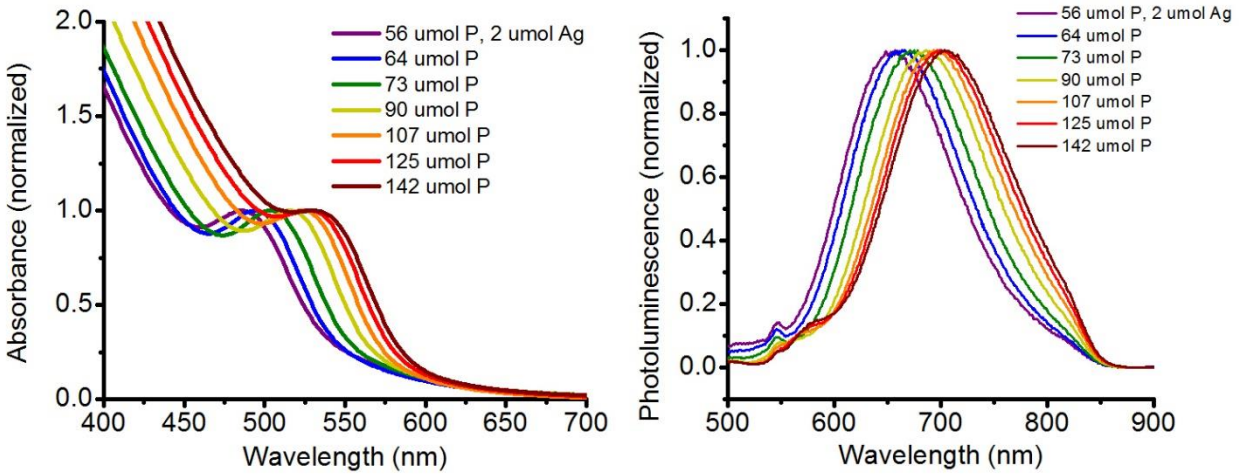

Figure 34. (a) Absorption and (b) PL spectra of aliquots taken during the first seeded continuous injection growth of Ag:InP QDs. The band edge absorption and silver-related PL both redshift with increasing addition of indium and phosphorus precursors. The total amounts of phosphorus and silver at the point of each aliquot are indicated in the legends.

additional indium and phosphorus precursors into the reaction mixture to continue the growth of the doped nanocrystals. The growth of the QDs is supported by the redshift of the absorption spectrum (Figure 34.a). This is accompanied by a redshift of the PL spectrum (Figure 34.b), which indicates that the PL spectrum is also dependent on the confinement of the QDs.

While the continuous injection led to some extended growth of the Ag:InP QDs, we were not able to achieve absorption peak maxima as far red as in the continuous injection growth of undoped InP QDs. Presumably, the silver had some inhibitory effect on the growth. Thus, we conducted two more reactions in which we first grew the InP seeds by continuous injection before doping with silver. After the absorption spectrum of the InP seeds reached a certain wavelength by continuous injection, we injected the silver precursor, and then resumed the continuous injection for even more growth. In the first of these reactions, we let the absorption peak reach 543 nm before adding silver. The growth of these QDs by continuous injection, shown in Figure 35, was inhibited even more than in the growth depicted in Figure 34. In the next reaction, we let the

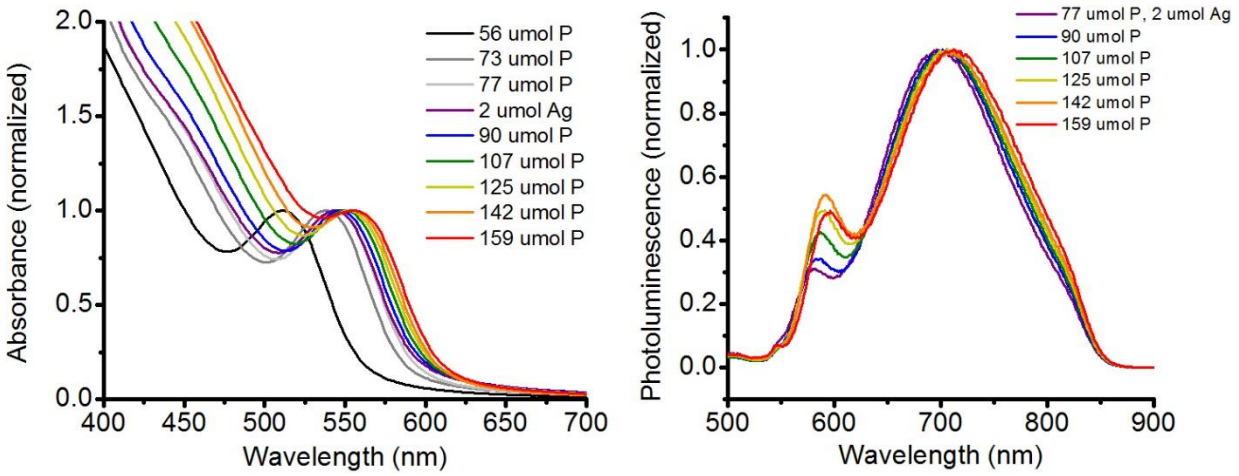

Figure 35. (a) Absorption and (b) PL spectra of aliquots taken during the second seeded continuous injection growth of Ag:InP QDs. Again, the band edge absorption and silver-related PL both redshift with increasing addition of indium and phosphorus precursors. However, further growth becomes more difficult as the QDs get larger.

absorption peak reach 595 nm before adding silver. In this case, continuous injection after the addition of silver did not lead to further growth.

While the broader absorption spectra of the larger QDs will have an unambiguously positive impact on the performance of LSCs, there is another effect of size that complicates the picture. Specifically, the energy separation between the absorption and emission peak depends on the size. We refer to this separation, which is due to two distinct electronic transitions, as the

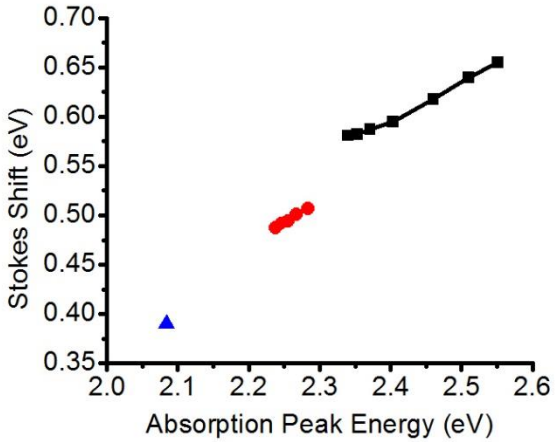

Figure 36. The effective Stokes shift of Ag:InP QDs as a function of the energy of their first absorption peak. As the QD bandgap gets smaller, so does the effective Stokes shift. While the smaller bandgap will act to increase LSC efficiency, the smaller effective Stokes shift will work to decreases LSC efficiency.

effective Stokes shift (as opposed to a true Stokes shift, which would be the separation between absorption and emission for the same transition). We find that as the QDs grow larger and their absorption peak shifts to lower energies, the effective Stokes shift also decreases (Figure 36). While the broader absorption spectrum will lead to greater absorption of solar light, the decreased effective Stokes shift (and increased overlap between the absorption and emission spectra) will lead to greater reabsorption losses. These two effects will have competing influences on the performance of LSCs.

The decreasing effective Stokes shift with decreasing QD bandgap can be understood based on a simple band diagram in which the electronic state associated with the silver dopants is pinned at a constant absolute energy within the bandgap (Figure 37**Error! Reference source not found.**). For the case of Ag:InP, this state is closer to the InP VB than to the CB. As the QD gets larger, the silver-related state stays at roughly the same energy, but the VB maximum increases due to relaxing confinement. This decreases the energy difference between the VB and the silver-related state, which is the origin of the effective Stokes shift.

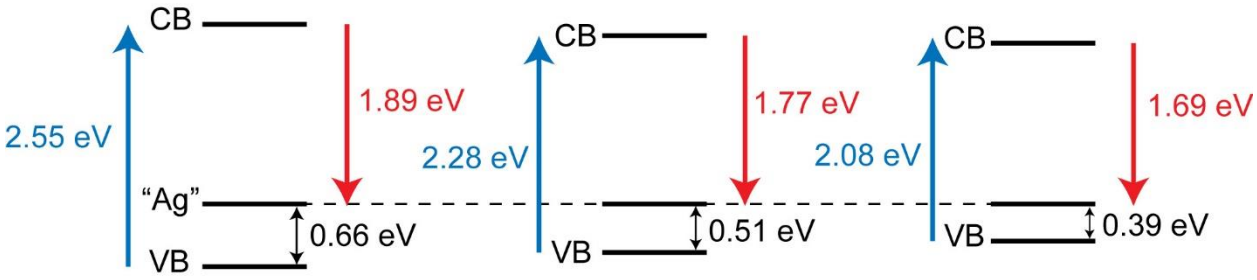

Figure 37. Band diagrams of Ag:InP QDs of increasing size. The energy separation between the valence band (VB) and conduction band (CB) was determined by the energy of the absorption peak. The energy separation between the CB and silver-related state ("Ag") was determined by the energy of the PL peak. As an estimation, the silver-related states are pinned to the same absolute energy. This leads to a reasonable picture because it means that the CB decreases in energy and the VB increases in energy as the QDs get bigger, as is expected for relaxing confinement.

We also synthesized even larger Ag:InP QDs by first synthesizing large InP QDs by a seedless continuous injection. We then added silver post-synthetically in a manner analogous to the synthesis of smaller Ag:InP. For these Ag:InP QDs, no luminescence was observed directly after the addition of silver. However, after adding DDT, a broad near-infrared emission band was observed. In contrast to the trend we observed for Ag:InP QDs synthesized by seeded continuous injection, these exceptionally large Ag:InP QDs have an even greater effective Stokes shift than the small Ag:InP QDs (Figure 38). This cannot be explained by the analysis depicted in Figure 37.

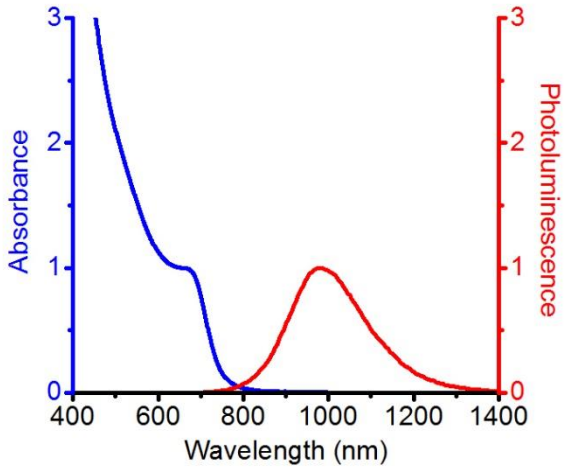

Figure 38. Absorption and photoluminescence spectra of large Ag:InP QDs synthesized by seedless continuous injection of InP QDs and post-synthetic doping with silver. There is very little overlap between the absorption and emission spectra, which would be beneficial for LSC performance. However, the source of the large effective Stokes shift is unknown because it is inconsistent with Figure 36 and Figure 37.

This large effective Stokes shift may be the result of a different crystal environment of the dopants. This may lead to a different hybridization of the silver and phosphorus atoms and a different energy of the midgap state. Alternatively, it may lead to a different level of confinement of the hole to the dopant, causing the dopant state to be pinned to a certain energy above the valence band rather than to a certain absolute energy.

By increasing the size of Ag:InP QDs, we were able to decrease their bandgap and increase the breadth of their absorption spectra, which is beneficial for an LSC fluorophore. However, the

decrease in the bandgap was accompanied by a decrease in the effective Stokes shift. This was the case except for one particular case of exceptionally large Ag:InP QDs synthesized by a seedless continuous injection, which had an exceptionally large effective Stokes shift. A better understanding of this effect could lead to new syntheses of Ag:InP QDs with extremely low reabsorption for LSCs. Another down side to the large Ag:InP QDs is that their QY remains low. A better understanding of the factors that affect the QY must be reached in order to increase the QY so that they may be used in LSCs.

4.6 Shell Growth

For Cu:InP, it has been shown that overcoating the doped cores with a shell can increase the QY due to passivation of surface traps. Thus, we attempted a similar strategy for Ag:InP. For an initial attempted at shell growth, we designed a synthesis for a ZnSe shell. This involved the injection of zinc carboxylates and TOPSe into a solution of the Ag:InP QDs. Because of the relatively low reactivity of the TOPSe precursor, the reaction was done at a high temperature of 300 °C. During the course of the shell growth, the dopant emission disappeared and was replaced by band edge emission. We hypothesize that this was due to the high reaction temperature. This allowed the silver ions to migrate out of the QDs during shell growth. Thus, we tried another shell growth, but this time with ZnS. We used the more reactive bis(trimethylsilyl)sulfide [$(TMS)_2S$] precursor, which allowed us to conduct the reaction at a lower temperature. Under these conditions, the dopant emission was preserved and no band edge emission appeared. However, the shell growth did not have the intended effect of increasing the QY. In fact, the QY decreased throughout shell growth. This may also be the result of the loss of silver ions from the nanocrystals but to a lesser extent than the higher-temperature ZnSe shell growth. More work must be done to monitor

and control the concentration of silver in the QDs during shell growth in order to achieve QDs with higher QYs.

4.7 Recommended Future Work

In this work, we developed a new nanocrystalline system of silver-doped indium phosphide QDs that exhibits high quantum yield and a high effective Stokes shift. However, there is a lot of work on characterizing this material that can be done in order to arrive at a deeper understanding of the physical principles behind its properties. A better understanding of these principles will allow future research to arrive at new syntheses that lead to improvements on these properties.

In order to improve the QY of Ag:InP QDs beyond 70%, it is important to understand what leads to this relatively high QY in the first place. This research direction should take into consideration the effects of both silver and thiols on the QY. One important set of experiments would be to determine the number of silver atoms per QD for samples with different QYs. This could be done by analyzing purified samples of the doped QDs by inductively coupled plasma optical emission spectroscopy (ICP-OES) or X-ray photoelectron spectroscopy (XPS). If there are a small number of silver atoms per QD, it is unlikely that there is enough of them to effectively passivate surface traps to increase the QY. Therefore, we could conclude that the surface passivation explanation is unlikely to be the reason for the high QY. We could also use ICP-OES or XPS to track the number of silver atoms per QD during a shell growth reaction. This could help us determine whether the decrease in QY during shell growth is due to a loss of dopants.

It would also be helpful to analyze the XPS spectra of Ag:InP samples before and after the addition of thiols. Not only could it tell us if thiols have an impact on the number of silver atoms per QD, but it could also give us some information on any redox activity. Silver(I) has a fairly high

reduction potential, and thiols are reducing agents. XPS would reveal if there is any change to the oxidation state of silver as a result of the addition of thiols. A change in the oxidation state could lead to a change in the concentration of electrons or holes or to a change in the charge of the QD, which could affect the QY by filling traps. An analysis of the dopant oxidation state would also be interesting for Cu:InP QDs because copper has slightly richer redox activity than silver. It would be instructive to see if there is also a correlation between QY, thiol concentration, and oxidation state for this separate but related system.

XPS could also have a third role in helping to construct band diagrams. It could reveal the energy levels of the QD band edges and the dopant-related states. We could make this measurement on a size series of Ag:InP QDs to determine if the dopant-related state stays pinned in absolute energy. We could also compare the results of this analysis for Ag:InP QDs prepared by seeded continuous injection (which appear to have the dopant related state pinned in absolute energy) to the results for Ag:InP QDs prepared by seedless continuous injection (which have an unexpectedly large effective Stokes shift).

There are also some optical experiments to be done. Time-resolved photoluminescence (TRPL) could help us to keep track of the radiative and nonradiative decay channels of the excited QDs. One set of experiment would be to measure the photoluminescence lifetimes of the undoped InP QDs, the silver-doped InP QDs, and the silver-doped InP QDs with thiol ligands. The appearance and disappearance of different components to the decay would give us some information about the presence or absence of different radiative and nonradiative decay channels in each of the samples. This would help us determine the factors that affect the QY in each of the samples.

TRPL would also pair well with transient absorption spectroscopy (TA). TA measures the recovery of the bleach of the absorption spectrum of the excited QDs as the charge carriers relax to their ground state. Because of the greater degeneracy of the valence band compared to the conduction band, absorption of a photon can occur more easily if there is a hole in the valence band than if there is an electron in the conduction band. Thus, TA is more sensitive to changes in the electron population of the conduction band than to changes in the hole population of the valence band.[93–96] On the other hand, TRPL is sensitive to both the electron population of the CB and the hole population of the VB. Thus, a comparison of the TRPL decay components and TA recovery components can be used to identify which are caused by electron trapping and which are caused by hole trapping. For example, Hughes et al. found a 7 ns component in both the TRPL and TA of core-only InP QDs. Because this component exists in both the TRPL and TA, they assigned it to hole trapping. They then showed that this 7 ns component became less pronounced as the hole traps were removed by surface treatment of the cores with divalent cations. This was used to explain the increase in quantum yield due to the surface treatment. Similarly, we could use a comparison of TRPL and TA data for undoped InP QDs, silver-doped InP QDs, and silver-doped InP QDs with thiol ligands to assign the changes in quantum yield to different degrees of electron and hole trapping. With that knowledge, we could then seek to improve the quantum yield even more by rationally designing structures that eliminate the remaining traps.

Finally, some additional standard nanocrystal characterization techniques are required. Powder X-ray diffraction would show us if the addition of dopants causes any change to the crystal structure of the QDs, or if the addition of silver to the reaction mixture leads to the formation of any new crystalline phases (silver nanoparticles or silver phosphide, for example). This could be especially helpful for identifying any structural differences that may cause the unexpectedly large

Stokes shift in the largest Ag:InP QDs. Transmission electron microscopy could also give us some insight into structural effects, such as faults in the crystal structure, size and shape effects, and secondary crystalline domains. One final bit of characterization would be photoluminescence excitation spectroscopy. This would help us verify that each of the photoluminescence and absorption features are correlated and therefore that they each originate from the QDs.

4.8 Conclusions

We synthesized silver-doped indium phosphide quantum dots that exhibit minimal reabsorption due to a separation between their absorption and emission spectra. They have a QY of 70%, which is lower than that of CdSe/CdS QDs, but still fairly high. Despite the lower QY, they have a broader absorption spectrum than CdSe/CdS QDs, and as a result, our Monte Carlo simulation predicts that they will perform slightly better than CdSe/CdS QDs in LSCs. We also worked on synthesizing larger Ag:InP QDs in order to absorb a higher percentage of the solar spectrum. We were able to synthesize large Ag:InP QDs, but the QY was low. More characterization is needed to understand the factors that affect the QY so that we can rationally design ways to increase the QY. In addition, most of our experiments show that the effective Stokes shift decreases with decreasing bandgap, but there is one synthesis of large Ag:InP QDs that leads to an unexpectedly large Stokes shift. More characterization is needed to understand this phenomenon so that we can rationally design ways to separate the absorption and emission spectra to minimize reabsorption losses in LSCs.

4.9 Experimental

4.9.1 Small Ag:InP QDs

Indium acetate (0.07 mmol), 1-octadecene (3 mL), and oleic acid (0.21 mmol) were loaded in a 4-neck round bottom flask with a stirbar, condenser, thermocouple, and two rubber septa. The mixture was degassed under vacuum at 110 °C for 1 hour. In a nitrogen-filled glove box, tris(trimethylsilyl)phosphine (TMS3P, 0.056 mmol) was dissolved in 1-octadecene (1 mL). The reaction flask was filled with nitrogen and heated to 300 °C. The solution of TMS3P was injected swiftly into the reaction mixture, which was allowed to react at 300 °C for 20 minutes. Next, the mixture was cooled to 210 °C and a 0.025 M solution of silver nitrate in trioctylphosphine (0.2 mL) was injected by a syringe pump at a rate of 0.15 mL/hr. Then, dodecanethiol (2 mL) was injected by a syringe pump at 1 mL/hr. Finally, additional 0.025 M silver nitrate in trioctylphosphine (0.5 mL) was injected at 0.15 mL/hr.

4.9.2 Ag:InP/ZnSe core/shell QDs

After the synthesis of Ag:InP core QDs, the reaction mixture was kept under an inert atmosphere of nitrogen and the temperature was raised to 300 °C. Next, a 0.1 M solution of zinc neodecanoate in ODE and a 0.083 M solution of TOPSe in ODE were injected at 1 mL/h.

4.9.3 Ag:InP/ZnS core/shell QDs

After the synthesis of Ag:InP core QDs, the reaction mixture was kept at 210 °C under an inert atmosphere of nitrogen. Next, a 0.1 M solution of zinc neodecanoate in ODE and a 0.083 M solution of bis(trimethylsilyl)sulfide in ODE were injected at 1 mL/h.

4.9.4 Large Ag:InP QDs by Seeded Continuous Injection

ODE (2.3 mL), oleic acid (5.0 μL), and 0.1 M indium oleate in ODE (0.7 mL) were loaded in a 4-neck round bottom flask with a stirbar, condenser, thermocouple, and two rubber septa. The mixture was degassed under vacuum at 110 °C for 1 hour. In a nitrogen-filled glove box, tris(trimethylsilyl)phosphine (TMS_3P, 14 mg) was dissolved in 1-octadecene (1 mL). The reaction flask was filled with nitrogen and heated to 300 °C. The solution of TMS_3P was injected swiftly into the reaction mixture, which was allowed to react at 300 °C for 10 minutes. Next, the mixture was cooled to 210 °C and a 0.1 M solution of silver t-dodecanethiolate in ODE (0.02 mL) was injected. With the solution still at 210 °C, the QDs were grown further by injecting a 0.1 M solution of indium oleate in ODE and a 0.085 M solution of TMS_3P in ODE at 1 mL/h. Alternatively, to grow even larger Ag:InP QDs, the injection of 0.1 M indium oleate in ODE and 0.085 M TMS_3P in ODE was started before the solution was cooled to 210 °C and the silver was injected. Once the InP QDs reached the desired size, the precursor injection was paused, the solution was cooled to 210 °C, the silver t-dodecanethiolate was injected, and the indium and phosphorus precursor injection was resumed.

Chapter 5: Conclusion

In this thesis, we described three projects on the development of materials for the improvement of luminescent solar concentrators. In the first project, we invented a new polymer to disperse large thick-shelled CdSe/CdS QDs in a thin film to be deposited on a waveguide. Extending from the backbone of this polymer are long alkyl groups terminated by carboxylic acids. These side chains mimic the native ligands of the QDs, allowing for binding between the polymer and QDs to keep them well dispersed. The similarity of the polymer to the native ligands also allows for high retention of the QD quantum yield. By testing the efficiency of thin-film LSCs prepared with this polymer and CdSe/CdS QDs, we found that concentrated, well-dispersed, low-scattering, high-QY films were achieved. However, the efficiency was limited by the amount of solar light that can be absorbed by the QDs. Thus, we designed a two-layer device based on the complementary absorption properties of the QDs and Lumogen F Red 305. We have yet to prepare and test this device experimentally, but our Monte Carlo simulation predicts that it will perform better than an LSC with a single layer of either CdSe/CdS QDs or Lumogen F Red 305.

In the second project, we sought to develop cadmium-free QDs as a less toxic alternative to replace the CdSe/CdS QDs. For this, we chose indium phosphide QDs. In order to make InP QDs competitive with CdSe QDs for luminescent solar concentrators, we first developed a new method to synthesize large InP QDs in order to access the same long-wavelength optical features that are possible with CdSe. This would allow them to absorb a fraction of the solar spectrum that is competitive with CdSe. We found that slowly adding indium and phosphorus precursors to InP seeds from a hot injection was an effective way to extend their growth to larger sizes. We also found that this continuous injection strategy was effective for producing large InP QDs even in the absence of seeds from a hot injection. Control of the injection rate was critical to balance the

nucleation of new QDs with the growth of existing ones. Our optimized synthesis led to QDs with absorption features with wavelengths as long as 631 nm, which is good for solar light absorption. By controlling the growth rate, we also achieved narrow size distributions and a photoluminescence band as narrow as 53 nm at a position of 655 nm. This makes these QDs also attractive for applications in displays.

In the third project, we sought to induce a separation between the absorption and emission spectra of the InP QDs in order to reduce the probability of reabsorption events when they are used in LSCs. We did this by adding silver atoms to the InP QDs to introduce an electronic state in the middle of the bandgap. This provides a low-energy emission transition between the conduction band and the midgap state, while the absorption transition remains at higher energy between the valence band and conduction band. We first synthesized small silver-doped InP QDs by adding silver to InP QDs that were synthesized by a traditional hot injection. By optimizing the amount of silver and by adding dodecanethiol as a ligand, we achieved a quantum yield of 70% for this separated emission band. So far, shell growth has been unsuccessful at increasing the quantum yield further. Despite the fact that the QY is lower than that of CdSe/CdS QDs, our Monte Carlo simulation predicts that these Ag:InP QDs will perform better than CdSe/CdS QDs in LSCs due to their broader absorption band. We then synthesized larger Ag:InP QDs by adding silver to InP QDs that were synthesized by seeded continuous injection. We grew them even larger by continuing the continuous injection of indium and phosphorus precursors after silver was added. For these QDs, we found a decreasing effective Stokes shift with decreasing bandgap, which would decrease their efficiency in LSCs due to reabsorption. However, for even larger Ag:InP QDs, synthesized by adding silver to InP QDs synthesized by seedless continuous injection, we observed a greater effective Stokes shift, but a low quantum yield. More characterization must be done to

understand what influences the quantum yield and effective Stokes shift so that these properties can be optimized for use in LSCs.

Appendix

Monte Carlo Simulation Code

All of the computer code for the Monte Carlo simulation was written by Timothy S. Sinclair.

Concentrator Class

```
classdef concentrator

    properties
        source_spectrum = []; % intensities of source light
        source_lambdas = []; % wavelengths of source light
        lat_dimensions = [0 0]; % x-y dimensions of concentrator in mm
        layers = cell(0); % list of layers of the aggregate
        thicknesses = []; % list of thicknesses of each layer in mm
        QY = []; % list of QY of each layer that contains absorbing media
        ns = []; % refractive indices of each layer
        mfp_lambdas = cell(0);
        mfps = cell(0);
        scatter_mfps = cell(0); % mean free path before scattering
        scatter_lambdas = cell(0); % wavelengths of scattering mean free path
        emission_lambdas = cell(0);
        emissions = cell(0);
        polar = 1;
        debug = 0;
        full_collect = 1;
        n_clad = 1.00029;
        ph_pos = [0 0 0]; % position of the photon during propogation
        ph_dir = [0 0 0]; % direction of the photon during propogation
        ph_absorption = 0;
        ph_bottom = 0; % number of photons that escape out of the bottom
        ph_absorbed = 0; % number of photons that are absorbed and never
reemit
        ph_top = 0; % number of photons that escape out of the top (includes
reflections)
        wave = 0;
        ph_wall = [0 0 0 0]';
        ph_collect = 0;
        abs_ctr = zeros(4,26);
        sst = '-x+x-y+yz0';
        collisions = [0 0 0 0 0];
    end % concentrator properties
    methods (Static)
        function direction = randomDirection()
            theta = 2*pi*rand();
            phi = acos(2*rand()-1);
            x = sin(phi)*cos(theta);
            y = sin(phi)*sin(theta);
            z = cos(phi);
            direction = [x y z];
        end % randomDirection function
    end
```

```
    methods
        function obj = concentrator(lat_dimensions, polar, Solar, collisions)
            % Construct a new concentrator object. dimensions should be a
            % 1x2 array of the x and y dimensins of the concentrator.
            obj.lat_dimensions = lat_dimensions;
            obj.polar = polar;
            if size(Solar) == 1
                obj.source_lambdas = Solar;
                obj.source_spectrum = 1;
            else
                if Solar(2,1) < Solar(1,1)
                    Solar = flipud(Solar);
                end
                obj.source_lambdas = Solar(:,1);
                scaled_source = (Solar(:,2) -
min(Solar(:,2))*ones(size(Solar(:,2))));
                scaled_source = scaled_source/((Solar(2,1)-
Solar(1,1))*trapz(scaled_source,1));
                cumu_scaled_source = cumsum(scaled_source);
                obj.source_spectrum = cumu_scaled_source; % wavelength of the
laser illumination
            end
            if nargin > 3
                obj.collisions = collisions;
            end
        end % concentrator constructor function

        function obj = addLayer(obj, name, thickness, QY, n, T, emission,
collisions)
            % Adds a new layer on top of the previous layer. thickness is
            % the z-height, n is the index of refraction, T is the
            % transmittance spectrum, and emission is the emission spectrum
            num_layers = numel(obj.thicknesses);
            obj.sst = [obj.sst,'z',num2str(num_layers)+1];
            obj.layers{1,end+1} = name;
            obj.thicknesses = [obj.thicknesses thickness];
            obj.QY(1,end+1) = QY;
            obj.ns = [obj.ns n];
            obj.collisions = [obj.collisions collisions];
            if T(2,1) < T(1,1)
                T = flipud(T);
            end
            obj.mfp_lambdas{1,end+1} = T(:,1);
            scaled_T = (T(:,2)).*ones(size(T(:,2)))/100;
            obj.mfps{1,end+1} = thickness./-log(scaled_T);

            if emission(2,1) < emission(1,1)
                emission = flipud(emission);
            end
            obj.emission_lambdas{1,end+1} = emission(:,1);
            scaled_emission = emission(:,2) -
min(emission(:,2))*ones(size(emission(:,2)));
            scaled_emission = scaled_emission/((emission(2,1)-
emission(1,1))*trapz(scaled_emission,1));
            cumu_scaled_emission = cumsum(scaled_emission);
            obj.emissions{1,end+1} = cumu_scaled_emission;
```

```
        end % addLayer function
        function ind = getLayer(obj, coords)
           % gives the index of the layer in which the coords are located,
           % or if "coords" is a string, then gives the index of the layer
           % with that name
           if ischar(coords)
               ind = find(strcmp(obj.layers, coords));
           end
           if ~ischar(coords)
               depths = cumsum([0 obj.thicknesses]);
               ind = sum(coords(3) > depths);
           end
        end % getLayer function

        function n = getn(obj,coords)
            % gives the index of refraction (n) for the coordinates given
            layer = obj.getLayer(coords);
            if (layer == 0) || (layer > size(obj.ns,2)) || (abs(coords(1)) >
obj.lat_dimensions(1)/2) || (abs(coords(2)) > obj.lat_dimensions(2)/2)
                n = 1.00029;
            else
                n = obj.ns(layer);
            end % if
        end % function getn

        function length = meanFreePath(obj, layer, wavelength)
%             if layer == 1;
%                 if wavelength == 400
%                     length = obj.mfps{1};
%                     length = length(1);
%                 end
%                 if wavelength == 600
%                     length = Inf;
%                 end
%
%             else
%                     length = Inf;
%             end
            if (layer > 0) && (layer < size(obj.layers,2)+1)
                mfp_spectrum = obj.mfps{layer};
                mfp_wavelengths = obj.mfp_lambdas{layer};
                if wavelength < min(mfp_wavelengths)
                    length = mfp_spectrum(1);
                elseif wavelength > max(mfp_wavelengths)
                    length = mfp_spectrum(end);
                else
                    %wavelength
                    prev_ind = find(wavelength > mfp_wavelengths,1,'last');
                    next_ind = find(wavelength < mfp_wavelengths,1,'first');
                    interp = (wavelength -
mfp_wavelengths(prev_ind))/(mfp_wavelengths(next_ind) -
mfp_wavelengths(prev_ind));
                    length = mfp_spectrum(prev_ind) +
interp*(mfp_spectrum(next_ind) - mfp_spectrum(prev_ind));
                end
```

```
            else %
                length = Inf;
            end
        end % function meanFreePath

        function wavelength = randomSolarWavelength(obj)
            if size(obj.source_lambdas) == 1
                wavelength = obj.source_lambdas;
            else
                cumu_spectrum = obj.source_spectrum;
                cumu_wavelengths = obj.source_lambdas;
                val = rand();
                if val < cumu_spectrum(1)
                    wavelength = cumu_wavelengths(1);
                else
                    prev_ind = find(val > cumu_spectrum,1,'last');
                    next_ind = find(val < cumu_spectrum,1,'first');
                    interp = (val -
cumu_spectrum(prev_ind))/(cumu_spectrum(next_ind) - cumu_spectrum(prev_ind));
                    wavelength = cumu_wavelengths(prev_ind) +
interp*(cumu_wavelengths(next_ind) - cumu_wavelengths(prev_ind));
                end
            end
        end % randomSolarWavelength function

        function wavelength = randomWavelength(obj, layer)
            cumu_spectrum = obj.emissions{layer};
            cumu_wavelengths = obj.emission_lambdas{layer};
            val = rand();
            %first_ind = obj.emission_lambdas{layer}(1);
            if val < cumu_spectrum(1)
                wavelength = cumu_wavelengths(1);
            else
                prev_ind = find(val > cumu_spectrum,1,'last');
                next_ind = find(val < cumu_spectrum,1,'first');
                interp = (val -
cumu_spectrum(prev_ind))/(cumu_spectrum(next_ind) - cumu_spectrum(prev_ind));
                wavelength = cumu_wavelengths(prev_ind) +
interp*(cumu_wavelengths(next_ind) - cumu_wavelengths(prev_ind));
            end
        end % randomWavelength function

        function truth = isNotReemitted(obj, layer)
            if rand() > obj.QY(layer) % the higher the QY, the higher
                truth = 1;            % the chance of being reemitted
            else % if
                truth = 0;
            end % if
        end % function isNotReemitted

        function obj = propogatePhoton(obj, targets, pos, ncoll)
            obj.ph_pos = [pos -10^-10];
            direc = [0 0 1];
            ph_propogating = 1;
            abs_count = 0;
            obj.wave = obj.randomSolarWavelength();
```

```
            s_polar = 0.5;
            while ph_propogating
                current_layer = obj.getLayer(obj.ph_pos);
                mfp = obj.meanFreePath(current_layer, obj.wave);
                dist_travel = exprnd(mfp);
                reflecting = 1;

                gmd =
(obj.lat_dimensions(1)*obj.lat_dimensions(2)*sum(obj.thicknesses))^(1/3);
                if not(current_layer==0)
                TIR = asind(1/1.49);%obj.getn(current_layer));
                states_check = 1:max(size(obj.ns));
                states_check(current_layer) = [];
                truths = zeros(size(states_check));
                for ind = 1:(max(size(obj.ns))-1)
                    state = states_check(ind);
                    truths(ind) = (obj.meanFreePath(state,obj.wave) >
100*gmd);
                end
                while prod(TIR<acosd(abs(direc)))&&(dist_travel >
100*gmd)&&prod(truths)
                    'TIR\n'
                    direc = obj.randomDirection();
                    nlayers = max(size(obj.ns));
                    mfp_list = zeros(1,nlayers);
                    for i = 1:nlayers
                        mfp_list(i) = obj.meanFreePath(i,obj.wave);
                    end
                    layer_out =
randscr(1,[1:nlayers;1./mfp_list/sum(1./mfp_list)]);
                    obj.ph_pos = [obj.lat_dimensions.*(2*rand(1,2)-1)
sum(obj.thicknesses(1:(layer_out-1)))+obj.thicknesses(layer_out)*rand()];
                    current_layer = obj.getLayer(obj.ph_pos);
                    obj.wave = obj.randomWavelength(current_layer);
                    mfp = obj.meanFreePath(current_layer, obj.wave);
                    dist_travel = exprnd(mfp);
                    for ind = 1:(max(size(obj.ns))-1)
                        state = states_check(ind);
                        truths(ind) = (obj.meanFreePath(state,obj.wave) >
100*gmd);
                    end
                    if not(prod(TIR<acosd(abs(direc)))&&(dist_travel >
100*gmd)&&prod(truths))
                        break
                    end
                end
                end
                while reflecting
                    if obj.debug == 1
                        pos = obj.ph_pos;
                        fprintf(['\tposition ',num2str(pos(1)),'
',num2str(pos(2)),' ',num2str(pos(3)),'\n'])
                        fprintf(['\tdirection ',num2str(direc(1)),'
',num2str(direc(2)),' ',num2str(direc(3)),'\n'])
                        fprintf(['\twill travel up to ',num2str(dist_travel),'
before absorption\n'])
```

```
                    end % debug
                    % calculates which wall will be hit first, and what point
will
                    % be hit
                    % Walls listed are +/- x walls, +/- y walls, then z walls
in
                    lat_dims = obj.lat_dimensions;
                    pos = obj.ph_pos;
                    walls = [lat_dims(1)/2 -lat_dims(1)/2 lat_dims(2)/2 -
lat_dims(2)/2 0 cumsum(obj.thicknesses)];
                    zvel = direc(3);
                    vels = [direc(1) direc(1) direc(2) direc(2)
repmat(zvel,1,numel(obj.thicknesses)+1)];
                    zpos = pos(3);
                    locs = [pos(1) pos(1) pos(2) pos(2)
repmat(zpos,1,numel(obj.thicknesses)+1)];
                    times = (walls - locs)./vels;
                    time = unique(min(times(times >= 0))); % the photon will
first encounter the closest wall in a positive direction

                    if isequal(size(time),[1 0]) % if no walls are in a
positive direction, which wall did the photon last hit?
                        time = max(times);
                    end

                    collision_point = obj.ph_pos + direc*time; % where did the
photon hit?
                    nearest_wall = unique(find(time == times)); % which wall
is this?

                    if time < 0  % if the photon will never hit a wall again,
put it in the correct bin
                        if ismember(nearest_wall,targets)
                            obj.abs_ctr(abs_count+1) =
obj.abs_ctr(abs_count+1) + 1;
                            obj.ph_collect = obj.ph_collect + 1;
                        end
                        if nearest_wall < 5
                            obj.ph_wall(nearest_wall) =
obj.ph_wall(nearest_wall) + 1;
                        end
                        if nearest_wall == 5
                            obj.ph_top = obj.ph_top + 1;
                        else
                            obj.ph_bottom = obj.ph_bottom + 1;
                        end
                        return
                    end
                    if obj.debug == 1
                        %sst = '-x+x-y+y-z+z';
                        fprintf(['\twall ',obj.sst(2*nearest_wall-
1:2*nearest_wall),'\n'])
                        fprintf(['\tnext wall in
',num2str(pdist(vertcat(obj.ph_pos,collision_point))),' mm\n'])
                    end
```

```
                    dist_travel = dist_travel -
pdist(vertcat(obj.ph_pos,collision_point));
                    if dist_travel < 0
                        abs_count = abs_count + 1;
                        obj.ph_pos = collision_point + dist_travel * direc;
                        obj.ph_absorption = obj.ph_absorption + 1;
                        if obj.debug == 1
                            fprintf('\tabsorbed\n')
                            %fprintf(['\tabsorbed in
',num2str(pdist(vertcat(pos,collision_point))),'\n'])
                        end % if
                        if obj.isNotReemitted(obj.getLayer(obj.ph_pos))
                            obj.ph_absorbed = obj.ph_absorbed + 1; % Photon
absorbed and not re-emitted
                            if obj.debug == 1
                                fprintf('\tnot re-emitted\n')
                            end % debug
                            return
                        end % is not reemitted
                        if obj.debug == 1
                            fprintf('\tre-emitted with new direction and
wavelength\n')
                        end % debug
                        obj.wave = obj.randomWavelength(current_layer);
                        direc = obj.randomDirection();
                        break
                        %reflecting = 0;
                    end % if absorbed

                    n1 = obj.getn(obj.ph_pos);
                    if ismember(nearest_wall, [1 2])
                    %handle R/T
                        n2 = 1.00029;
                        th_i = acos(abs(direc(1)));
                        th_t = asin((n1/n2)*sqrt(direc(2)^2 + direc(3)^2));
                        Rp = abs((n1*cos(th_i) - n2*cos(th_t))/(n1*cos(th_i) +
n2*cos(th_t)))^2;
                        Rs = abs((n1*cos(th_t) - n2*cos(th_i))/(n1*cos(th_t) +
n2*cos(th_i)))^2;
                        R = s_polar*Rs + (1 - s_polar)*Rp;

                        collision = obj.collisions(nearest_wall);
                        if ((rand() < R)&&(collision == 0))||(collision == -1)
                        % reflect
                            if obj.debug == 1
                                fprintf('\treflected in x\n')
                            end
                            if obj.polar == 0
                                s_polar = 0.5;
                            end
                            s_polar = s_polar*Rs / (s_polar*Rs + (1-
s_polar)*Rp);
                            direc(1) = -1*direc(1);
                            obj.ph_pos = collision_point + 10^-
10*sign(direc(1));
```

```
                        else
                        % transmit
                            obj.ph_wall(nearest_wall) =
obj.ph_wall(nearest_wall)+1;
                            target = 1 + (-sign(direc(1))+1)/2;
                            if ismember(target,targets)
                                n1 = 1.00029;
                                n2 = ncoll;
                                th_i = acos(abs(direc(1)));
                                th_t = asin((n1/n2)*sqrt(direc(2)^2 +
direc(3)^2));
                                Rp = abs((n1*cos(th_i) -
n2*cos(th_t))/(n1*cos(th_i) + n2*cos(th_t)))^2;
                                Rs = abs((n1*cos(th_t) -
n2*cos(th_i))/(n1*cos(th_t) + n2*cos(th_i)))^2;
                                R = s_polar*Rs + (1 - s_polar)*Rp;
                                obj.abs_ctr(abs_count+1) =
obj.abs_ctr(abs_count+1) + 1;
                                obj.ph_collect = obj.ph_collect + (1-R);
                            end
                            return
                        end % end if reflects
                    end % nearest_wall == 1

                    if ismember(nearest_wall, [3 4])
                        %handle R/T
                        n2 = 1.00029;
                        th_i = acos(abs(direc(2)));
                        th_t = asin((n1/n2)*sqrt(direc(1)^2 + direc(3)^2));
                        Rp = abs((n1*cos(th_i) - n2*cos(th_t))/(n1*cos(th_i) +
n2*cos(th_t)))^2;
                        Rs = abs((n1*cos(th_t) - n2*cos(th_i))/(n1*cos(th_t) +
n2*cos(th_i)))^2;
                        R = s_polar*Rs + (1 - s_polar)*Rp;

                        collision = obj.collisions(nearest_wall);
                        if ((rand() < R)&&(collision == 0))||(collision == -1)
                            % reflect
                            if obj.debug == 1
                                fprintf('\treflected in y\n')
                            end
                            if obj.polar == 0
                                s_polar = 0.5;
                            end
                            s_polar = s_polar*Rs / (s_polar*Rs + (1-
s_polar)*Rp);
                            direc(2) = -1*direc(2);
                            obj.ph_pos = collision_point + 10^-
10*sign(direc(2));

                        else % transmit
                            obj.ph_wall(nearest_wall) =
obj.ph_wall(nearest_wall) + 1;
                            target = 3 + (-sign(direc(2))+1)/2;
                            if ismember(target,targets)
                                n1 = 1.00029;
```

```
                                n2 = ncoll;
                                th_i = acos(abs(direc(2)));
                                th_t = asin((n1/n2)*sqrt(direc(1)^2 +
direc(3)^2));
                                Rp = abs((n1*cos(th_i) -
n2*cos(th_t))/(n1*cos(th_i) + n2*cos(th_t)))^2;
                                Rs = abs((n1*cos(th_t) -
n2*cos(th_i))/(n1*cos(th_t) + n2*cos(th_i)))^2;
                                R = s_polar*Rs + (1 - s_polar)*Rp;
                                obj.abs_ctr(abs_count+1) =
obj.abs_ctr(abs_count+1) + 1;
                                obj.ph_collect = obj.ph_collect + (1-R);
                            end
                            return
                        end % end if reflects
                    end

                    if nearest_wall > 4
                        current_layer = sum(obj.ph_pos(3) > [0
cumsum(obj.thicknesses)]);
                        layer_id = current_layer + sign(direc(3));
                        layernums = 1:numel(obj.ns);
                        if sum(layernums == current_layer)
                            n1 = obj.ns(current_layer);
                        else
                            n1 = obj.n_clad;
                        end
                        if sum(layernums == layer_id)
                            n2 = obj.ns(layer_id);
                        else
                            n2 = obj.n_clad;
                        end
                        th_i = acos(abs(direc(3)));
                        th_t = asin((n1/n2)*sqrt(direc(1)^2 + direc(2)^2));
                        Rs = abs((n1*cos(th_i) - n2*cos(th_t))/(n1*cos(th_i) +
n2*cos(th_t)))^2;
                        Rp = abs((n1*cos(th_t) - n2*cos(th_i))/(n1*cos(th_t) +
n2*cos(th_i)))^2;

                        if obj.polar == 0
                            s_polar = 0.5;
                        end
                        R = s_polar*Rs + (1 - s_polar)*Rp;

                        collision = obj.collisions(nearest_wall);
                        if ((rand() < R)&&(collision == 0))||(collision == -1)
                            % reflect
                            if obj.debug == 1
                                fprintf('\treflected in z\n')
                            end
                            if current_layer == 0
                                obj.ph_top = obj.ph_top + 1;
                                return
                            end % lost out the top
                            s_polar = s_polar*Rs / (s_polar*Rs + (1-
s_polar)*Rp);
```

```
                            direc(3) = -1*direc(3);
                            obj.ph_pos = collision_point + 10^-
10*sign(direc(3));

                        else
                            % transmit
                            if obj.debug == 1
                                fprintf('\ttransmitted through z\n')
                                fprintf(['\tlayer ID =
',num2str(layer_id),'\n'])
                            end
                            s_polar = s_polar*(1-Rs) / (s_polar*(1-Rs) + (1-
s_polar)*(1-Rp));
                            r = n1/n2; c = abs(direc(3));
                            v_ref = r*direc + (r*c - sqrt(1-r^2*(1-c^2)))*[0 0
-sign(direc(3))];
                            direc = v_ref;
%                            if ~(abs(direc(3)) == 1)
%                                direc = direc/abs(direc).*[1 1 0]*sqrt((1-
(cos(th_t))^2)/((direc(1)/direc(2))^2+1)) + [0 0 cos(th_t)];
%                            end
                            obj.ph_pos = collision_point + 10^-10*direc;
                            if (layer_id == 0)
                                obj.ph_top = obj.ph_top + 1;
                                return
                            elseif (layer_id > numel(obj.layers))
                                obj.ph_bottom = obj.ph_bottom + 1;
                                return
                            end % lost defintion
                            reflecting = 0; % Photon is in new layer;
penetration obeys new rules
                        end % end if reflects
                    end % if nearest_wall == 3
                end % while reflecting
            end % while propogating
        end % function propogatePhoton
        function plot_handle = eff_plot(obj, N_photons)
            trunc_wall1 = num2str(round(obj.ph_wall(1)/N_photons*100,3));
            space1 = repmat(' ',1,5-length(trunc_wall1));
            trunc_wall2 = num2str(round(obj.ph_wall(2)/N_photons*100,3));
            space2 = repmat(' ',1,5-length(trunc_wall2));
            trunc_wall3 = num2str(round(obj.ph_wall(3)/N_photons*100,3));
            space3 = repmat(' ',1,5-length(trunc_wall3));
            trunc_wall4 = num2str(round(obj.ph_wall(4)/N_photons*100,3));
            space4 = repmat(' ',1,5-length(trunc_wall4));
            trunc_top = num2str(round(obj.ph_top/N_photons*100,3));
            space_top = repmat(' ',1,5-length(trunc_top));
            trunc_bottom = num2str(round(obj.ph_bottom/N_photons*100,3));
            space_bottom = repmat(' ',1,5-length(trunc_bottom));
            %plot_handle =
            fprintf(['      ',trunc_wall3,'\n      ______\n     |
',space_top,trunc_top,'|\n',space1,trunc_wall1,'|
',space_bottom,trunc_bottom,'|',trunc_wall2,'\n     |______|\n
',space4,trunc_wall4,'\n']);
        end % function eff_plot
    end % methods
```

```
end % concentrator classdef
```

Simulation

```
Transmittance_data = importdata('C:\Users\Odin Achorn\Dropbox (MIT)\LSC Monte
Carlo Simulation\CdSe_CdS_Transmittance.csv');
Transmittance = vertcat(horzcat((4000:-
1:1001)',100*ones(3000,1)),Transmittance_data.data);
PL_data = importdata('C:\Users\Odin Achorn\Dropbox (MIT)\LSC Monte Carlo
Simulation\CdSe_CdS_PL.xlsx');
PL = PL_data.data;
PMMA_Transmittance = Transmittance;
PMMA_Transmittance(:,2) = 100*ones(3801,1);
PMMA_PL = PL;

N_photons = 1000;
eff = 0;

conc = concentrator([300 23], 0, 405, [0 0 0 0 0]); % Dimensions (mm), 0
(polarization), Source spectrum or laser wavelength (nm)
%conc.full_collect = 1; % 0 if surrounded by air, 1 if collecter is index
matched
conc = conc.addLayer('QDs', 0.1, 0.95, 1.48, Transmittance, PL, 0); % name,
thickness (mm), QY, n(ref. ind.),Transmittance (%), PL (a.u.)
conc = conc.addLayer('waveguide', 6, 1, 1.49, PMMA_Transmittance, PMMA_PL, 0);

conc.debug = 0;
for photon_num = 1:N_photons
    if conc.debug == 1
        fprintf('new photon\n')
    end
    conc = conc.propogatePhoton([1],[loc,0],1.00029); % targets: 1,2,3,4 for
+x,-x,+y,-y; location of laser
                                                      % 1.00029, 3.85
end

eff = (conc.ph_collect)/N_photons
%conc.eff_plot(N_photons)
%toc
```

Runner

```
tic;
locations = 149:-1:-149;
loc_inds = 1:max(size(locations));
eff_mat = zeros(max(size(locations)),1);
distance = (1:1:299)';
for loc_ind = loc_inds
    loc = locations(loc_ind)
    run('simulation.m')
    eff_mat(loc_ind) = eff;
end
toc
```

References

(1) Debije, M. G.; Verbunt, P. P. C. Thirty Years of Luminescent Solar Concentrator Research: Solar Energy for the Built Environment. *Adv. Energy Mater.* **2012**, *2*, 12–35.

(2) Swartz, B. A.; Cole, T.; Zewail, A. H. Photon Trapping and Energy Transfer in Multiple-Dye Plastic Matrices: An Efficient Solar-Energy Concentrator. *Opt. Lett.* **1977**, *1*, 73.

(3) Bailey, S. T.; Lokey, G. E.; Hanes, M. S.; Shearer, J. D. M.; McLafferty, J. B.; Beaumont, G. T.; Baseler, T. T.; Layhue, J. M.; Broussard, D. R.; Zhang, Y.-Z.; Wittmershaus, B. P. Optimized Excitation Energy Transfer in a Three-Dye Luminescent Solar Concentrator. *Sol. Energy Mater. Sol. Cells* **2007**, *91*, 67–75.

(4) Altan Bozdemir, O.; Erbas-Cakmak, S.; Ekiz, O. O.; Dana, A.; Akkaya, E. U. Towards Unimolecular Luminescent Solar Concentrators: Bodipy-Based Dendritic Energy-Transfer Cascade with Panchromatic Absorption and Monochromatized Emission. *Angew. Chemie Int. Ed.* **2011**, *50*, 10907–10912.

(5) Schiphorst, J. ter; Kendhale, A. M.; Debije, M. G.; Menelaou, C.; Herz, L. M.; Schenning, A. P. H. J. Dichroic Perylene Bisimide Triad Displaying Energy Transfer in Switchable Luminescent Solar Concentrators. *Chem. Mater.* **2014**, *26*, 3876–3878.

(6) Tummeltshammer, C.; Taylor, A.; Kenyon, A. J.; Papakonstantinou, I. Homeotropic Alignment and Förster Resonance Energy Transfer: The Way to a Brighter Luminescent Solar Concentrator. *J. Appl. Phys.* **2014**, *116*, 173103.

(7) Currie, M. J.; Mapel, J. K.; Heidel, T. D.; Goffri, S.; Baldo, M. A. High-Efficiency Organic Solar Concentrators for Photovoltaics. *Science* **2008**, *321*, 226–228.

(8) Banal, J. L.; Ghiggino, K. P.; Wong, W. W. H. Efficient Light Harvesting of a Luminescent Solar Concentrator Using Excitation Energy Transfer from an Aggregation-Induced Emitter. *Phys. Chem. Chem. Phys.* **2014**, *16*, 25358–25363.

(9) Mulder, C. L.; Theogarajan, L.; Currie, M.; Mapel, J. K.; Baldo, M. A.; Vaughn, M.; Willard, P.; Bruce, B. D.; Moss, M. W.; McLain, C. E.; Morseman, J. P. Luminescent Solar Concentrators Employing Phycobilisomes. *Adv. Mater.* **2009**, *21*, 3181–3185.

(10) Gutierrez, G. D.; Coropceanu, I.; Bawendi, M. G.; Swager, T. M. A Low Reabsorbing Luminescent Solar Concentrator Employing π-Conjugated Polymers. *Adv. Mater.* **2016**, *28*, 497–501.

(11) Meinardi, F.; Colombo, A.; Velizhanin, K. A.; Simonutti, R.; Lorenzon, M.; Beverina, L.; Viswanatha, R.; Klimov, V. I.; Brovelli, S. Large-Area Luminescent Solar Concentrators Based on Stokes-Shift-Engineered Nanocrystals in a Mass-Polymerized PMMA Matrix. *Nat. Photonics* **2014**, *8*, 392–399.

(12) Coropceanu, I.; Bawendi, M. G. Core/Shell Quantum Dot Based Luminescent Solar Concentrators with Reduced Reabsorption and Enhanced Efficiency. *Nano Lett.* **2014**, *14*, 4097–4101.

(13) Meinardi, F.; McDaniel, H.; Carulli, F.; Colombo, A.; Velizhanin, K. A.; Makarov, N. S.; Simonutti, R.; Klimov, V. I.; Brovelli, S. Highly Efficient Large-Area Colourless Luminescent Solar Concentrators Using Heavy-Metal-Free Colloidal Quantum Dots. *Nat. Nanotechnol.* **2015**, *10*, 878–885.

(14) Li, C.; Chen, W.; Wu, D.; Quan, D.; Zhou, Z.; Hao, J.; Qin, J.; Li, Y.; He, Z.; Wang, K. Large Stokes Shift and High Efficiency Luminescent Solar Concentrator Incorporated with $CuInS_2$/ZnS Quantum Dots. *Sci. Rep.* **2015**, *5*, 17777.

(15) Li, H.; Wu, K.; Lim, J.; Song, H. J.; Klimov, V. I. Doctor-Blade Deposition of Quantum Dots onto Standard Window Glass for Low-Loss Large-Area Luminescent Solar Concentrators. *Nat. Energy* **2016**, *1*, 16157.
(16) Sumner, R.; Eiselt, S.; Kilburn, T. B.; Erickson, C.; Carlson, B.; Gamelin, D. R.; McDowall, S.; Patrick, D. L. Analysis of Optical Losses in High-Efficiency $CuInS_2$-Based Nanocrystal Luminescent Solar Concentrators: Balancing Absorption versus Scattering. *J. Phys. Chem. C* **2017**, *121*, 3252–3260.
(17) Meinardi, F.; Ehrenberg, S.; Dhamo, L.; Carulli, F.; Mauri, M.; Bruni, F.; Simonutti, R.; Kortshagen, U.; Brovelli, S. Highly Efficient Luminescent Solar Concentrators Based on Earth-Abundant Indirect-Bandgap Silicon Quantum Dots. *Nat. Photonics* **2017**, *11*, 177–185.
(18) Wu, K.; Li, H.; Klimov, V. I. Tandem Luminescent Solar Concentrators Based on Engineered Quantum Dots. *Nat. Photonics* **2018**, *12*, 105–110.
(19) Bergren, M. R.; Makarov, N. S.; Ramasamy, K.; Jackson, A.; Guglielmetti, R.; McDaniel, H. High-Performance $CuInS_2$ Quantum Dot Laminated Glass Luminescent Solar Concentrators for Windows. *ACS Energy Lett.* **2018**, *3*, 520–525.
(20) Efros, A. L.; Nesbitt, D. J. Origin and Control of Blinking in Quantum Dots. *Nat. Nanotechnol.* **2016**, *11*, 661–671.
(21) Houtepen, A. J.; Hens, Z.; Owen, J. S.; Infante, I. On the Origin of Surface Traps in Colloidal II-VI Semiconductor Nanocrystals. *Chem. Mater.* **2017**, *29*, 752–761.
(22) Reiss, P.; Protière, M.; Li, L. Core/Shell Semiconductor Nanocrystals. *Small* **2009**, *5*, 154–168.
(23) Hines, M. A.; Guyot-Sionnest, P. Synthesis and Characterization of Strongly Luminescing ZnS-Capped CdSe Nanocrystals. *J. Phys. Chem.* **1996**, *100*, 468–471.
(24) Peng, X.; Schlamp, M. C.; Kadavanich, A. V.; Alivisatos, A. P. Epitaxial Growth of Highly Luminescent CdSe/CdS Core/Shell Nanocrystals with Photostability and Electronic Accessibility. *J. Am. Chem. Soc.* **1997**, *119*, 7019–7029.
(25) Kim, S.; Fisher, B.; Eisler, H. J.; Bawendi, M. Type-II Quantum Dots: CdTe/CdSe(Core/Shell) and CdSe/ZnTe(Core/Shell) Heterostructures. *J. Am. Chem. Soc.* **2003**, *125*, 11466–11467.
(26) Sadeghi, S.; Bahmani Jalali, H.; Melikov, R.; Ganesh Kumar, B.; Mohammadi Aria, M.; Ow-Yang, C. W.; Nizamoglu, S. Stokes-Shift-Engineered Indium Phosphide Quantum Dots for Efficient Luminescent Solar Concentrators. *ACS Appl. Mater. Interfaces* **2018**, *10*, 12975–12982.
(27) Aharoni, A.; Mokari, T.; Popov, I.; Banin, U. Synthesis of InAs/CdSe/ZnSe Core/Shell1/Shell2 Structures with Bright and Stable near-Infrared Fluorescence. *J. Am. Chem. Soc.* **2006**, *128*, 257–264.
(28) Vela, J.; Htoon, H.; Chen, Y.; Park, Y.-S.; Ghosh, Y.; Goodwin, P. M.; Werner, J. H.; Wells, N. P.; Casson, J. L.; Hollingsworth, J. A. Effect of Shell Thickness and Composition on Blinking Suppression and the Blinking Mechanism in 'Giant' CdSe/CdS Nanocrystal Quantum Dots. *J. Biophotonics* **2010**, *3*, 706–717.
(29) Ghosh, Y.; Mangum, B. D.; Casson, J. L.; Williams, D. J.; Htoon, H.; Hollingsworth, J. A. New Insights into the Complexities of Shell Growth and the Strong Influence of Particle Volume in Nonblinking "Giant" Core/Shell Nanocrystal Quantum Dots. *J. Am. Chem. Soc.* **2012**, *134*, 9634–9643.
(30) Chen, O.; Zhao, J.; Chauhan, V. P.; Cui, J.; Wong, C.; Harris, D. K.; Wei, H.; Han, H. S.;

Fukumura, D.; Jain, R. K.; Bawendi, M. G. Compact High-Quality CdSe-CdS Core-Shell Nanocrystals with Narrow Emission Linewidths and Suppressed Blinking. *Nat. Mater.* **2013**, *12*, 445–451.
(31) Sahu, A.; Kang, M. S.; Kompch, A.; Notthoff, C.; Wills, A. W.; Deng, D.; Winterer, M.; Frisbie, C. D.; Norris, D. J. Electronic Impurity Doping in CdSe Nanocrystals. *Nano Lett.* **2012**, *12*, 2587–2594.
(32) Kompch, A.; Sahu, A.; Notthoff, C.; Ott, F.; Norris, D. J.; Winterer, M. Localization of Ag Dopant Atoms in CdSe Nanocrystals by Reverse Monte Carlo Analysis of EXAFS Spectra. *J. Phys. Chem. C* **2015**, *119*, 18762–18772.
(33) Li, L.; Pandey, A.; Werder, D. J.; Khanal, B. P.; Pietryga, J. M.; Klimov, V. I. Efficient Synthesis of Highly Luminescent Copper Indium Sulfide-Based Core/Shell Nanocrystals with Surprisingly Long-Lived Emission. *J. Am. Chem. Soc.* **2011**, *133*, 1176–1179.
(34) Norris, D. J.; Yao, N.; Charnock, F. T.; Kennedy, T. A. High-Quality Manganese-Doped ZnSe Nanocrystals. *Nano Lett.* **2001**, *1*, 3–7.
(35) Zu, L.; Norris, D. J.; Kennedy, T. A.; Erwin, S. C.; Efros, A. L. Impact of Ripening on Manganese-Doped ZnSe Nanocrystals. *Nano Lett.* **2006**, *6*, 334–340.
(36) Gan, C.; Xiao, M.; Battaglia, D.; Pradhan, N.; Peng, X. Size Dependence of Nonlinear Optical Absorption and Refraction of Mn-Doped ZnSe Nanocrystals. *Appl. Phys. Lett.* **2007**, *91*.
(37) Pradhan, N.; Peng, X. Efficient and Color-Tunable Mn-Doped ZnSe Nanocrystal Emitters: Control of Optical Performance via Greener Synthetic Chemistry. *J. Am. Chem. Soc.* **2007**, *129*, 3339–3347.
(38) Gan, C.; Zhang, Y.; Battaglia, D.; Peng, X.; Xiao, M. Fluorescence Lifetime of Mn-Doped ZnSe Quantum Dots with Size Dependence. *Appl. Phys. Lett.* **2008**, *92*.
(39) Zhang, Y.; Gan, C.; Muhammad, J.; Battaglia, D.; Peng, X.; Xiao, M. Enhanced Fluorescence Intermittency in Mn-Doped Single ZnSe Quantum Dots. *J. Phys. Chem. C* **2008**, *112*, 20200–20205.
(40) Zeng, R.; Rutherford, M.; Xie, R.; Zou, B.; Peng, X. Synthesis of Highly Emissive Mn-Doped ZnSe Nanocrystals without Pyrophoric Reagents. *Chem. Mater.* **2010**, *22*, 2107–2113.
(41) Zu, L.; Wills, A. W.; Kennedy, T. A.; Glaser, E. R.; Norris, D. J. Effect of Different Manganese Precursors on the Doping Efficiency in ZnSe Nanocrystals. *J. Phys. Chem. C* **2010**, *114*, 21969–21975.
(42) Erickson, C. S.; Bradshaw, L. R.; McDowall, S.; Gilbertson, J. D.; Gamelin, D. R.; Patrick, D. L. Zero-Reabsorption Doped-Nanocrystal Luminescent Solar Concentrators. *ACS Nano* **2014**, *8*, 3461–3467.
(43) Griffini, G.; Levi, M.; Turri, S. Thin-Film Luminescent Solar Concentrators: Optimization and Photo-Stability Study of a Model Device Based on a Perylene Fluorescent Dye. In *12th International Conference on Environment and Electrical Engineering, EEEIC 2013*; IEEE, 2013; pp 89–93.
(44) Griffini, G.; Levi, M.; Turri, S. Thin-Film Luminescent Solar Concentrators: A Device Study towards Rational Design. *Renew. Energy* **2015**, *78*, 288–294.
(45) Li, H.; Wu, K.; Lim, J.; Song, H.-J.; Klimov, V. I. Doctor-Blade Deposition of Quantum Dots onto Standard Window Glass for Low-Loss Large-Area Luminescent Solar Concentrators. *Nat. Energy* **2016**, *1*, 16157.
(46) Liu, C.; Li, Z.; Hajagos, T. J.; Kishpaugh, D.; Chen, D. Y.; Pei, Q. Transparent Ultra-High-

Loading Quantum Dot/Polymer Nanocomposite Monolith for Gamma Scintillation. *ACS Nano* **2017**, *11*, 6422–6430.
(47) Connell, R.; Keil, J.; Peterson, C.; Hillmyer, M. A.; Ferry, V. E. CdSe/CdS–Poly(Cyclohexylethylene) Thin Film Luminescent Solar Concentrators. *APL Mater.* **2019**, *7*, 101123.
(48) Chen, Y.; Cordero, J. M.; Wang, H.; Franke, D.; Achorn, O. B.; Freyria, F. S.; Coropceanu, I.; Wei, H.; Chen, O.; Mooney, D. J.; Bawendi, M. G. A Ligand System for the Flexible Functionalization of Quantum Dots via Click Chemistry. *Angew. Chemie - Int. Ed.* **2018**, *57*, 4652–4656.
(49) Cui, J.; Beyler, A. P.; Marshall, L. F.; Chen, O.; Harris, D. K.; Wanger, D. D.; Brokmann, X.; Bawendi, M. G. Direct Probe of Spectral Inhomogeneity Reveals Synthetic Tunability of Single-Nanocrystal Spectral Linewidths. *Nat. Chem.* **2013**, *5*, 602–606.
(50) Murray, C. B.; Norris, D. J.; Bawendi, M. G. Synthesis and Characterization of Nearly Monodisperse CdE (E = S, Se, Te) Semiconductor Nanocrystallites. *J. Am. Chem. Soc.* **1993**, *115*, 8706–8715.
(51) LaMer, V. K.; Dinegar, R. H. Theory, Production and Mechanism of Formation of Monodispersed Hydrosols. *J. Am. Chem. Soc.* **1950**, *72*, 4847–4854.
(52) de Mello Donegá, C.; Liljeroth, P.; Vanmaekelbergh, D. Physicochemical Evaluation of the Hot-Injection Method, a Synthesis Route for Monodisperse Nanocrystals. *Small* **2005**, *1*, 1152–1162.
(53) van Embden, J.; Chesman, A. S. R.; Jasieniak, J. J. The Heat-Up Synthesis of Colloidal Nanocrystals. *Chem. Mater.* **2015**, *27*, 2246–2285.
(54) Allen, P. M.; Walker, B. J.; Bawendi, M. G. Mechanistic Insights into the Formation of InP Quantum Dots. *Angew. Chemie - Int. Ed.* **2010**, *49*, 760–762.
(55) Sugimoto, T. Preparation of Monodispersed Colloidal Particles. *Adv. Colloid Interface Sci.* **1987**, *28*, 65–108.
(56) Harris, D. K.; Bawendi, M. G. Improved Precursor Chemistry for the Synthesis of III-V Quantum Dots. *J. Am. Chem. Soc.* **2012**, *134*, 20211–20213.
(57) Gary, D. C.; Glassy, B. A.; Cossairt, B. M. Investigation of Indium Phosphide Quantum Dot Nucleation and Growth Utilizing Triarylsilylphosphine Precursors. *Chem. Mater.* **2014**, *26*, 1734–1744.
(58) Franke, D.; Harris, D. K.; Xie, L.; Jensen, K. F.; Bawendi, M. G. The Unexpected Influence of Precursor Conversion Rate in the Synthesis of III-V Quantum Dots. *Angew. Chemie - Int. Ed.* **2015**, *54*, 14299–14303.
(59) Song, W. S.; Lee, H. S.; Lee, J. C.; Jang, D. S.; Choi, Y.; Choi, M.; Yang, H. Amine-Derived Synthetic Approach to Color-Tunable InP/ZnS Quantum Dots with High Fluorescent Qualities. *J. Nanoparticle Res.* **2013**, *15*, 1750.
(60) Tessier, M. D.; Dupont, D.; De Nolf, K.; De Roo, J.; Hens, Z. Economic and Size-Tunable Synthesis of InP/ZnE (E = S, Se) Colloidal Quantum Dots. *Chem. Mater.* **2015**, *27*, 4893–4898.
(61) Peng, X.; Wickham, J.; Alivisatos, A. P. Kinetics of II-VI and III-V Colloidal Semiconductor Nanocrystal Growth: "Focusing" of Size Distributions. *J. Am. Chem. Soc.* **1998**, *120*, 5343–5344.
(62) Franke, D.; Harris, D. K.; Chen, O.; Bruns, O. T.; Carr, J. A.; Wilson, M. W. B.; Bawendi, M. G. Continuous Injection Synthesis of Indium Arsenide Quantum Dots Emissive in the Short-Wavelength Infrared. *Nat. Commun.* **2016**, *7*, 12749.

(63) Ramasamy, P.; Kim, N.; Kang, Y. S.; Ramirez, O.; Lee, J. S. Tunable, Bright, and Narrow-Band Luminescence from Colloidal Indium Phosphide Quantum Dots. *Chem. Mater.* **2017**, *29*, 6893–6899.
(64) Ramasamy, P.; Ko, K. J.; Kang, J. W.; Lee, J. S. Two-Step "Seed-Mediated" Synthetic Approach to Colloidal Indium Phosphide Quantum Dots with High-Purity Photo- and Electroluminescence. *Chem. Mater.* **2018**, *30*, 3643–3647.
(65) Xu, Z.; Li, Y.; Li, J.; Pu, C.; Zhou, J.; Lv, L.; Peng, X. Formation of Size-Tunable and Nearly Monodisperse InP Nanocrystals: Chemical Reactions and Controlled Synthesis. *Chem. Mater.* **2019**, *31*, 5331–5341.
(66) Won, Y. H.; Cho, O.; Kim, T.; Chung, D. Y.; Kim, T.; Chung, H.; Jang, H.; Lee, J.; Kim, D.; Jang, E. Highly Efficient and Stable InP/ZnSe/ZnS Quantum Dot Light-Emitting Diodes. *Nature* **2019**, *575*, 634–638.
(67) Gary, D. C.; Terban, M. W.; Billinge, S. J. L.; Cossairt, B. M. Two-Step Nucleation and Growth of InP Quantum Dots via Magic-Sized Cluster Intermediates. *Chem. Mater.* **2015**, *27*, 1432–1441.
(68) Gary, D. C.; Flowers, S. E.; Kaminsky, W.; Petrone, A.; Li, X.; Cossairt, B. M. Single-Crystal and Electronic Structure of a 1.3 Nm Indium Phosphide Nanocluster. *J. Am. Chem. Soc.* **2016**, *138*, 1510–1513.
(69) Cossairt, B. M. Shining Light on Indium Phosphide Quantum Dots: Understanding the Interplay among Precursor Conversion, Nucleation, and Growth. *Chem. Mater.* **2016**, *28*, 7181–7189.
(70) Xie, L.; Shen, Y.; Franke, D.; Sebastián, V.; Bawendi, M. G.; Jensen, K. F. Characterization of Indium Phosphide Quantum Dot Growth Intermediates Using MALDI-TOF Mass Spectrometry. *J. Am. Chem. Soc.* **2016**, *138*, 13469–13472.
(71) Stein, J. L.; Mader, E. A.; Cossairt, B. M. Luminescent InP Quantum Dots with Tunable Emission by Post-Synthetic Modification with Lewis Acids. *J. Phys. Chem. Lett.* **2016**, *7*, 1315–1320.
(72) Koh, S.; Eom, T.; Kim, W. D.; Lee, K.; Lee, D.; Lee, Y. K.; Kim, H.; Bae, W. K.; Lee, D. C. Zinc–Phosphorus Complex Working as an Atomic Valve for Colloidal Growth of Monodisperse Indium Phosphide Quantum Dots. *Chem. Mater.* **2017**, *29*, 6346–6355.
(73) Virieux, H.; Le Troedec, M.; Cros-Gagneux, A.; Ojo, W. S.; Delpech, F.; Nayral, C.; Martinez, H.; Chaudret, B. InP/ZnS Nanocrystals: Coupling NMR and XPS for Fine Surface and Interface Description. *J. Am. Chem. Soc.* **2012**, *134*, 19701–19708.
(74) Xie, L.; Harris, D. K.; Bawendi, M. G.; Jensen, K. F. Effect of Trace Water on the Growth of Indium Phosphide Quantum Dots. *Chem. Mater.* **2015**, *27*, 5058–5063.
(75) Baquero, E. A.; Virieux, H.; Swain, R. A.; Gillet, A.; Cros-Gagneux, A.; Coppel, Y.; Chaudret, B.; Nayral, C.; Delpech, F. Synthesis of Oxide-Free InP Quantum Dots: Surface Control and H2-Assisted Growth. *Chem. Mater.* **2017**, *29*, 9623–9627.
(76) Zhao, Q.; Kulik, H. J. Electronic Structure Origins of Surface-Dependent Growth in III-V Quantum Dots. *Chem. Mater.* **2018**, *30*, 7154–7165.
(77) Talapin, D. V. Experimental and Theoretical Studies on the Formation of Highly Luminescent II-VI, III-V and Core-Shell Semiconductor Nanocrystals, University of Hamburg, 2002.
(78) *Group IV Elements, IV-IV and III-V Compounds. Part b - Electronic, Transport, Optical and Other Properties*; Madelung, O., Rössler, U., Schulz, M., Eds.; Landolt-Börnstein - Group III Condensed Matter; Springer-Verlag: Berlin/Heidelberg, 2002; Vol. b.

(79) Handwerk, D. R.; Shipman, P. D.; Whitehead, C. B.; Özkar, S.; Finke, R. G. Mechanism-Enabled Population Balance Modeling of Particle Formation En Route to Particle Average Size and Size Distribution Understanding and Control. *J. Am. Chem. Soc.* **2019**, *141*, 15827–15839.
(80) Buffard, A.; Dreyfuss, S.; Nadal, B.; Heuclin, H.; Xu, X.; Patriarche, G.; Mézailles, N.; Dubertret, B. Mechanistic Insight and Optimization of InP Nanocrystals Synthesized with Aminophosphines. *Chem. Mater.* **2016**, *28*, 5925–5934.
(81) McMurtry, B. M.; Qian, K.; Teglasi, J. K.; Swarnakar, A. K.; De Roo, J.; Owen, J. S. Continuous Nucleation and Size Dependent Growth Kinetics of Indium Phosphide Nanocrystals. *Chem. Mater.* **2020**, *32*, 4358–4368.
(82) Wegner, K. D.; Pouget, S.; Ling, W. L.; Carrière, M.; Reiss, P. Gallium - a Versatile Element for Tuning the Photoluminescence Properties of InP Quantum Dots. *Chem. Commun.* **2019**, *55*, 1663–1666.
(83) Pu, Y.; Cai, F.; Wang, D.; Wang, J. X.; Chen, J. F. Colloidal Synthesis of Semiconductor Quantum Dots toward Large-Scale Production: A Review. *Ind. Eng. Chem. Res.* **2018**, *57*, 1790–1802.
(84) File:CIExy1931 Rec 2020.svg – Wikimedia Commons https://commons.wikimedia.org/wiki/File:CIExy1931_Rec_2020.svg (accessed Apr 14, 2020).
(85) Xie, R.; Peng, X. Synthesis of Cu-Doped InP Nanocrystals (d-Dots) with ZnSe Diffusion Barrier as Efficient and Color-Tunable NIR Emitters. *J. Am. Chem. Soc.* **2009**, *131*, 10645–10651.
(86) Hassan, A.; Zhang, X.; Liu, C.; Snee, P. T. Electronic Structure and Dynamics of Copper-Doped Indium Phosphide Nanocrystals Studied with Time-Resolved X-Ray Absorption and Large-Scale DFT Calculations. *J. Phys. Chem. C* **2018**, *122*, 11145–11151.
(87) Mundy, M. E.; Eagle, F. W.; Hughes, K. E.; Gamelin, D. R.; Cossairt, B. M. Synthesis and Spectroscopy of Emissive, Surface-Modified, Copper-Doped Indium Phosphide Nanocrystals. *ACS Mater. Lett.* **2020**, *2*, 576–581.
(88) Hughes, K. E.; Hartstein, K. H.; Gamelin, D. R. Photodoping and Transient Spectroscopies of Copper-Doped CdSe/CdS Nanocrystals. *ACS Nano* **2018**, *12*, 718–728.
(89) Nelson, H. D.; Hinterding, S. O. M.; Fainblat, R.; Creutz, S. E.; Li, X.; Gamelin, D. R. Mid-Gap States and Normal vs Inverted Bonding in Luminescent Cu+- and Ag+-Doped CdSe Nanocrystals. *J. Am. Chem. Soc.* **2017**, *139*, 6411–6421.
(90) Yang, W.; He, G.; Mei, S.; Zhu, J.; Zhang, W.; Chen, Q.; Zhang, G.; Guo, R. Controllable Synthesis of Dual Emissive Ag:InP/ZnS Quantum Dots with High Fluorescence Quantum Yield. *Appl. Surf. Sci.* **2017**, *423*, 686–694.
(91) Vinokurov, A.; Chernysheva, G.; Mordvinova, N.; Dorofeev, S. Optical Properties and Structure of Ag-Doped InP Quantum Dots Prepared by a Phosphine Synthetic Route. *Dalt. Trans.* **2018**, *47*, 12414–12419.
(92) Wei, X.; Mei, S.; Yang, B.; Chen, Z.; Dai, H.; Hu, Z.; Zhang, G.; Xie, F.; Zhang, W.; Guo, R. Optical and Morphological Properties of Single-Phased and Dual-Emissive InP/ZnS Quantum Dots via Transition Metallic and Inorganic Ions. *Langmuir* **2020**, *36*, 10244–10250.
(93) Leatherdale, C. A.; Bawendi, M. G. Electron and Hole Relaxation Pathways in Semiconductor Quantum Dots. *Phys. Rev. B - Condens. Matter Mater. Phys.* **1999**, *60*, 13740–13749.

(94) Ellingson, R. J.; Blackburn, J. L.; Yu, P.; Rumbles, G.; Mićić, O. I.; Nozik, A. J. Excitation Energy Dependent Efficiency of Charge Carrier Relaxation and Photoluminescence in Colloidal InP Quantum Dots. *J. Phys. Chem. B* **2002**, *106*, 7758–7765.
(95) Thomas, A.; Sandeep, K.; Somasundaran, S. M.; Thomas, K. G. How Trap States Affect Charge Carrier Dynamics of CdSe and InP Quantum Dots: Visualization through Complexation with Viologen. *ACS Energy Lett.* **2018**, *3*, 2368–2375.
(96) Hughes, K. E.; Stein, J. L.; Friedfeld, M. R.; Cossairt, B. M.; Gamelin, D. R. Effects of Surface Chemistry on the Photophysics of Colloidal InP Nanocrystals. *ACS Nano* **2019**, *13*, 14198–14207.